Development of a c-Si/nc-Si:H/a-Si:H multi-junction device with a smooth c-Si surface texture

D.A. van Nijen

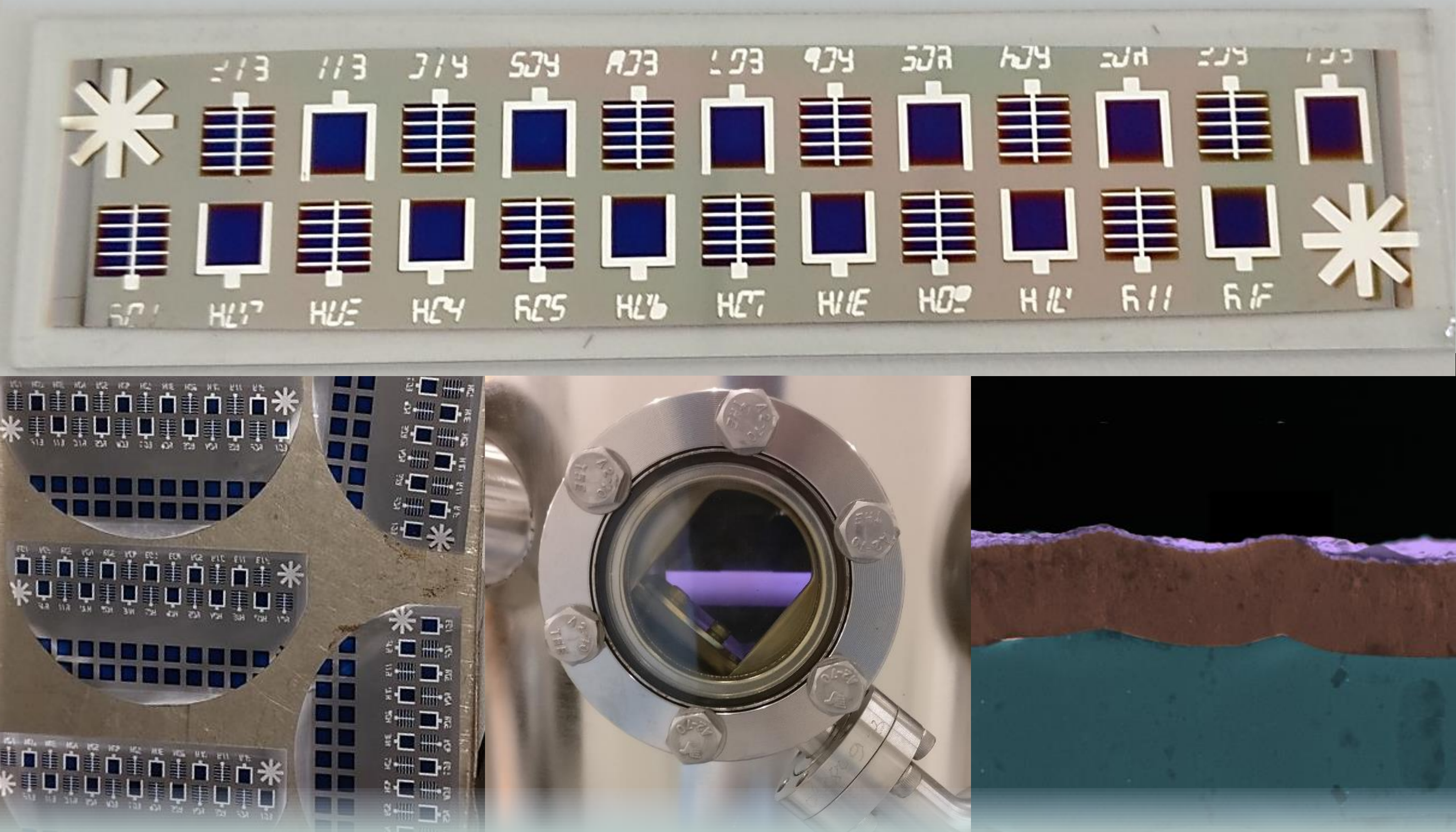

TU Delft Delft University of Technology

PVMD Delft University of Technology

Development of a c-Si/nc-Si:H/a-Si:H multi-junction device with a smooth c-Si surface texture

by

David van Nijen

to obtain the degree of Master of Science
at the Delft University of Technology,
to be defended publicly on Friday July 10, 2020 at 10:30 AM.

Student number:	4481933	
Project duration:	November 11, 2019 – July 10, 2020	
Thesis committee:	Prof. dr. ir. A. Smets,	TU Delft, Professor & Supervisor
	Prof. dr. A. Weeber,	TU Delft, Professor
	Dr. G.R. Chandra Mouli,	TU Delft, Assistant Professor
	Ir. T. de Vrijer,	TU Delft, PhD candidate & Daily supervisor

An electronic version of this thesis is available at `http://repository.tudelft.nl/`.

TU Delft Delft University of Technology

PVMD

Preface

This master thesis project marks the end of my time as a student in Delft. After having completed a bachelor programme in Applied Physics, I chose to continue my studies with the master programme Sustainable Energy Technology. During my master, I have learnt a lot about the energy system of the future. Since I believe that solar energy will play a major part in the energy transition, I chose to carry out my thesis project in this fascinating field.

The aim of my thesis project was to combine wafer-based crystalline silicon with thin film silicon technology to make a triple-junction cell. I am grateful for this versatile thesis topic, which has helped me to remain highly interested and keep on learning new things for the full eight months. By independently making solar cells myself, I have learnt more about photovoltaic technologies than I could ever have learnt from a textbook. For example, I will never complain again about doing dishes now that I have manually had to clean substrate holders that have been used to process nanocrystalline silicon.

In general, I would like to thank everyone from the PVMD group and the EKL staff for their help during my thesis project. Most of all, I would like to thank my daily supervisor Thierry de Vrijer, who is working on the DISCO project. He has given me guidance during the project and was always available on short notice when I had a question. My apologies to him and his wife for processing-related questions during weekends. Furthermore, I would like to thank Harsh Parasramka, who I have closely collaborated with. He has often helped me out when some holders needed to be placed in a machine and I could not do it myself. Together with Thierry and Harsh, I have worked hard over the last eight months while having a lot of fun as well.

Moreover, I would like to thank prof. Arno Smets for his enthusiasm, sharing his expertise during our meetings and for the fact that I could walk into his office with a question when needed. My gratitude also goes to Martijn Tijssen, who played an important part by keeping all the machines operational and always acted quickly when problems occured. Furthermore, I would like to thank the people participating in the DISCO project, as well as Gianluca Limodio and his team from the FlamingoPV project. In addition, I would like to thank Prof. Arthur Weeber and Dr. Chandra Mouli for being part of my graduation committee.

Finally, I would like to thank Yida, my family and my friends for their support and for always being there for me.

David van Nijen
Delft, July 2020

Abstract

For the continued growth of PV capacity, it will be necessary to store vast amounts of energy to overcome seasonal differences in energy generation. To this end, the conversion of electricity to liquid or gas fuels could play an important role in the future energy system. There are numerous ways to create fuels from solar energy, the possibilities range from completely monolithically integrated photoelectrochemical (PEC) devices to configurations where the PV is completely decoupled from the electrochemical reaction. This thesis is part of the DISCO project, where the aim is to create multi-junction PV cells that can generate a high voltage and integrate these into PEC devices. The aim of this thesis project is to optimize the photovoltaic performance of a triple-junction device based on crystalline silicon (c-Si), nanocrystalline silicon (nc-Si:H) and amorphous silicon (a-Si:H).

The bottom junction of this triple-junction device is a wafer-based silicon heterojunction (SHJ) cell. The used wafer should have a smooth surface texture, since previous research has shown that growing a nc-Si:H absorber layer on the regular random pyramid surface texture results in the formation of cracks. To this end, three different proposed smooth surface textures were compared amongst each other. These surface textures were a smooth pyramid surface texture, a hexagonal surface texture created with photolithography, and a texture of crater like surface features obtained by etching a sacrificial layer. It was found that from these three textures, the best performing SHJ cells could be made from wafers with a smooth pyramid surface texture. With respect to the other surface textures, the smooth pyramid surface texturing approach leads to the smallest fraction of exposed <100> crystal orientations, which are more challenging to passivate. The performance of the SHJ cell is extremely sensitive to the passivation quality of the intrinsic amorphous silicon layers on both side of the wafer. By optimizing this passivation layer and the doped layers, SHJ bottom cell efficiencies of over 18% were achieved.

The middle junction of this triple-junction device is based on a nc-Si:H absorber layer. By varying the crystallinity of this i-nc-Si:H absorber layer, it was found that optimal photovoltaic performance is achieved for a crystalline volume fraction between 50% and 65%. Furthermore, the thickness of this absorber layer can be varied to improve the current matching between the different subcells in the triple-junction device. To this end, the effect of a varying absorber layer thickness on the single-junction PV performance was investigated. It was found that the absorber layer thickness is a trade-off between on the one hand V_{oc} and FF, and on the other hand J_{sc}. For example, doubling the absorber layer thickness from 2.5 μm to 5.0 μm results in a J_{sc} increase from 18.2 mA/cm^2 to 20.8 mA/cm^2, whereas the V_{oc} and the FF respectively decrease from 506 mV and 0.65 to 481 mV and 0.59.

Once the bottom and middle junctions were optimized, different material combinations in the tunnel recombination junctions of the multi-junction device were investigated. It was found that p-nc-SiO_x and n-nc-SiO_x with appropriate doping levels and contact layers were the best performing materials in both tunnel recombination junctions. When the V_{oc} of the tandem cells was compared to the sum of the single-junction cells, the optimized tunnel recombination junctions resulted in a V_{oc} loss of 7 mV in the top tandem (nc-Si:H/a-Si:H), and 51 mV in the bottom tandem (SHJ/nc-Si:H).

By making use of all the performed optimizations described above, a triple-junction device based on c-Si/nc-Si:H/a-Si:H was processed. The final device had a PV efficiency of 13.63%, with a FF of 0.755, a V_{oc} of 1982 mV and a J_{sc} of 9.11 mA/cm^2. To the best of our knowledge, this is a world-record efficiency for this type of solar cell configuration. If it is managed in future research to match the current over the different subcells more evenly, this device has the potential to achieve a current density over 12 mA/cm^2.

Contents

List of Figures ix

List of Tables xiii

Nomenclature xvi

1 Introduction 1

1.1 Human influence on climate change . . . 1
1.2 Solar energy potential and current market share . . . 2
1.3 The need for long-term energy storage . . . 3
1.4 Photoelectrochemical Devices . . . 4
1.5 DISCO project. . . . 5
1.6 The triple-junction device . . . 6
1.7 Project description and outline . . . 7

2 Theoretical background 9

2.1 Photovoltaic fundamentals . . . 9
2.1.1 Solar radiation . . . 9
2.1.2 Semiconductors . . . 10
2.1.3 Solar cells . . . 11
2.2 Different types of solar cells . . . 12
2.2.1 Crystalline silicon . . . 12
2.2.2 Amorphous silicon . . . 12
2.2.3 Nanocrystalline silicon . . . 13
2.3 Loss mechanisms in solar cells . . . 13
2.3.1 Spectral mismatch . . . 13
2.3.2 Optical losses . . . 13
2.3.3 Electrical losses . . . 14
2.3.4 The Shockley-Queisser limit . . . 14
2.4 Solar cell parameters . . . 15
2.4.1 Short circuit current . . . 15
2.4.2 Open circuit voltage . . . 15
2.4.3 Fill factor . . . 15
2.4.4 Efficiency . . . 15
2.5 Light management . . . 16
2.6 Multi-junction PV cells . . . 17
2.6.1 The concept . . . 17
2.6.2 Tunnel recombination junctions . . . 18
2.6.3 Interface engineering . . . 18

3 PV cell production and characterization 19

3.1 Production tools . . . 19
3.1.1 Plasma-enhanced chemical vapour deposition . . . 19
3.1.2 Low pressure chemical vapour deposition . . . 20
3.1.3 Radio-frequency magnetron sputtering . . . 20
3.1.4 Metal evaporation . . . 20
3.1.5 Ion implantation . . . 21
3.2 Texturing methods of c-Si wafers . . . 21
3.2.1 Smooth pyramid texturing . . . 21
3.2.2 Photolithography texturing . . . 22
3.2.3 Sacrificial layer texturing . . . 23

3.3 Cell production method. 23
3.3.1 Silicon heterojunction single junction cell production 24
3.3.2 Nanocrystalline single junction cell production 25
3.3.3 Multi-junction cell production. 27
3.4 Characterization tools 27
3.4.1 Spectroscopic ellipsometry 27
3.4.2 Raman spectroscopy. 28
3.4.3 Photoconductance lifetime measurement 28
3.4.4 J-V measurement 28
3.4.5 External quantum efficiency 29
3.4.6 Transmittance and reflectance. 29
3.4.7 Scanning electron microscopy 30
3.4.8 Atomic force microscopy. 30

4 Optimizing the sacrificial layer texturing method 31
4.1 Grain growth mechanisms in the sacrificial layer 31
4.2 Sacrificial layer thickness 33
4.3 Annealing optimization. 33
4.4 Implantation dose 35
4.5 Different ions 35
4.6 Conclusions. 36

5 Optimizing the silicon heterojunction cell performance 37
5.1 Passivation of the smooth surface textures with different a-Si:H layers 37
5.2 Intrinsic a-Si:H passivation layer thickness 39
5.3 P-layer thickness 41
5.4 Conclusions. 42

6 Optimizing the nanocrystalline silicon cell performance 43
6.1 Optimizing the seed layer 43
6.2 Optimizing the intrinsic absorber layer 44
6.3 Optimizing the intrinsic absorber layer thickness 48
6.4 Conclusions. 49

7 Optimizing the tunnel recombination junctions 51
7.1 Optimizing the p-layer of the tunnel recombination junction. 51
7.1.1 The p-layer in the micromorph top tandem 51
7.1.2 The p-layer in the SHJ/nc-Si:H bottom tandem 52
7.1.3 Discussion of the p-layer performance. 53
7.2 Optimizing the n-layer of the tunnel recombination junction. 54
7.2.1 Top tandem 54
7.2.2 Discussion of the n-layer performance. 54
7.3 Conclusions. 55

8 The triple-junction device 57

9 Conclusions and recommendations 61
9.1 Conclusions. 61
9.2 Recommendations 63

Appendix 65
A: Etching time optimization of the sacrificial layer texturing method 65
B: Optimizing the n-layer thickness of the SHJ single-junction cell. 66
C: Optimizing the p-layer of the nc-Si:H single-junction cell 66
D: Calculation of the crystalline fraction 68
E: Nanocrystalline solar cell performance for varying absorber layer thickness 69
F: Deposition parameters of the doped layers in the tunnel recombination junctions 70
G: Extra data tunnel recombination junctions 71

Bibliography 73

List of Figures

1.1 Atmospheric CO_2 over the last 420,000 years [1]. The data in this graph is from the Antarctic Vostok [2], the Law Dome ice cores [3], and the Mauna Loa Observatory in Hawaii [4]. 1
1.2 The LCOE of different electricity generation technologies installed in Germany in 2018 [8]. . . . 2
1.3 Life-cycle land transformation for fuel cycles based on a 30-years timeframe (U.S. cases unless otherwise specified) [9]. 2
1.4 Electricity yield of a PV system installed in Delft every month in the year 2004 [11]. 3
1.5 Theoretical specific energies and energy densities comparison between different fuels and batteries [12]. 3
1.6 Scale of the different possible solar water splitting devices [15]. 4
1.7 Schematics of possible water splitting PV-EC device configurations. 5
1.8 Scanning electron microscope (SEM) top view and profile of a textured (A, C) and flat (B, D) solar cells [15]. 6
1.9 Raster electron microscope pictures of the wafer surface after the conventional anisotropic texture etch followed by the indicated duration of isotropic etching [20]. 6
1.10 SEM images of the different surface textures that have been developed in the DISCO project. . . 7

2.1 The different solar spectra [1]. 9
2.2 The Fermi energy for different types of doping [1]. 10
2.3 The formation of a space charge depletion region in a pn-junction [1]. 11
2.4 The splitting of the Fermi energy into two quasi-Fermi levels upon illumination [1]. 11
2.5 A simple and generic solar cell model [1]. 11
2.6 The pin-junction of an a-Si:H solar cell [1]. 12
2.7 The major loss mechanisms in the Shocley-Quisser limit [1]. 14
2.8 The effect of texturing [1]. 16
2.9 The spectral utilization of different solar cells [25]. 17
2.10 Theoretical efficiency of Si-based triple-junction cells as a function of middle and top cell band gaps [24]. 17
2.11 Band diagram with and without tunnel recombination junctions [1]. 18

3.1 Schematic representation of the plasma-enhanced chemical vapour deposition setup [26]. . . . 19
3.2 Schematic representation of a sputtering process [26]. 20
3.3 Schematic representation of two types of metal evaporation [27]. 21
3.4 Schematic representation of ion implantation [29]. 21
3.5 SEM images of the full pyramid surface texture (left) compared to the smooth pyramid surface texture (right). 22
3.6 The steps performed in the photolithography texturing method as well a tilted SEM image of the end result [22]. 23
3.7 The steps performed in the sacrificial layer texturing method as well a SEM image of the resulting texture [22]. 23
3.8 A schematic representation of the process of creating an SHJ cell. 24
3.9 Front side of a SHJ sample 25
3.10 A schematic representation of the process of creating a nc-Si:H cell. 25
3.11 Front side of a nc-Si:H sample 26
3.12 Schematic representation of a SE setup [31]. 27
3.13 Schematic representation of the lifetime tester used in this thesis project [31]. 28
3.14 Schematic representation of the J-V characteristic measurement setup [31]. 29
3.15 Schematic representation of the EQE measurement setup [40]. 29

4.1 Raman measurement of a 1500 nm thick sacrificial layer in as-deposited and implanted state. The implantation step was performed with argon ions at a dose of $1{\cdot}10^{16}$ ions/cm^2 and an energy of 250 keV. The measurements were performed at a laser excitation energy of 514 nm. The Raman spectra are normalized with respect to the total amount of counts. 32
4.2 Raman spectra of sacrificial layers with different Ar implantation doses. The layers had a thickness of 1500 nm and were annealed at 1050 °C for 1h. The measurements were performed at a laser excitation energy of 514 nm. The Raman spectra are presented on a semilog scale and normalized with respect to the highest count. 32
4.3 SEM images from the surface texture resulting from different sacrificial layer thicknesses. These sacrificial layers were all implanted with Ar at an implantation energy of 250 keV and a dose of $1 \cdot 10^{16}$ ions/cm^2. The wafers were annealed at 950 °C for 60 minutes. 33
4.4 SEM images from the resulting surface texture from different annealing times at temperatures of 950 °C and 1050 °C. These sacrificial layers all had a thickness of 1 μm and were implanted with Ar at an implantation energy of 250 keV and a dose of $1 \cdot 10^{16}$ ions/cm^2. 34
4.5 AFM analysis of the surface texture resulting from different annealing times and temperatures. . 34
4.6 SEM images from the resulting surface texture from different Ar implantation doses at an energy of 250 keV. The sacrificial layer thickness for this experiment was kept constant at 1500 nm and an annealing step of 60 minutes at 1050 °C was used. 35
4.7 SEM images from the resulting surface texture from implantation with BF_2 and As for sacrificial layer thicknesses of 250 nm and 500 nm. The implantation doses and energy were respectively $2{\cdot}10^{16}$ ions/cm^2 and 250 keV. The annealing step was performed for 60 minutes at 1050 °C. . . . 36

5.1 The <100> and the <111> surfaces of a silicon crystal [1]. 38
5.2 Charge carrier lifetime of the smooth pyramid and the photolithography textured wafers at a carrier density of 10^{15} cm^{-3} for different a-Si:H layer thicknesses. The p- and n-layer thicknesses were respectively 19 nm and 10 nm. 39
5.3 External solar cell parameters of SHJ cells with the smooth pyramid and photolithography texture for different a-Si:H passivation layer thicknesses. The p- and n-layer thicknesses were respectively 19 nm and 10 nm. 40
5.4 The external quantum efficiency of SHJ cells with the smooth pyramid texture for different a-Si:H passivation layer thicknesses. The p- and n-layer thicknesses were respectively 19 nm and 10 nm. 40
5.5 The external quantum efficiency of SHJ cells with the photolithography texture for different a-Si:H passivation layer thicknesses. The p- and n-layer thicknesses were respectively 19 nm and 10 nm. 40
5.6 External solar cell parameters of SHJ cells with the smooth pyramid texture for different p-layer thicknesses. The i-a-Si:H passivation layer had a thickness of 9 nm on both sides, while the n-layer thicknesses was 10 nm. 41
5.7 The external quantum efficiency of SHJ cells with the smooth pyramid texture for different p-layer thicknesses. The i-a-Si:H passivation layer had a thickness of 14 nm on both sides, while the n-layer thicknesses was 10 nm. 41

6.1 Raman spectra of nc-Si:H intrinsic layers for varying SiH_4 flow (2.9-3.7sccm) at a deposition power of 40 W. The measurements were performed at a laser excitation energy of 633 nm and the spectra are normalized with respect to the total amount of counts in the measurement. . . . 44
6.2 Raman spectra measured of nc-Si:H intrinsic layers for varying power (34 W to 46 W) at a SiH_4 flow of 3.5 sccm. The measurements were performed at a laser excitation energy of 633 nm and the spectra are normalized with respect to the total amount of counts in the measurement. . . . 45
6.3 The crystalline fraction of the different intrinsic absorber layers. The fits to calculate the crystalline fraction were performed for Raman measurements with an excitation energy of both 633nm and 514 nm. 45
6.4 External solar cell parameters of nc-Si:H cells for varying SiH_4 flow and power during the intrinsic layer deposition. 46
6.5 EQE for nc-Si:H cells with varying SiH_4 flow rate and power during the deposition of the intrinsic layer. 47

6.6 External parameters of nc-Si:H single-junction cells with different thicknesses of the intrinsic absorber layer. 48
6.7 The external quantum efficiency of nc-Si:H single-junction cells with different thicknesses of the intrinsic absorber layer. 48

7.1 A schematic representation of the different p-layers that were tried in the TRJ of the micromorph top tandem. A plus-sign is indicative of a higher doping level. The exact deposition parameters of the different layers are presented in Table 4 of Appendix F. For the layers other than the contact layers of P5 and P6 a deposition power of 12 W was used. 52
7.2 A schematic representation of the different p-layers that were tried in the TRJ of the SHJ/nc-Si bottom tandem. A plus-sign is indicative of a higher doping level. The exact deposition parameters of the different layers are presented in Table 4 of Appendix F. 52
7.3 A schematic representation of the different n-layers that were tried in the TRJ of the micromorph top tandem. For all tandems, P3 from Figure 7.1 was incoroporated. A plus-sign is indicative of a higher doping level. The exact deposition parameters of the different layers are presented in Table 5 of Appendix F. 54

8.1 A schematic of the device structure of the triple-junction cell. 57
8.2 The JV characteristic of the triple-junction cell. The current density was corrected foro the J_{sc} that resulted from the EQE measurement of the nc-Si:H middle cell. 58
8.3 The external quantum efficiency of the triple-junction cell. The used absorber layer thicknesses for the a-Si:H and the nc-Si:H cells were respectively 160 nm and 4.0 μm. 59

1 Cross-sectional SEM images of a 1500 nm sacrificial layer after after implantation with $1{\cdot}10^{16}$ ions/cm^2 Ar ions at 250 keV, after 1h annealing at 1050 °C, after 4.5 minutes of etching and after 8.5 minutes of etching. This figure suggests that the etchant has an etching rate around 160 nm/min. 65
2 SEM images of the sacrificial layer after implantation with $1{\cdot}10^{16}$ ions/cm^2 Ar ions at 250 keV, after 1h annealing at 1050 °C, after 4.5 minutes of etching and after 8.5 minutes of etching. . . . 65
3 Highly zoomed in SEM images for the samples that were presented in Figure 2 with etching times of 4.5 minutes and 8.5 minutes. If the sacrificial layer is fully etched away, the microcracks in the SEM images seem to disappear. 65
4 External solar cell parameters of SHJ cells with the smooth pyramid texture for different n-layer thicknesses. The i-a-Si:H passivation layer had a thickness of 14 nm on both sides, while the p-layer thicknesses was 19 nm. 66
5 A schematic figure of the different p-layers that were tried, all labeled from P1 to P4. 66
6 External solar cell paramaters for the different p-layers that are presented in Figure 5 67
7 EQE for the different p-layers that are presented in Figure 5 67
8 Transmittance and reflectance measurements of the nc-Si:H cells for the different thicknesses of the intrinsic layer. Note that the data of the transmittance figure is linearly interpolated in between 840 and 865 nm to prevent outliers due to detector switching of the LAMBDA machine. 69
9 The external quantum efficiency of micromorph cells with the different p-layers from Figure 7.1. 71
10 The external quantum efficiency of micromorph cells where P3 from Figure 7.1 was used and varied in thickness. 72
11 The external quantum efficiency of SHJ/nc-Si:H bottom tandem cells with the different p-layers from Figure 7.2. 72
12 The external quantum efficiency of micromorph cells with the different n-layers from Figure 7.3. 72

List of Tables

3.1 Layer-by-layer PECVD deposition parameters for the performed SHJ cell production. 25
3.2 Layer-by-layer PECVD deposition parameters for the performed nip-deposited nc-Si:H cell production. 26
3.3 Layer-by-layer PECVD deposition parameters for the performed nip-deposited a-Si:H top cell production. 27

4.1 AFM analysis of the surface texture resulting from different sacrificial layer thicknesses 33

5.1 A comparison between different a-Si passivation layer types for wafers with a smooth pyramid and sacrificial layer texture. 38

6.1 External solar cell parameters of nc-Si:H single-junction cells with a varying seed layer. Seed layer thicknesses of 25 nm, 50 nm and 100 nm were investigated at a deposition power of 40 W and 50 W. 44
6.2 Standard deposition parameters for the intrinsic layer of nc-Si:H cells. 44
6.3 The left two columns present the SiH_4 flow rate and the power during the intrinsic layer deposition. The right four columns present the external solar cell parameters of the resulting cells. . 47

7.1 External parameters of the different p-layers that were tried in micromorph cells. ΔV_{oc} indicates the loss in V_{oc} compared to the sum of the two single-junction cells. 52
7.2 External parameters of the SHJ/nc-Si tandem cells with different p-layers. ΔV_{oc} indicates the loss in V_{oc} compared to the sum of the two single-junction cells. 53
7.3 External parameters of the different n-layers that were tried in micromorph cells. ΔV_{oc} indicates the loss in V_{oc} compared to the sum of the two single-junction cells. 54

8.1 External parameters of the different solar cells used in the different experiments. The single-junction external solar cell parameters are for an nc-Si:H middle cell absorber layer thicknesses of 4 μm and an a-Si:H top cell absorber layer thickness of 160 nm. However, it has to be noted that the reported bottom tandem had an nc-Si:H absorber layer thickness of 2.7 μm, hereby increasing the V_{oc} and decreasing the J_{sc} of the nc-Si:H subcell. 58

1 Deposition parameters for the different p-layers that were tried. 66
2 External solar cell parameters of nc-Si:H single-junction cells with varying deposition parameters for the intrinsic absorber layer. 69
3 External solar cell parameters of nc-Si:H single-junction cells with different absorber layer thicknesses. 69
4 Deposition parameters of the different p-layers that were used in tunnel recombination junctions of the tandem cells. 70
5 Deposition parameters of the different n-layers that were used in tunnel recombination junctions of the tandem cells. 70
6 External parameters of micromorph cells with varying p-layer thickness. The p-layer materials of P3 from Figure 7.1 were used for these micromorph cell. For these micromorph cells, the nc-Si:H absorber layer of the bottom cell had a thickness of 4.0 μm. 71
7 Series and shunt resistances of the different micromorph top tandem p-layers from Figure 7.1. . 71
8 Series and shunt resistances of the different bottom tandem p-layers from Figure 7.2. 71
9 Series and shunt resistances of the different micromorph top tandem n-layers from Figure 7.3. . 71

Nomenclature

Abbreviations

:H	hydrogenated
a-Si	amorphous silicon
AFM	atomic force microscopy
c-Si	crystalline silicon
CVD	chemical vapour deposition
EKL	Else Kooi laboratory
EQE	external quantum efficiency
FF	fill factor
GHG	greenhouse gas
i-	intrinsic
IRL	intermediate reflective layer
ITO	indium tin oxide
LCOE	levelized costs of electricity
LPCVD	low pressure chemical vapour deposition
MPP	maximum power point
NAOC	nitric acid oxidation cycle
nc-Si	nanocrystalline silicon
PEC	photoelectrochemical
PECVD	plasma-enhanced chemical vapour deposition
PV	photovoltaic
PVD	physical vapour deposition
RF	radio-frequency
SE	spectroscopic ellipsometry
SEM	scanning electron microscopy
SHJ	silicon heterojunction
SRH	Shockley-Read-Hall
STH	solar to hydrogen
TCO	transparent conducting oxide
TRJ	tunnel recombination junction

VHF very high frequency

ZnO:Al aluminium doped zinc oxide

Physics Constants

c speed of light *in vacuo* (2.9979 $\cdot 10^{8}$ ms^{-1})

h Planck constant (6.6261 $\cdot 10^{-34}$ Js)

k_B Boltzmann constant (1.3806 $\cdot 10^{-23}$ $m^2 kg s^{-2} K^{-1}$)

q elementary charge (1.6022 $\cdot 10^{-19}$ C)

Symbols

α absorption coefficient (-)

η efficiency (%)

λ wavelength (nm)

τ_{eff} minority charge carrier lifetime (ms)

R reflectivity (-)

R_{sh} shunt resistance ($\Omega \cdot m^2$)

R_{s} series resistance ($\Omega \cdot m^2$)

I_{sc} short circuit current (A)

J_0 saturation current density (mA/cm^2)

J_{ph} photocurrent density (mA/cm^2)

J_{sc} short circuit current density (mA/cm^2)

T temperature (K)

V_{oc} open circuit voltage (V)

1
Introduction

This chapter is meant to provide some background on the relevance of this thesis, and subsequently describes the project in detail. This chapter unavoidably makes use of some terms generally used in photovoltaics, most of which are explained more in-depth in chapter 2 *theoretical background*.

1.1. Human influence on climate change

Life on earth is only possible because of the atmosphere around it. Greenhouse gases that are present in the atmosphere trap the heat from the Sun, which results in a temperature that allows life on Earth. The greenhouse gas concentration on Earth has been naturally fluctuating for the past hundred thousands of years, also contributing to fluctuations in the climate. However, since approximately 1750, the CO_2 concentration has been increasing at a historically unusual high pace, which can be seen in Figure 1.1.

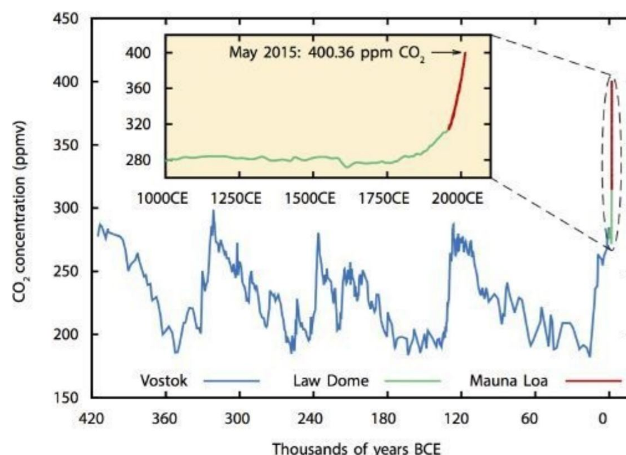

Figure 1.1: Atmospheric CO_2 over the last 420,000 years [1]. The data in this graph is from the Antarctic Vostok [2], the Law Dome ice cores [3], and the Mauna Loa Observatory in Hawaii [4].

When fossil fuels are burnt, they release CO_2 into the atmosphere. Mankind has been burning fossil fuels for energy generation since the industrial revolution started around 1750, which is one of the main reasons for the rising CO_2 concentration. The International Panel on Climate Change (IPCC) has identified that electricity and heat production contributed 25% to the total human-caused greenhouse gas emissions in 2010 [5]. However, this number will only rise if the way that electricity is produced stays the same, since more and more economic sectors are currently electrifying. The industry and the transport sector, which are respectively responsible for 21% and 14% of the worldwide greenhouse gas emissions, are examples of industries that are expected to electrify in the years to come. The IPCC has identified that the human-caused increase in greenhouse gases is a dominant force behind the observed global warming since the mid-20th century [5]. It is one of the main challenges of this era to reduce greenhouse gas emissions by humans and restore the CO_2 level in the atmosphere to the level of pre-industrial times.

1.2. Solar energy potential and current market share

Solar energy has proven to be a promising form of generating sustainable electricity on a large scale. Over the last 30 years, the costs of solar energy generation have been decreasing rapidly compared to other energy generation technologies [6]. The costs of solar PV electricity generation has already reached an all time low record price of 0.017 $/kWh in Dubai [7]. However, even in a less sunny country like Germany, the price of utility scale PV is among the cheapest forms of electricity generation, as can be seen in Figure 1.2. This Figure compares the different Levelized Costs of Electricity (LCOE) for different electricity generation technologies in Germany in 2018.

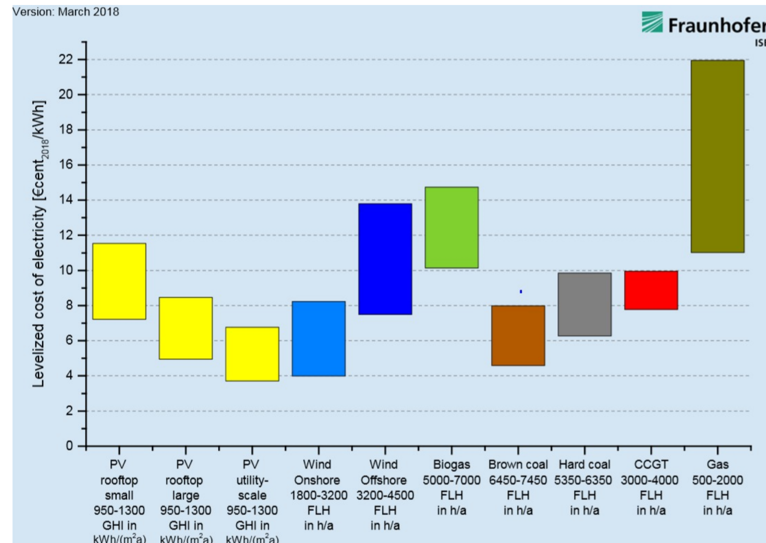

Figure 1.2: The LCOE of different electricity generation technologies installed in Germany in 2018 [8].

A challenge of renewable energy technologies in general is that they require a larger area than conventional fossil fuel power plants to generate the same amount of electricity. However, among the different renewable energy technologies that are available, solar PV is the technology that needs the least area per unit of energy generation. This is illustrated in Figure 1.3, where the land use for several renewable energy technologies are compared to fossil fuel plants. Note that these estimates are based on PV modules with 13% efficiency, while it is not uncommon for modern PV modules to approach an efficiency of 20%.

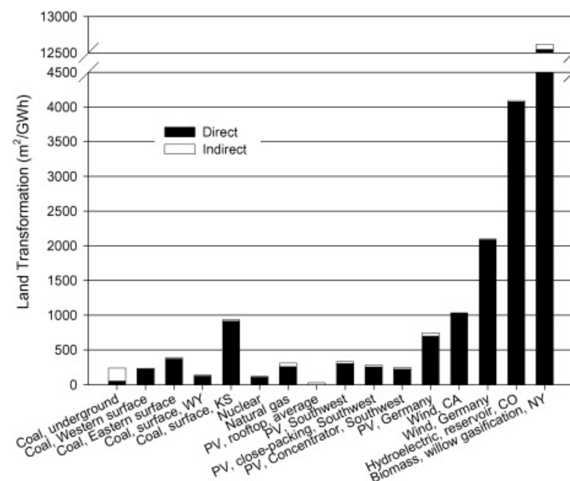

Figure 1.3: Life-cycle land transformation for fuel cycles based on a 30-years timeframe (U.S. cases unless otherwise specified) [9].

In 2017, solar PV and solar thermal respectively generated 398 and 397 TWh of energy worldwide [10]. However, the total final worldwide energy consumption in this same year was 113 PWh. A quick calculation shows that solar energy thus only generated a mere 0.7% of the total energy consumed in 2017.

1.3. The need for long-term energy storage

One of the main challenges of implementing solar energy on a large scale is that this technology does not generate a constant amount of energy throughout the day. Weather conditions can cause serious fluctuations in PV yield and the technology does not generate any electricity in the night. In off-grid PV applications these problems are typically solved by adding a battery to the PV system design, although this often heavily increases the total system costs. If the PV system is grid connected, the fluctuations in the energy yield are typically compensated for by the inertia in the power system. Another challenge is that the further away a PV system is installed from the equator, the more seasonal differences start to play a role. To illustrate this, the electricity yield of a PV system installed in Delft is presented for every month in the year 2004 in Figure 1.4.

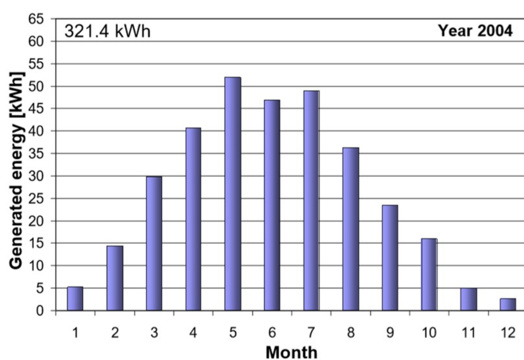

Figure 1.4: Electricity yield of a PV system installed in Delft every month in the year 2004 [11].

Figure 1.4 shows that the electricity yield was about 10 times higher in the summer than in the winter in the year 2004. Since energy consumption is relatively stable throughout the year, it will be necessary to store large amounts of energy to overcome seasonal differences if solar energy is implemented on a large scale. To store such large quantities of energy, liquid or gas fuels are a more feasible option than battery storage. Battery storage is not a suitable option for long-term energy storage because of its high self-discharge rates and the costs associated with such large storage capacities. Another advantage of fuels is that they have a higher energy density and specific energy for storage on a large scale than batteries, as can be seen in Figure 1.5.

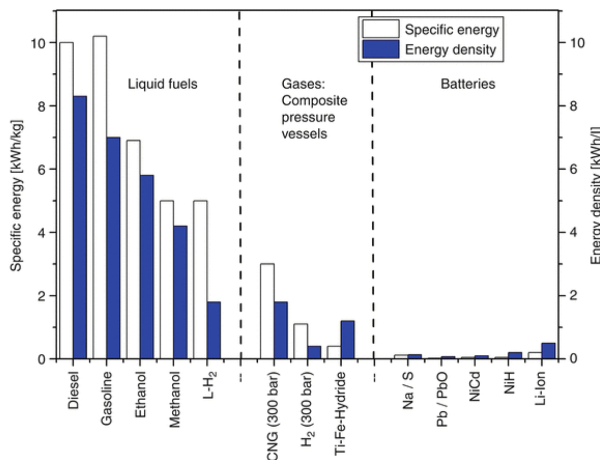

Figure 1.5: Theoretical specific energies and energy densities comparison between different fuels and batteries [12].

An advantage of storing electricity in the form of fuels is that these fuels do not necessarily have to be converted back to electricity for consumption. For example, fuels can serve as feedstock for different chemical processes in industry, can be used in fuel cells, or can be used in combustion engines in the transport sector. However, the conversion of electricity into fuels is an expensive process and the electricity-to-fuel efficiencies are typically low. For example, typical Alkaline and Polymer Electrolyte Membrane (PEM) electrolysis efficiencies lie in between 60% and 70% [13].

1.4. Photoelectrochemical Devices

Hydrogen is a promising fuel for energy storage, since it is highly abundant, lightweight, and if it is used in a fuel cell for energy generation the only product is water (H_2O). However, most of the hydrogen that is nowadays being used has been made from fossil fuels, emitting CO_2 in the process. Nevertheless, it is possible to make clean hydrogen by powering an electrolysis reaction with renewable energy. Optimizing this process is an important research topic nowadays, because many experts think that the physical and chemical advantages of hydrogen will make it an important synthetic fuel in the future [14]. In order to understand what is happening during an electrolysis reaction, it is useful to take a look at the half-reactions taking place during the process:

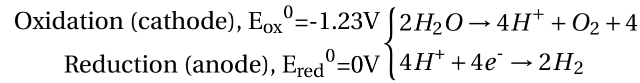

$$\text{Oxidation (cathode), } E_{ox}^{0}=-1.23\text{V} \begin{cases} 2H_2O \rightarrow 4H^{+} + O_2 + 4 \\ 4H^{+} + 4e^{-} \rightarrow 2H_2 \end{cases} \text{Reduction (anode), } E_{red}^{0}=0\text{V}$$

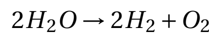

$$2H_2O \rightarrow 2H_2 + O_2$$

The overall redox reaction requires a theoretical voltage of 1.23 V. However, in practice a higher voltage in between 1.6 and 2.0 V is needed for electrolysis due to several loss mechanisms involved. Some of these losses are related to the electrolyte and contact resistance (depends on distance between the electrodes and the resistivity of the electrolyte), the resistance for charge carrier injection at the semiconductor/electrolyte interface, or the catalytic energy losses. Typically, the required overpotential increases for higher current densities [13].

There are several ways to reach the required voltage by using solar energy, of which the most important ones are presented in Figure 1.6. The possibilities range from completely monolithically integrated PEC devices to a device where the PV is completely decoupled from the electrolysis. In order to define the performance of a photoelectrochemical (PEC) devices, usually the solar to hydrogen (STH) efficiency is used, which is given by:

$$\eta_{STH} = \frac{J_{ph} 1.23V}{P_{in}} \tag{1.1}$$

in which η_{STH} is the STH efficiency, J_{ph} the photocurrent, and P_{in} is the incoming irradiance.

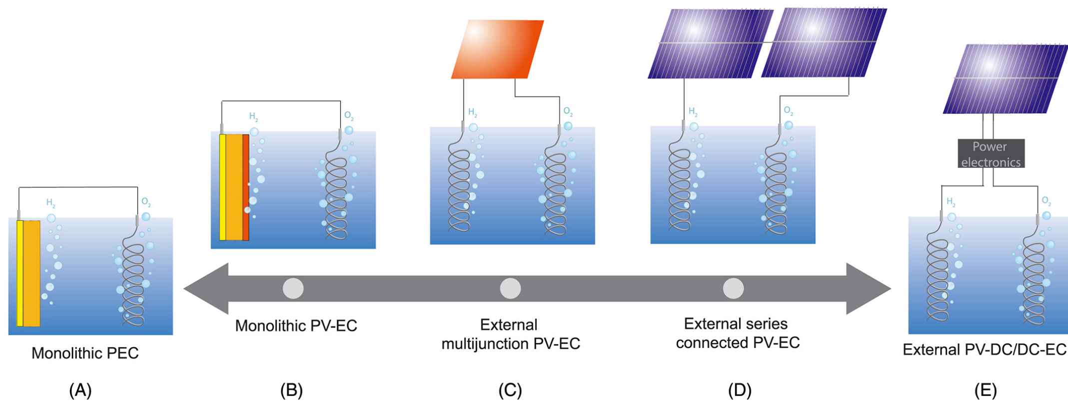

Figure 1.6: Scale of the different possible solar water splitting devices [15].

Below, the different designs for the PEC devices presented in Figure 1.6 are described:

- Monolithic PEC (A) devices only make use of one semiconductor absorber material. For these technologies it is typically challenging to find an absorber material with a bandgap that is high enough to reach the required voltage while still absorbing a significant part of the solar spectrum.

- PV-EC (B) or external multijunction PV-EC (C) devices make use of multijunction solar cells, of which the voltage can become high enough to drive electrolysis. Some of the highest STH efficiencies have been reached with III-V based multijunction solar cells, achieving 19.3% [16]. However, the III-V based

solar cells do contain relatively scarce materials unsuitable for cost-effective production on a large scale. If it would be possible to make a multijunction PV-EC device that is based on non-scarce materials, this could potentially result in easily producible compact PEC devices suitable for large scale production. However, it would remain challenging to come up with a large-scale design in which the hydrogen is collected.

- In external series connected PV-EC (D), several crystalline silicon based cells are connected in series to an electrolyzer, since one individual cell does not produce a high enough voltage. Advantages of this approach are that it only makes use of mature technologies and that the separate cells are highly current matched. However, a disadvantage is that the approach requires additional cabling compared to the multijunction approach. The PV-EC approach has been shown to reach an STH efficiency of 14.2% by connecting three heterojunction cells in series [17].

- In the external PV-DC/DC-EC (E) approach the PV device and the electrolyzer are decoupled and power electronics are located in between them. This approach is the most likely candidate to be used in industry, since it depends on the most mature technologies. Typical STH efficiencies of this approach would lie around 13%, based on c-Si modules and an electrolyzer with efficiencies of respectively 19% and 70% [13]. However, using III-V based solar technology it has been shown that this approach can even reach a 20.6% STH efficiency [18].

1.5. DISCO project

This section aims to give some background into the DISCO (DIrect Solar to CO conversion) project, of which this thesis is a part. The DISCO project focuses on making multi-junction PV-EC devices based on non-toxic and earth abundant materials. This is done by developing hybrid multi-junction solar cells in which c-Si wafer technology is combined with thin film silicon technology. By combining these two technologies, high voltages can be generated while achieving high current densities as well. Silicon based PV cells have the lowest costs per Wp due to their high market penetration. Unlike many PV semiconductor materials, the used materials based on silicon are resistant against water. Hence, a stable PEC device can be made by etching micropores into the multi-junction device and submerging the solution into an electrolyte, schematically presented in Figure 1.7a. However, another possibility is to connect the cell to the electrolyte with wires, presented in Figure 1.7b. Both of these two device configurations are investigated in the DISCO project.

Depending on the electrochemical reaction taking place in a PV-EC device, a specific voltage is required. For high solar to fuel efficiencies, the V_{mpp} of the solar cells should match the voltage at optimum operation conditions of the electrochemical component. The aim of the DISCO project is to deliver a package of PV device configurations with different voltages, so that there are different cells available for different electrochemical reactions.

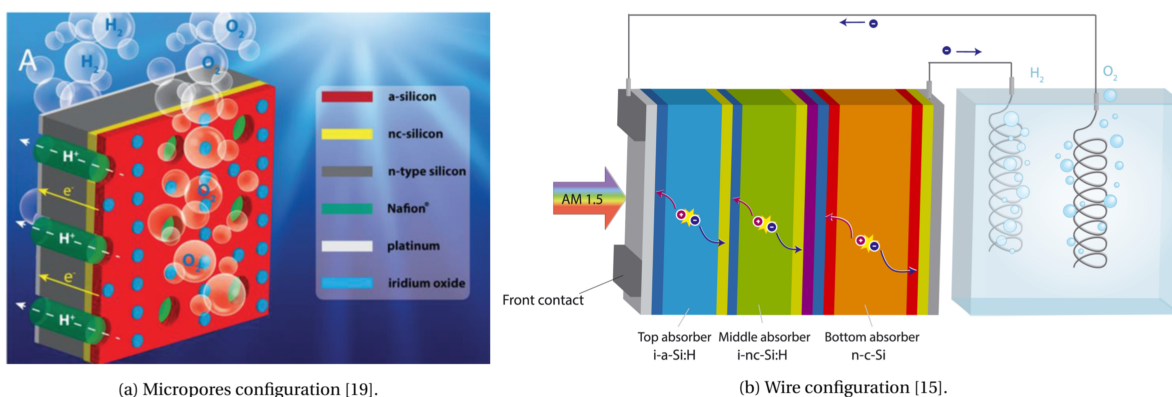

(a) Micropores configuration [19].

(b) Wire configuration [15].

Figure 1.7: Schematics of possible water splitting PV-EC device configurations.

The two multi-junction configurations that are currently being investigated in the DISCO project are a triple junction a-Si:H/nc-Si:H/c-Si and a quadruple junction a-Si:H/a-SiGe:H/nc-Si:H/c-Si device. Parallel to these devices, a low-bandgap solar cell based on a-GeSn:H is being developed. This cell can absorb photons below the c-Si bandgap (1.12 eV), which makes it a suitable material to be used as the bottom cell in a multi-

junction. Since a sufficient number of photons are present in the infrared spectrum, this bottom cell could add 0.2-0.4V to the V_{oc} of the device without being current limiting.

1.6. The triple-junction device

The goal of this thesis project is to develop a c-Si/nc-Si:H/a-Si:H triple-junction device. This device has already been developed experimentally before:

- Perez-Rodriguez et al. have developed a multijunction cell with a PV efficiency of 10.57%, a fill factor of 0.60, an open circuit voltage of 2.03V and a short-circuit current density of 8.65 mA/cm^2 at Delft University of Technology [15]. These cells were deposited on flat c-Si surfaces, because using a c-Si surface texture caused cracks in the nc-Si:H layer, as shown in Figure 1.8. These cracks were shown to have a detrimental impact on the FF and the V_{oc} of the device.

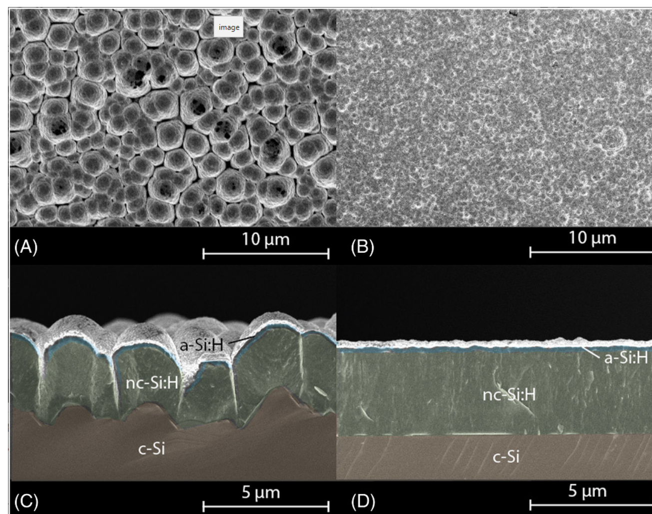

Figure 1.8: Scanning electron microscope (SEM) top view and profile of a textured (A, C) and flat (B, D) solar cells [15].

- Kirner et al. have developed a multijunction cell with a PV efficiency of 12.7%, a fill factor of 0.65, an open circuit voltage of 1.73V and a short-circuit current density of 11.3 mA/cm^2 at the Helmholtz-Zentrum Berlin [20]. In their research, the c-Si substrate consisted of a smooth surface texture, as presented in Figure 1.9. They made this texture by following the conventional anisotropic etch with an isotropic etch, which decreases the maximum difference between the tips and the valleys of the surface.

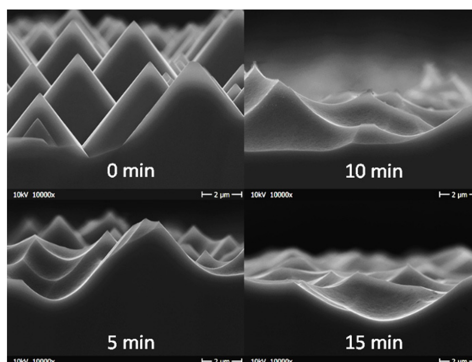

Figure 1.9: Raster electron microscope pictures of the wafer surface after the conventional anisotropic texture etch followed by the indicated duration of isotropic etching [20].

Even though it has proven to be challenging to find a c-Si surface texture that does not cause cracks in the nc-Si:H layer, the research of Kirner et al. has shown that a smooth surface texture is beneficial to the per-

formance of the triple-junction device. Firstly, the adhesion of the thin film cells onto the c-Si surface is improved if the substrate is textured, since this reduces the internal stresses in the nc-Si:H layer [15]. Secondly, higher current densities can be achieved with textured wafers, because the reflectance at the front surface is lower than for flat wafers. Hence, the aim in this thesis project is to integrate a c-Si bottom cell with a smooth surface texture into the triple-junction cell. Before the start of this project, three different surface textures have been developed in the DISCO project, all presented in Figure 1.10. Firstly, the smooth pyramid surface texture is created by isotropically etching a wafer with a random pyramid texture [21]. Secondly, the hexagonal photolithography surface texture is created by isotropic etching after an SiO_2 etching mask has been created with photolithography [22]. Thirdly, the sacrificial layer texture is created by etching a poly-Si sacrificial layer, where the grains in the sacrificial layer cause anisotropic etching behaviour [22]. More information about these surface texture, as well as a step-by-step description of the fabrication process is presented in section 3.2.

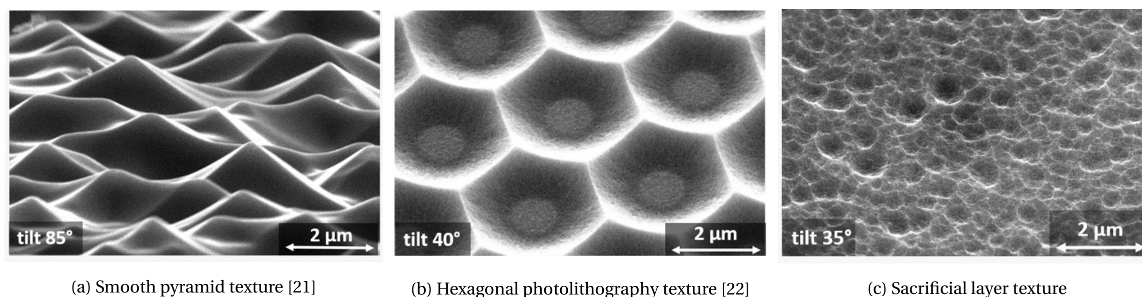

(a) Smooth pyramid texture [21] (b) Hexagonal photolithography texture [22] (c) Sacrificial layer texture

Figure 1.10: SEM images of the different surface textures that have been developed in the DISCO project.

1.7. Project description and outline

The focus of this thesis project is to optimize the performance of a triple junction hybrid c-Si/nc-Si:H/a-Si:H device. The project consists of four main research objectives:

1. Further optimize the sacrificial layer texturing method for c-Si wafers.
2. Optimize the performance of single junction silicon heterojunction (SHJ) solar cells with a smooth surface texture. This cell will be integrated into the triple-junction device as the bottom cell. This objective includes a comparison between the performance of SHJ cells with three different surface textures; the smooth pyramid texture (1), the hexagonal photolithography texture (2) and the sacrificial layer texure (3).
3. Optimize the absorber layer of nip substrate nc-Si:H single junction solar cells. This cell will be integrated into the triple-junction device as the middle cell.
4. Optimize the two tunnel recombination junctions (TRJs) in the triple-junction device, which is of utmost importance to achieve a high V_{oc}-Fill factor product.

Now that the reader has been introduced to the scope and background of the research topic, chapter two provides a more thorough theoretical background. Chapter three treats the manufacturing and characerization methods that were used. The optimization of the sacrificial layer method is described in chapter four, followed by the work that was done on the development of silicon heterojunction solar cells with a smooth surface texture in chapter five. Chapter six treats the optimization of nc-Si:H single-junction cells, followed by the optimization of the tunnel recombination junctions in chapter 7. After the performance of the final triple-junction device is discussed in chapter 8, the conclusions of this thesis work are presented in chapter 9.

2

Theoretical background

This chapter treats some theoretical background of photovoltaic solar technology that is relevant for this thesis project. Although it is not cited everywhere for practical reasons, most of the information in this chapter was taken from the book *Solar Energy* written by Smets et al. [1].

2.1. Photovoltaic fundamentals

In this section, some fundamental theory related to photovoltaic solar technology is described.

2.1.1. Solar radiation

In the centre of the Sun, the conditions are such that nuclear fusion can take place. The surface of the Sun has a temperature of about 6000K that behaves closely to a blackbody. The total power produced by the sun is 3.8 $\cdot 10^{26}$ W, of which $1.7 \cdot 10^{18}$ W reaches the Earth. The power produced by the Sun travels through space in the form of electromagnetic radiation. This radiation comes in quanta of energy called *photons*. The energy of a photon is determined by its wavelength λ:

$$E_{ph} = \frac{hc}{\lambda} \tag{2.1}$$

Just outside the Earth's atmosphere, the irradiance is about 1361 W/m^2, which is called the AM0 spectrum. However, the AM0 spectrum is attenuated as it travels through the atmosphere; light of specific wavelength is scattered or absorbed by air molecules. The spectrum that is perceived on the surface on the earth is thus dependent on the distance that light has travelled through the atmosphere, but also on the weather conditions. In order to be able to compare different solar cells, the AM1.5 spectrum is a common international standard for which solar cells are measured. This is the spectrum that is received in a Sun-facing plane surface tilted at 37 °to the horizontal. The AM1.5 spectrum corresponds to an irradiance of 1000 W/m^2. The spectral irradiance of the AM1.5, the AM0, and the 6000K blackbody radiation are all presented in Figure 2.1.

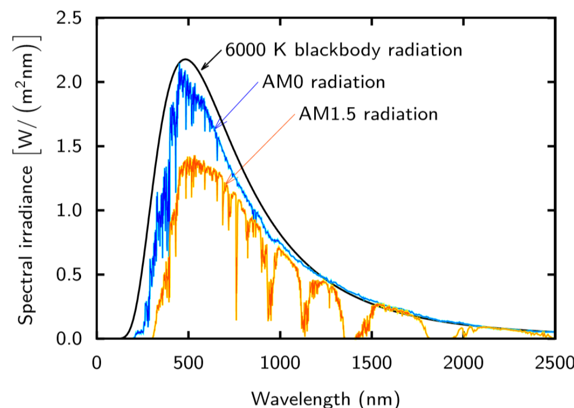

Figure 2.1: The different solar spectra [1].

2.1.2. Semiconductors

Semiconductors are characterized by their conductive behaviour, that is located in between a conductor and an insulator. The conductivity of a semiconductor scales with the amount of free charge carriers that are present in the material. Free charge carriers are created when an electron breaks free from a covalent bond, which means it is excited from the valence band to the conduction band. The energy needed for this excitation is equal to the band gap energy of the semiconductor and can be taken from thermal energy at room temperature or from photons. When an electron is excited, this creates a free electron in the conduction band as well as a free hole in the valence band. After excitation to the conduction band, a charge carrier is called a *free charge carrier*. In semiconductor material, free electrons and holes recombine some time after they have been excited. The exact time is random, but on average they recombine once the *free charge carrier lifetime* has passed by. The holes and electrons have then on average travelled a distance called the diffusion length.

In an intrinsic semiconductor at room temperature, the amount of free electrons in the conduction band is equal to the amount of holes in the valence band. This situation is described by a Fermi energy that lies exactly in between these two bands, as can be seen in Figure 2.2a.

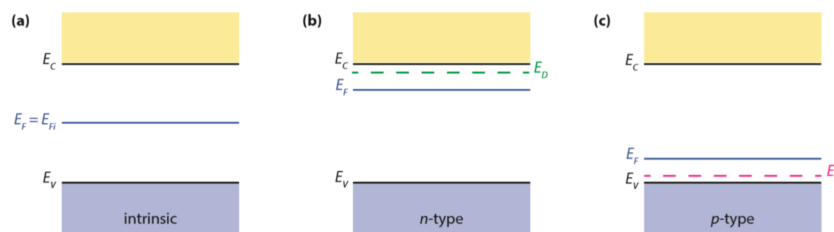

Figure 2.2: The Fermi energy for different types of doping [1].

However, in solar cells the semiconductor materials are often doped, which makes charge carrier separation possible. There are two types of doping:

- n-type doping: donor atoms are incorporated into a lattice (for Si lattices this is usually phosphorus). The donor atoms usually have one extra valence electron that cannot take part in a covalent bond with the other atoms in the lattice. The energy E_D of the weakly bound valence electron lies close to the conduction band, which means that they can easily be excited into the conduction band by absorbing thermal energy at room temperature. The increased amount of free electrons is represented by an increased Fermi-level in n-type material, which can be seen in Figure 2.2b.
- p-type doping: acceptor atoms are incorporated into a lattice (for Si lattices this is usually boron). The acceptor atoms have one valence electron too little to form covalent bonds with all four neighbouring Si atoms. However, this 'hole' in the lattice can accept electrons from other nearby covalent bonds. As a result, the 'hole' can travel through the lattice. Actually, the hole can be described just like a free electron, except for the fact that it is considered to be positively charged instead of negatively. The energy E_A of the hole lies close to the valence band, since a nearby valence electron can easily be excited into this new covalent bond at room temperature. The increased amount of free holes is represented by a decreased Fermi-level in p-type material, which can be seen in Figure 2.2c.

Increasing the doping level in a semiconductor can decrease the activation energy, which is defined as the energy difference between the Fermi level and the energy state where the charge carriers can conduct (conduction band for electrons, valence band for holes). A low E_{act} leads to a high conductivity, since a larger amount of electrons is in a state where they conduct. Furthermore, a common application of p- and n-doped materials is a *pn-junction*, in which these two material types are located directly next to each other. At the interface between these two material types, free electrons of n-type material recombine with free holes in the p-type material. The recombination of these free charge carriers leads to positively charged donor atoms and negatively charged acceptor atoms at the interface. The region where these charged donor and acceptor atoms exist is called the space charge region, and is presented schematically in Figure 2.3. The region is also often called the charge depletion region because of the absence of free charge carriers. In the space charge region there exists an electric field due to the differently charged donor atoms on both sides. The result of this electric field is that free charge carriers can only pass through a pn-junction if they move in the direction in which they are not opposed by the electric field. Hence, a pn-junction is a common way to separate electrons and holes from each other in a solar cell.

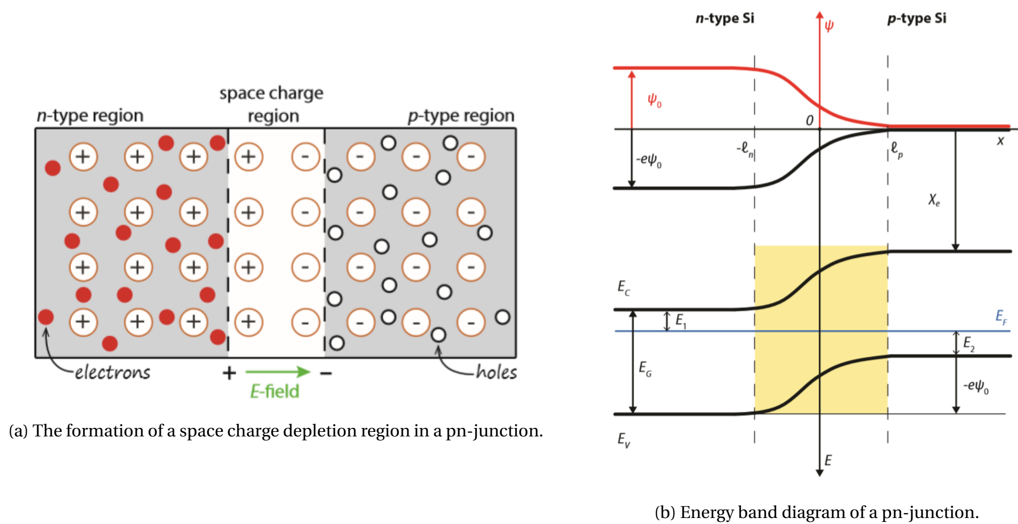

(a) The formation of a space charge depletion region in a pn-junction.

(b) Energy band diagram of a pn-junction.

Figure 2.3: The formation of a space charge depletion region in a pn-junction [1].

2.1.3. Solar cells

If a semiconductor is illuminated, the photons excite charge carriers from the valence band to the conduction band. Since in this process a significant amount of both free electrons and holes are created, the electron and hole concentrations change compared to the non-illuminated situation. If a semiconductor is illuminated, the situation is no longer described by one Fermi energy level. Now there exist two *quasi-Fermi energy* levels. The band diagram representation of this situation is presented in Figure 2.4.

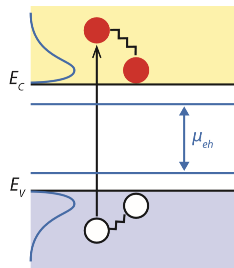

Figure 2.4: The splitting of the Fermi energy into two quasi-Fermi levels upon illumination [1].

Photovoltaic solar cells are based upon separating the electron-hole pair before they are able to recombine. This separation can be done in several different ways. One example is the earlier explained pn-junction, but in the next section also a different method called a *pin-junction* will be explained. The generation of electricity is achieved by making these charge carriers recombine through an external circuit, which makes electrons (and thus current) flow between the two electrodes of a solar cell. The whole process is sketched in Figure 2.5.

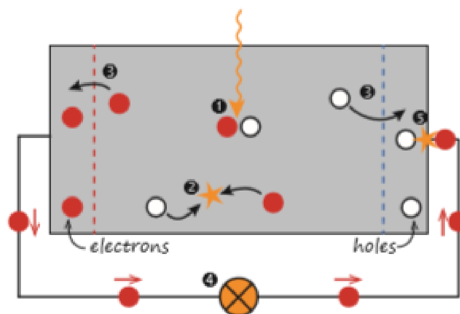

Figure 2.5: A simple and generic solar cell model [1].

2.2. Different types of solar cells

In this section, different PV cells that are relevant for this thesis project are described.

2.2.1. Crystalline silicon

Crystalline silicon (c-Si) cells are the most common cell type in the PV industry. Most of the PV modules installed on rooftops and in PV farms are based on c-Si cells. A c-Si cell is a so-called *diffusion based device*. In such a device the free charge carrier transport is based on diffusion, which means that the free charge carriers can move around freely through the bulk material. In a PV-cell these charge carriers need to be separated before they are able to recombine. In c-Si solar cells, the separation of charge carriers is done by creating a pn-junction. In such a junction, there exists an electric field, which acts as some sort of barrier that only lets through one type of charge carrier (electron or hole).

C-Si has an indirect band gap of around 1.12 eV. Since the bandgap is indirect, relatively high wafer thicknesses of several hundreds of μm are typically used to make sure that a high amount of photons can be absorbed. As explained above, c-Si is a diffusion based device, which means that charge carriers travel a relatively long way before they are separated by a pn-junction. To ensure that a high share of charge carriers is separated before they are able to recombine, the c-Si bulk material needs to have a high diffusion length and a high lifetime for charge carriers. For this reason, the bulk material of c-Si cells has to be of high quality (usually the purity of the Si that is used is over 99.9999%). Typical wafer thicknesses of c-Si cells are in the range of 230 μm. Choosing the absorber layer thickness is a trade-off between using a thick enough layer to absorb as many photons as possible, while ensuring that it is thin enough so that the charge carriers can still be separated before they recombine. The emitter layer of a c-Si solar cell is usually much thinner than the bulk material, namely in the order of 0.3 μm.

2.2.2. Amorphous silicon

Whereas c-Si consists of a highly structured crystal lattice, amorphous silicon (a-Si) is made from a slightly disordered lattice in a so called *continuous random network*. In such a structure there exist valence electrons that cannot form a bond with neighbouring silicon atoms, these electrons are called dangling bonds. Hydrogen can be incorporated into the material to passivate these dangling bonds. Such a material is called hydrogenated amorphous silicon (a-Si:H). Typical hydrogen contents in a-Si:H are between 5% and 15%. The point of distorting the lattice is that a-Si:H has a direct bandgap of 1.6-1.8 eV (depending on the hydrogen contents). The band gap is higher than that of c-Si due to the distortion in bond angles and bond lengths.

Since a-Si:H has a direct band gap, its absorption is higher than that of c-Si. This means that a thinner absorber layer is needed to collect photons. Furthermore, the diffusion length of free charge carriers in a-Si:H is relatively short due to the increased defect density (compared to c-Si). If the material would be doped, this defect density would increase further. To make sure that a high share of charge carriers can still be collected, a trick is applied in a-Si:H devices. The charge carrier separation is not based on a pn-junction, but on a so-called *pin-junction*. In such a device there exists an electric field in the intrinsic layer that is located in between the p- and the n-layer. This electric field ensures that electrons drift towards the n-layer, while holes are guided towards the p-layer. The band diagram of such a device is presented in Figure 2.6. Usually the p-side of the pin-junction of thin film silicon devices is on the front side (where the light enters the cell). This results in higher-efficiency cells, since holes have a shorter diffusion length than electrons and most of the photons are absorbed in the first part of the intrinsic material. Since in pin-devices the charge carrier separation is based on drift instead of diffusion, this type of device is called a *drift device*. Typical intrinsic layer thicknesses of a-Si:H are between 100 and 300 nm.

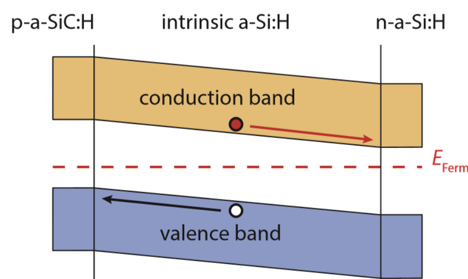

Figure 2.6: The pin-junction of an a-Si:H solar cell [1].

2.2.3. Nanocrystalline silicon

Nanocrystalline silicon (nc-Si) consists of small c-Si grains that are few nm to few tens of nm in size. These grains are embedded in a tissue of a-Si:H. Nc-Si:H bulk material has an indirect bandgap close to 1.12 eV (like c-Si), but is usually still based on a pin-junction. In order to still absorb sufficient photons, the intrinsic layer of a nc-Si:H cell is usually about ten times thicker than that of a typical a-Si:H cell; namely between 1 μm and 3 μm. A common application of nc-Si:H cells is to integrate them as the bottom junction into a tandem cell with a-Si:H. Tandem cells based on these two materials are often called *micromorph cells*. Multi-junction cells are described in more detail in section 2.6.

One of the biggest challenges of a-Si:H and nc-Si:H solar cells is light-induced degradation, also called the *Staebler-Wronski effect*. Over time, recombination of charge carriers create more and more metastable defects in the absorber layers. The increased defect density in the bulk material leads to increased recombination over time. After about 1000 hours of illumination the solar cells stabilize at an efficiency of 85% to 90% of the initial value.

2.3. Loss mechanisms in solar cells

This section describes the different loss mechanisms occurring in photovoltaic solar cells.

2.3.1. Spectral mismatch

The two main loss factors in solar cells are related to spectral mismatch:

- *Non-absorption losses*: The photons with an energy lower than the bandgap energy of the absorber layer are not absorbed, which means that the material is transparent to these wavelengths.

- *Thermalization losses*: The free electrons and holes usually occupy energy levels at respectively the bottom of the conduction band and the top of the valence band. This means that for absorbed photons with an energy higher than the bandgap energy of the absorber layer the extra energy is released as heat.

For low bandgap absorber layers a high current can be generated, but the high thermalisation losses result in a cell with a low voltage. Vice versa a high bandgap absorber can reach a high voltage due to low thermalization losses, but the increased non-aborption losses result in a low current. In order to optimize the spectral utilization of a solar cell, the bandgap has to be chosen such that an optimum is reached in the trade-off between thermalization and non-absorption losses.

2.3.2. Optical losses

Several optical loss factors play a role in solar cells:

- *Reflection losses*: Part of the light incident on a solar cell is reflected at the front interface. The reflection losses can be minimized by making use of anti-reflective coating and surface texturing.

- *Transmission losses*: Even if photons have an energy higher than the bandgap energy of the absorber layer, they can still be transmitted through the material. The probability of transmission of a photon is directly related to the thickness of the absorber layer, since light decays exponentially trough an absorbing medium. The thicker the absorber layer, the lower the optical losses due to transmission. Especially for absorber layers with an indirect bandgap a thicker absorber layer is needed for sufficient photon absorption. Furthermore, light scattering techniques and back reflectors can be used to decrease the transmission losses in solar cells.

- *Shading losses*: If metal front electrodes are used for charge carrier collection at the front of a solar cell, they reflect (or slightly absorb) the photons incident on them. The shading losses can be reduced by minimizing the area of the metal front electrodes or by choosing a transparent alternative.

- *Parasitic absorption*: Absorption of photons in all layers other than the absorber layer do not result in electron-hole pairs that can be successfully collected. Parasitic absorption can be reduced by making the layers other than the absorber layer as thin and transparent as possible.

2.3.3. Electrical losses

The electrical losses in solar cells are mainly related to charge carrier recombination mechanisms and resistive losses:

- *Radiative recombination*: In the direct recombination process, an electron falls back into a hole while emitting a photon. The higher the concentration of free electron and holes, the higher the direct recombination rate is. By using a doped material having either a low amount of free electrons or free holes (low-level injection), the direct recombination rate can be decreased significantly.

- *Shockley-Read-Hall (SRH) recombination*: Impurity atoms or lattice defects introduce energy levels within the band gap, which are called called trap states. If an electron or a hole gets trapped in such a defect, they can consequently recombine more easily. SRH recombination is dominant in amorphous materials, since these have a relatively high defect density. In order to minimize SRH recombination, it is crucial to keep the trap state density as low as possible.

- *Auger recombination*: In semiconductors with an indirect band gap, radiative recombination is limited. In these kind of materials, a three particle process called Auger recombination is dominant. Upon recombination of an electron-hole pair, the momentum is transferred to a third electron or hole present in the lattice. By increasing the doping levels in a semiconductor material the Auger recombination rate can be decreased.

- *Surface recombination*: Dangling bonds at a surface can introduce trap states that facilitate recombination in the same way as SRH recombination. Surface recombination can be minimized by using surface passivation techniques.

- *Resistive losses*: The resistive losses in a solar cell are described by two main parameters, namely the series resistance R_s and the shunt resistance R_{sh}. The series resistance R_s of a solar cell describes the resistance of the main current path through which the charge carriers travel to the external circuit. The main factors contributing to this current are the bulk resistance, the contact resistance between the junction and the electrodes, and the resistance of the electrodes. For an optimal solar cell the R_s should be as low as possible. In contrast, the shunt resistance R_{sh} should be as high as possible. The R_{sh} describes the leakage currents that are present in the solar cell. Leakage currents are mainly caused by current flowing through local defects in the junction or due to shunts at the edges of solar cells. A low R_{sh} is indicative of a shunted cell, in which a significant share of the photogenerated carriers leak away.

2.3.4. The Shockley-Queisser limit

The Shockley-Queisser limit (SQ limit) describes the maximum theoretical efficiency for single-junction solar cells with different bandgaps. In Figure 2.7, the SQ limit and the major loss mechanisms are presented. It can be seen that theoretically, most loss factors in single-junction cells can be reduced fairly well. However, the thermalization and below bandgap losses are responsible for the largest theoretical losses in single-junction solar cells. For the AM1.5 spectrum the efficiency limit is about 33.1% at an optimal bandgap of 1.34 eV.

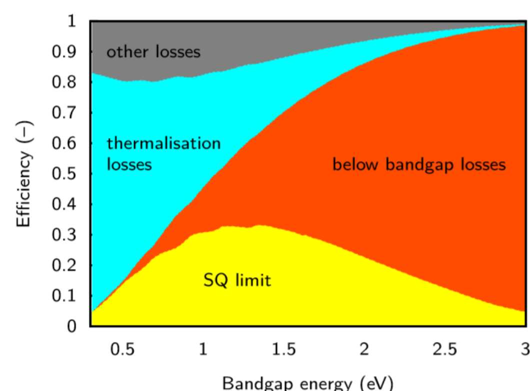

Figure 2.7: The major loss mechanisms in the Shocley-Quisser limit [1].

It has to be noted that the SQ limit does only take radiative recombination into account. This means that it is not directly applicable to crystalline silicon, in which Auger recombination is dominant. The efficiency limit for single-junction silicon solar cells was derived to be 29.43% [23].

2.4. Solar cell parameters

In this section some important solar cell characteristics are explained.

2.4.1. Short circuit current

The short circuit current I_{sc} (A) is the current that flows through the external circuit when the electrodes of a solar cell are short circuited. The short circuit current gives a measure of the maximum current that can be extracted from a solar cell upon illumination from the AM1.5 spectrum. Since the short circuit current is dependent on the area of a solar cell, the non-area dependent short circuit current density J_{sc} (mA/cm^2) is more often used. This makes it easier to compare between solar cells with different areas. The J_{sc} of a solar cell is mainly an interplay between the material band gap, the intrinsic layer thickness, the parasitic absorption and the amount of recombination.

2.4.2. Open circuit voltage

The open circuit voltage V_{oc} is the voltage at which no current flows through the external circuit. It is the maximum voltage that a solar cell can deliver. The V_{oc} is determined by the extent to which the quasi-Fermi levels of electrons E_{Fn} and holes E_{Fp} are able to split. Since the difference between the quasi-Fermi levels is always smaller than the voltage corresponding to the band gap, the qV_{oc} product can never exceed the band gap of a material. Furthermore, the splitting of the quasi-Fermi levels is limited by charge recombination mechanisms. The V_{oc} can be calculated with equation 2.2:

$$V_{oc} \approx \frac{k_B T}{q} \ln\left(\frac{J_{ph}}{J_0}\right) \tag{2.2}$$

In this equation, k_B is the Boltzmann constant, T the temperature, and q the elementary charge constant. Furthermore, the V_{oc} is dependent on the photocurrent density J_{ph} and the saturation current density J_0. The J_{ph} is the current resulting from the flux of photogenerated carriers. The saturation current density J_0 (also known as the dark current density) depends on some fundamental semiconductor parameters and it should be as low as possible to increase the V_{oc}. It has to be noted that the J_{ph} typically only has a small variation, while J_0 can vary by orders of magnitude. Therefore, the V_{oc} of a photovoltaic device is a measure of the amount of recombination.

2.4.3. Fill factor

When a solar cell is operating at its maximum power, this is called the maximum power point P_{mpp}. At P_{mpp} the corresponding maximum power current density (J_{mpp}) and the maximum power voltage (V_{mpp}) are lower than respectively the J_{sc} and the V_{oc}. The fill factor is the ratio between the maximum power and the product of the J_{sc} and the V_{oc}, as given by equation 2.3:

$$FF = \frac{J_{mpp} V_{mpp}}{J_{sc} V_{oc}} \tag{2.3}$$

The variation in fill factor between solar cells made from different materials can be significant, since the maximum achievable fill factor is dependent on the V_{oc} of a solar cell. For a higher V_{oc}, the maximum achievable FF typically increases. However, the FF becomes lower if higher parasitic resistive losses occur in a solar cell.

2.4.4. Efficiency

The efficiency of a solar cell is the ratio between the generated power and the power that is incident on a solar cell I_{in}. A common international standard for the incident power is the radiation from the AM1.5 spectrum, as was explained in section 2.1.1. In the efficiency, all the previously mentioned solar cell characteristics (J_{sc}, the V_{oc}, and FF) come together. The efficiency can be calculated with equation 2.4:

$$\eta = \frac{P_{max}}{I_{in}} = \frac{FF \cdot J_{sc} \cdot V_{oc}}{I_{in}} \tag{2.4}$$

2.5. Light management

If light is incident on a flat surface, part of it is reflected and part of it is refracted. For reflected light, the angle of the scattered light is per definition equal to the incident angle ($\theta_r = \theta_i$). The path of the refracted light is described by Snell's law:

$$n_1 \sin\theta_i = n_2 \sin\theta_t \tag{2.5}$$

The Fresnel equations give insight into the amount of light that is reflected and refracted. The reflection of perpendicular polarized light at a flat interface is given by:

$$r_s = \frac{n_1 \cos\theta_i - n_2 \cos\theta_t}{n_1 \cos\theta_i + n_2 \cos\theta_t} \tag{2.6}$$

The reflection of parallel polarized light is given by:

$$r_p = \frac{n_1 \cos\theta_t - n_2 \cos\theta_i}{n_1 \cos\theta_t + n_2 \cos\theta_i} \tag{2.7}$$

For unpolarized light the total reflectivity R is given by:

$$R = \frac{1}{2}\left(r_s^2 + r_p^2\right) \tag{2.8}$$

For normal incidence the equation of reflectivity reduces to:

$$R_0 = \left(\frac{n_1 - n_2}{n_1 + n_2}\right)^2 \tag{2.9}$$

In equation 2.9, it can be seen that the reflection reduces if the refractive index between two different media is as small as possible. Since the refractive indexes of air (n_{air}) and silicon (n_{Si}) are respectively about 1.0 and 4.3, about 38.8% of light that is of normal incidence to a flat silicon wafer is reflected. If an anti-reflective coating is used at this interface, this reflection can be reduced. The refractive index of an anti-reflective coating is optimal if it has a value of $n_{coating} = \sqrt{n_1 n_2}$. By including an optimal anti-reflective coating at a flat air-silicon interface the reflection reduces from 38.8% to 22.9%. The reflection can be reduced further if more than one interlayers are used. Furthermore, the thickness of an anti-reflective coating can be optimized if the light waves reflected from the air-coating and the coating-silicon interface are in antiphase. This is the case if the thickness of the coating is described by the following equation:

$$n_1 d = \frac{\lambda_0}{4} \tag{2.10}$$

Another way to decrease the front reflection is to use a textured surface. By making use of this approach, incident light that is initially reflected from one part of the textured surface can still be absorbed at another part. This is presented in Figure 2.8. The feature size of the texture has to be chosen wisely; small Rayleigh sized features scatter blue light effectively, while hardly affecting red. Vice versa, large features effectively scatter red light and are less efficient for scattering blue light. In a multi-junction device it is thus important to have a surface texturing with the right feature size at the right interface.

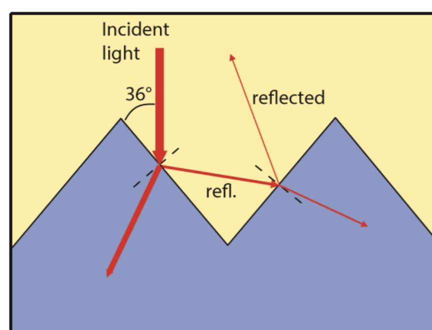

Figure 2.8: The effect of texturing [1].

Another benefit of surface texturing is that it can increase the absorption path length of the incident photons. In the ideal case, in which ideal Lambertian scattering takes place at the front surface and an ideal back reflector is placed at the back of an absorber, a maximal absorption enhancement of $4n^2$ can be achieved, which is often referred to as the Yablonovitch limit.

2.6. Multi-junction PV cells

2.6.1. The concept

In order to increase the voltage and the efficiency of a solar cell, the multi-junction approach can be used, in which two or more cells are stacked on top of each other. Usually, the top cell of a multi-junction solar cell consists of a high-energy bandgap material which absorbs the high-energy photons. Because of the high band gap the top cell has relatively low thermalization losses and can generate a high voltage. The lower cells in the multi-junction have a lower bandgap and thus absorb the photons with a lower energy. In a good multi-junction device the photon absorption should be evenly spread out over the different subcells, since the current of two-terminal multi-junction devices is limited by the subcell with the lowest current. Since the subcells are connected in series, their individual voltages adds up in the complete device.
The current non-concentrator record multi-junction cell consists of four junctions and has an efficiency of 39.2%, which illustrates the potential of multi-junction solar cells. The best multi-junction cells made to date are based on III-V materials. The main advantage of these materials is that subcells with suitable band gaps for usage in multi-junctions can be created with them. In Figure 2.9, the spectral utilization of a III-V based multi-junction cell is compared to that of a single-junction c-Si cell.

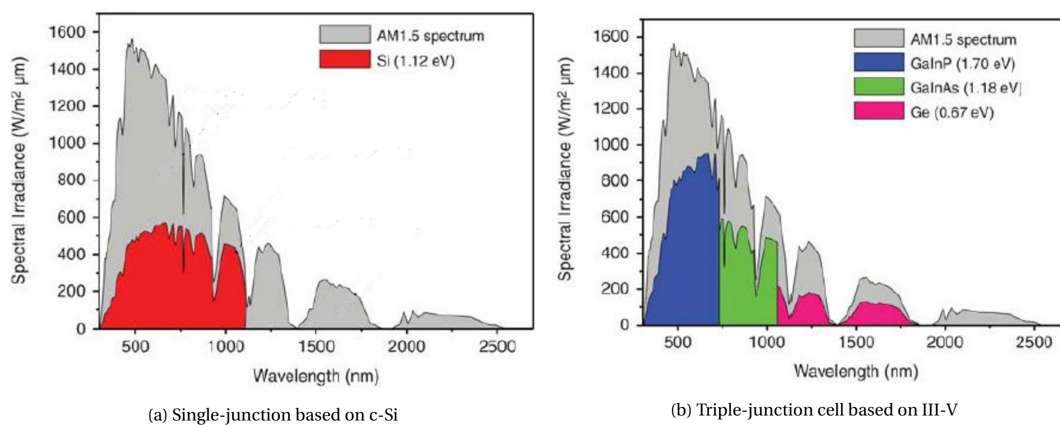

(a) Single-junction based on c-Si

(b) Triple-junction cell based on III-V

Figure 2.9: The spectral utilization of different solar cells [25].

A promising development is that of multi-junction cells with a c-Si bottom cell due to the high market penetration that this technology has reached. As can be seen in Figure 2.10, the theoretical efficiency for triple-junction solar cells with a c-Si bottom cell is highly dependent on the band gaps of the two top cells. In this thesis project, the middle cell based on nc-Si:H and the top cell based on a-Si:H have band gaps of respectively 1.12 eV and 1.6-1.8 eV. As can be seen in Figure 2.10, these band gaps are not ideal in order to reach a highly efficient solar cell. However, it has to be kept in mind that the goal of this thesis project is not to beat the efficiencies of single-junction c-Si technologies. The goal is to reach a multi-junction solar cell that produces a specific voltage in order to be able to drive an electrochemical reaction.

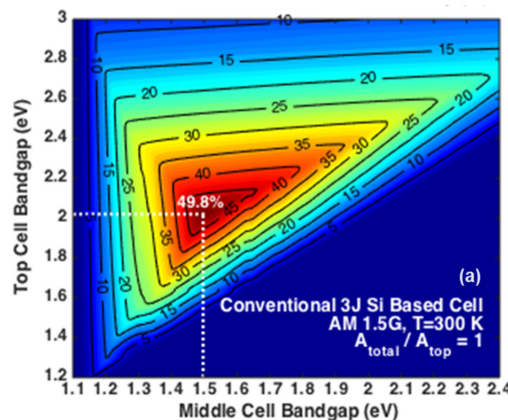

Figure 2.10: Theoretical efficiency of Si-based triple-junction cells as a function of middle and top cell band gaps [24].

2.6.2. Tunnel recombination junctions

If three solar cells would just be stacked directly on top of each other, pn-junctions would be formed in the reverse direction than the pn-junctions of the single-junction solar cells. In order to avoid that these junctions significantly lower the voltage of the complete multi-junction, tunnel recombination junctions (TRJ's) are used in between the different solar cells. In a TRJ the recombination between the holes and the electrons of different solar cells gets facilitated. Now it immediately becomes clear why all the cells should have a similar current; if there are for example more holes than electrons in a TRJ, the recombination (and thus the current of the multijunction) is limited by the amount of electrons. To achieve a high recombination current, the band alignment should be such that the valence band of the p-layer is close to the conduction band of the n-layer. The band diagram of a triple-junction cell with and without TRJ's is sketched in Figure 2.11.

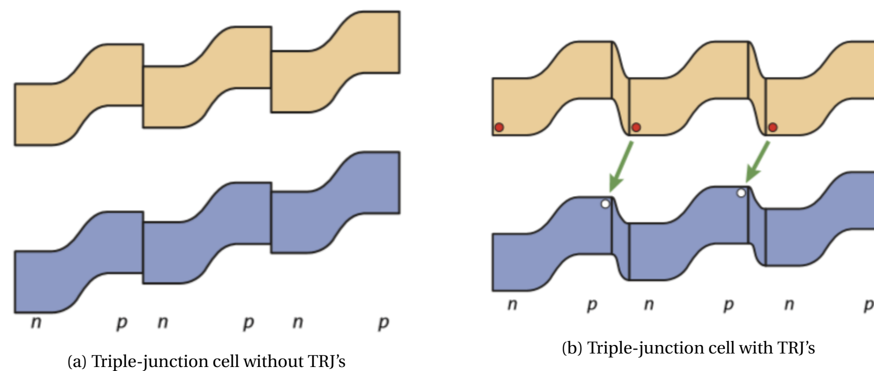

(a) Triple-junction cell without TRJ's

(b) Triple-junction cell with TRJ's

Figure 2.11: Band diagram with and without tunnel recombination junctions [1].

TRJ's play a crucial role in the performance of the multi-junction. The material should have a low resistance to avoid a large voltage drop. Furthermore, a high bandgap material is required so that parasitic absorption in this layer is minimized. Finally, the TRJ is the only layer in a solar cell in which defects might be desirable, especially directly at the p-n interface; they facilitate the recombination of charge carriers. The quality of the TRJ's in a multijunction device particularly affects the open-circuit voltage and the fill factor of a multi-junction device.

2.6.3. Interface engineering

As was discussed earlier in this section, current matching between different subcells is of the utmost importance in multi-junction devices. This can mainly be achieved by choosing the right absorber layer thicknesses. However, it is not always desirable to increase the absorber layer thickness, since this often causes a decrease in the V_{oc}. In these cases an intermediate reflective layer (IRL) can be used at the bottom of a subcell to reflect some photons back into the absorber layer. For example, silicon oxides or a TCO like ZnO:Al are materials that can be used for this application. Note that using a TCO as an IRL between two thin film junctions might laterally connect two shunts due to its high lateral conductivity. Furthermore, light scattering at the IRL due to the presence of a texture can significantly enhance the current density in a device.

3

PV cell production and characterization

In this chapter the production and characterization methods that were used for this thesis are described. The tools used for cell production are described in section 3.1. Step-by-step descriptions of the methods used to texture c-Si wafers and produce PV cells are presented respectively in section 3.2 and 3.3. Finally, the characterization tools used for this thesis are treated in section 3.4.

3.1. Production tools

This section describes the tools that were used for PV cell production during this thesis. These tools are located in the class 10000 or class 100 area of the Else Kooi Laboratory (EKL) at Delft University of Technology. The classification of a cleanroom represents the maximum allowed number of particles with a diameter greater than 0.5 μm per cubic foot of air.

3.1.1. Plasma-enhanced chemical vapour deposition

In Chemical Vapour Deposition (CVD) methods, the growth of a solid material on a substrate is achieved by using chemical reactions of a gas phase precursor. These chemical reactions include the dissociation of the precursor gases in the reaction chamber, which requires external energy. In PECVD methods, a relatively low ambient temperature of about 200 to 300 degrees is typically required, since the dissociation of the precursor gases is assisted by an alternating electric field. This alternating electric field removes the negatively charged electrons from the valence shells of the gas molecules, resulting in high energy electrons that are subsequently able to dissociate the gas molecules. The neutral dissociated particles diffuse and attach themselves onto the substrate, while the charged particles drift to the grounded electrode under the influence of the electric field. A PECVD reaction chamber is schematically represented in Figure 3.1. The type of Si layer that is grown with the PECVD method can be influenced by varying the pressure, temperature, frequency, power, or by adding precursor gases.

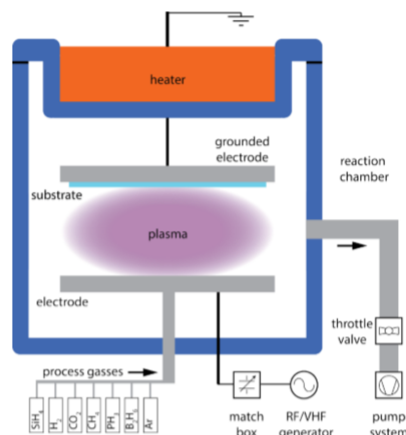

Figure 3.1: Schematic representation of the plasma-enhanced chemical vapour deposition setup [26].

In this thesis, the PECVD technique was used to deposit silicon layers of thin film cells as well as passivation layers and doped layers of the SHJ cells. All PECVD processes in this thesis were performed with a tool called AMIGO (made by Elettorava S.p.A.). In order to prevent cross-contamination, this tool makes use of different chambers for different types of layers. Substrate holders can be loaded into AMIGO via a load-lock chamber. The other chambers in the tool are a transfer chamber, a p-type layer chamber (DPC1), an n-type layer chamber (DPC2), an i-a-Si:H layer chamber (DPC3), an i-nc-Si:H layer chamber (VHF, DPC4), a multi-process chamber (DPC5), and a sputtering chamber (DPC6). DPC4 operates at 40 MHz (VHF), while the other chambers operate at 13.56 MHz (RF).

3.1.2. Low pressure chemical vapour deposition

Being a CVD method, low pressure chemical vapour deposition method (LPCVD) includes the dissociation of precursor gases in the reaction chamber. However, unlike PECVD, this method does not make use of a plasma. During LPCVD, SiH_4 is dissociated by heating up the reaction chamber to relatively high temperatures, typically in the range of 600 °C. In this thesis, the LPCVD technique was used to deposit poly-Si and a-Si layers for the sacrificial layer texturing method.

3.1.3. Radio-frequency magnetron sputtering

Sputtering is a common physical vapour deposition (PVD) method. In PVD methods, materials are typically transformed from a condensed phase into a vapour phase and then back into a condensed phase. During radio-frequency (RF) magnetron sputtering, an argon plasma is generated by an RF generator. Positively charged argon ions bombard the surface of a target, which allows these atoms to escape from the target and shift to the vapour phase. Subsequently, these atoms form a layer on a substrate that is placed in the reaction chamber. The RF sputtering process is presented in Figure 3.2.

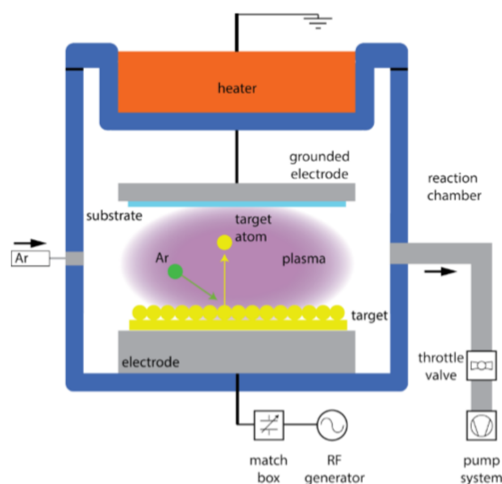

Figure 3.2: Schematic representation of a sputtering process [26].

In this thesis two RF sputtering tools were used. The first one, which is DPC6 of AMIGO, was used for the deposition of ZnO:Al. This tool has a target consisting of 98% ZnO and 2% Al. The second tool, called ZORRO, was made by Polyteknik and is used for the deposition of ITO. The target of this tool consists of 10% SnO_2 and 90% In_2O_3.

3.1.4. Metal evaporation

Evaporation is a PVD technique in which a material condensates on the surface of a substrate after being heated above its melting point. The technique is mostly used for the deposition of metallic layers. The heating can typically be done in two different ways. In the first one, called resistive evaporation, a material is heated resistively by applying a high current, which is presented in Figure 3.3a. During electron beam evaporation, the heating is done by irradiating a water-cooled crucible by an electron beam. This process is presented in Figure 3.3b.

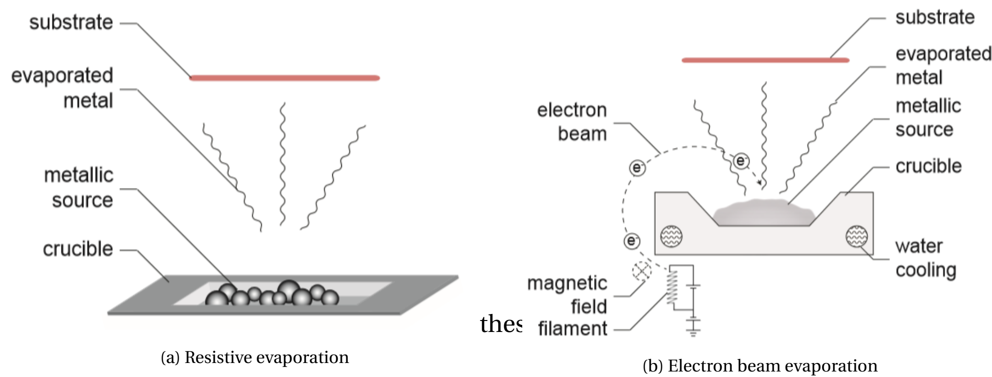

Figure 3.3: Schematic representation of two types of metal evaporation [27].

In this thesis all metal evaporation was performed using the Provac PRO500S. This is a single chamber high-vacuum system equipped with both an electron gun and a boat for thermal evaporation. The machine applies electron beam evaporation for melting Al and Cr, while Ag is melted resistively. The desired contact dimensions can be deposited on the substrate by making use of a mask.

3.1.5. Ion implantation

Ion implantation is a technique that is typically used to introduce doping atoms into a semiconductor wafer. The process starts by extracting positively charged ions from the ion source. A magnetic field generated by an electromagnet allows the selection of the right type of ion from the beam. The ions are then bombarded at the substrate after being accelerated by an electric field. The ions penetrate the solid material and are slowed down due to interaction with the Si atoms. For the relatively heavy ions used in this thesis, this is caused by collisions between impinging ions and Si atoms [28]. The process is represented schematically in Figure 3.4. The ion implanter used for this thesis project is the Varian Implanter E500HP, which can accelerate ions with an energy up to 250 keV. The available implantation atoms are B, P, Ar, As and BF_2.

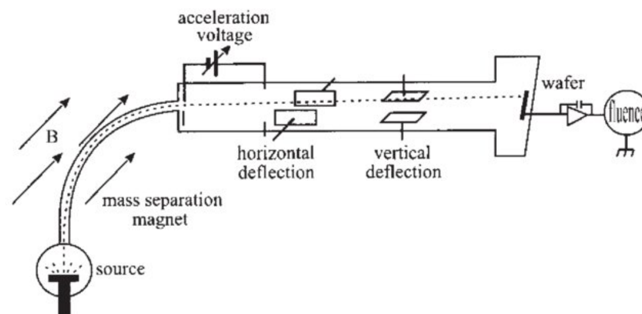

Figure 3.4: Schematic representation of ion implantation [29].

3.2. Texturing methods of c-Si wafers

This section treats the different methods that were used in this thesis to achieve a smooth surface texture on silicon wafers. More specifically, the next three sections describe the smooth pyramid texturing method, the photolithography texturing method, and the sacrificial layer texturing method.

3.2.1. Smooth pyramid texturing

This section describes the smooth pyramid texturing method. The first step of this method is to perform a regular anisotropic etch with a solution containing TMAH, which is used to create a random pyramid texture. This surface texture is widely used for c-Si solar cells. Pyramids are formed at the surface because the anisotropic etching solution etches different crystal facets of crystalline silicon at different rates. When a c-Si wafer is exposed to this etching solution, the <100> plane is etched at a higher rate than the <111> plane.

In the smooth pyramid texturing method, this pyramid-textured wafer is then exposed to an isotropic

etch. By doing so, the pyramidal features have been demonstrated to become more smooth [20]. The reason for this is that isotropic etching solutions etch all crystal facets of crystalline materials at the same rates.

More specifically, the smooth pyramid etching texturing method consists of the following steps:

1. 15 minutes of etching in a 25:3:100 TMAH (25%): ALKA-TEX.8 (ISRA):H_2O solution at 85 °C
2. 3 minutes of rinsing in water
3. 5 minutes of etching in a 1:6:3 HF (40%):HNO_3 (69%):H_2O solution at room temperature
4. 3 minutes of rinsing in water

SEM Figures of a full pyramid surface texture as well as a smooth pyramid surface texture are presented in Figure 3.5.

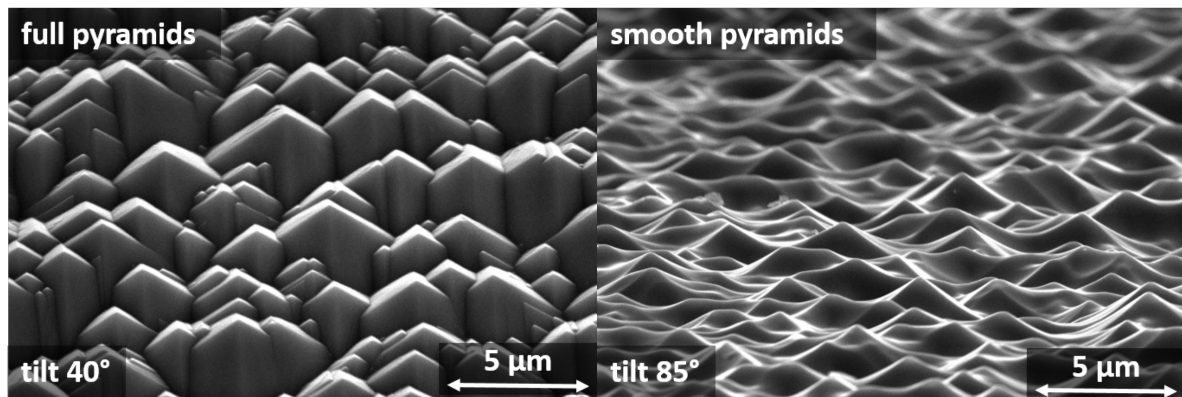

Figure 3.5: SEM images of the full pyramid surface texture (left) compared to the smooth pyramid surface texture (right).

3.2.2. Photolithography texturing

The photolithography texturing method is based upon the following steps, which are presented visually in Figure 3.6:

1. In a wet oxidation process at 1100 °C, the top layer at the surface of a flat silicon wafer is oxidized for 16 minutes, resulting in a 300 nm layer of silicon dioxide on both sides of the wafer.
2. The wafer is coated with a 1.4 μm layer of positive photoresist on the front side, which is added on top of the SiO_2 layer.
3. Lithographic exposure is performed at an energy of 140 mJ/cm^2. The mask used has small holes of 5 μm that are uniformly spaced in the vertexes of an equilateral triangle with a period of 15 μm. In the stepper that is used, the image projected is a 5 times reduction compared to the mask. This results in a pattern in the photoresist with a hole diameter of 1 μm and a period of 3 μm.
4. During development the areas of the photoresist that were irradiated during the lithographic exposure are removed. At these areas the silicon dioxide layer is exposed again.
5. The pattern that was created in the photoresist is now transferred to the SiO_2 using a wet etch in buffered hydrofluoric acid. Once the pattern has been transferred, the remaining photoresist is removed using aceton. The result is a flat silicon wafer with a SiO_2 etching mask.
6. The wafers are now exposed to an isotropic 1:35:14 HF (40%):HNO_3 (69%):H_2O etching solution. This results in a silicon wafer with an hexagonal texture, since the holes of bare silicon are etched quicker than the parts of the wafer that are covered by the SiO_2 mask.

The resulting hexagonal texture from this process is presented in Figure 3.6b. All the steps described above are treated in more detail in the master thesis project of M. Wiering [22].

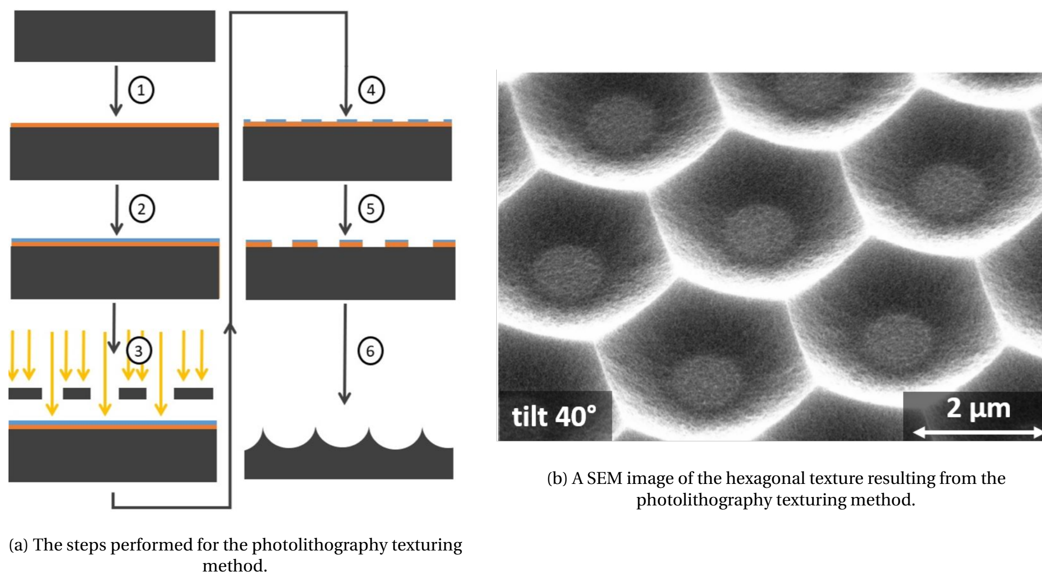

(a) The steps performed for the photolithography texturing method.

(b) A SEM image of the hexagonal texture resulting from the photolithography texturing method.

Figure 3.6: The steps performed in the photolithography texturing method as well a tilted SEM image of the end result [22].

3.2.3. Sacrificial layer texturing

The sacrificial layer texturing method is based upon the following steps, which are presented visually in Figure 3.7a:

1. The native oxide layer on the c-Si wafer is removed by performing Marangoni drying.
2. A poly-Si or a-Si layer is grown on both sides of a silicon wafer using an LPCVD furnace. The thickness of this layer was varied in between 250 and 1500 nm.
3. The amorphous silicon layer is implanted with ions. These can be different kinds of ions, but the most common one used in this thesis project was argon. After implantation the wafers are annealed at a temperature of 950 °C or 1050 °C. This step results in a poly-Si layer with a relatively large grain size.
4. The wafers are now exposed to an isotropic 1:35:14 HF (40%):HNO_3 (69%):H_2O etch. A random texture is created, because the etching speed differs for different areas of the polycrystalline layer.

The resulting random texture from this process is presented in Figure 3.7b. All the steps described above are treated in more detail in the master thesis project of M. Wiering [22].

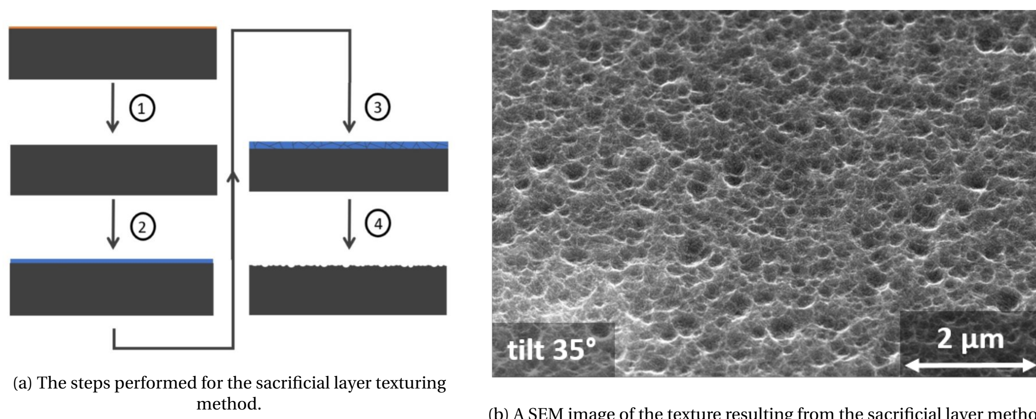

(a) The steps performed for the sacrificial layer texturing method.

(b) A SEM image of the texture resulting from the sacrificial layer method.

Figure 3.7: The steps performed in the sacrificial layer texturing method as well a SEM image of the resulting texture [22].

3.3. Cell production method

This section treats the production method that was used for the different type of solar cells made in this thesis.

3.3.1. Silicon heterojunction single junction cell production

This section treats the production method for the c-Si bottom cell. The chosen cell concept is the silicon heterojunction (SHJ) solar cell, which is known for its high V_{oc} [30]. The wafers used for these cells are polished n-type TOPSIL wafers with a thickness of 260-300 μm, a diameter of 10 cm, and a <100> orientation. The process used for manufacturing the cells is described step by step below, visually clarified in Figure 3.8. The PECVD deposition parameters for each of the layers are given in Table 3.1.

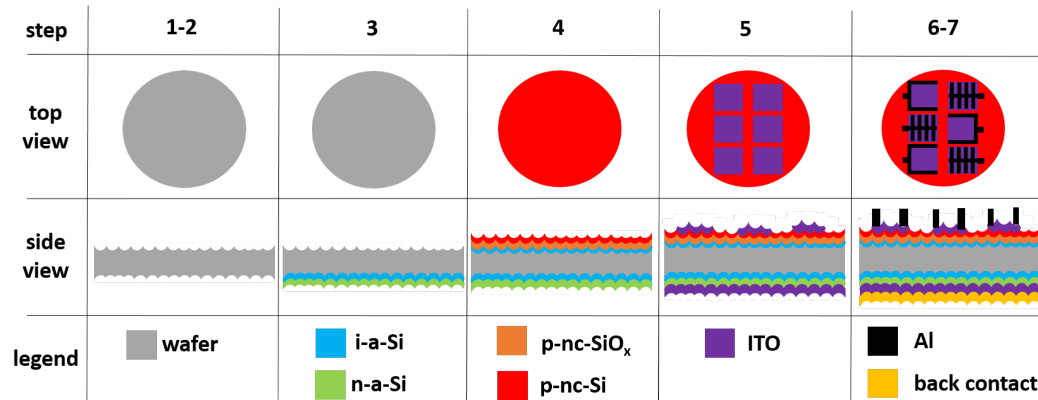

Figure 3.8: A schematic representation of the process of creating an SHJ cell.

1. The first step of the process is to texture the wafer. This is done with either one of the three texturing methods presented in section 3.2.

2. After texturing, the wafer undergoes three consecutive nitric acid oxidation (NAOC) cycles, as suggested by Deligiannis et al. [31]. One cycle consists of the following steps:

    - 10 minute dip in an HNO_3 (99%) bath at room temperature to remove organic contaminants
    - 5 minutes of rinsing in DI water
    - 10 minute dip in an HNO_3 (69%) bath at 110 °C to remove metal contaminants.
    - 5 minutes of rinsing in DI water
    - 5 minute dip in an HF (0.55%) bath at room temperature, which removes the formed oxide layer
    - 5 minutes of rinsing in DI water

    During the third and last NAOC cycle, the HF dip is replaced by Marangoni drying. This allows the wafers to be taken out of the HF (0.55%) bath completely dry [32]. The next step is performed as soon as possible after Marangoni drying to prevent the formation of a native oxide layer at the wafer surface [33]. During this thesis project, the wafers were often cut in half before the next step.

3. The n-side of the wafer is deposited with PECVD in AMIGO. The n-side deposition of the wafer consists of the following steps:

    - Deposition of an i-a-Si:H layer for surface passivation
    - 80 s of hydrogen plasma treatment (HPT) for passivation of dangling bonds [34]
    - Deposition of an n-a-Si:H layer

4. The wafer is taken out of AMIGO and flipped in order to process the p-side. The p-side deposition consists of the following steps:

    - Deposition of an i-a-Si:H layer for surface passivation
    - 80 s of HPT
    - i-nc-Si treatment for passivation and to minimize the incubation layer thickness [35]
    - Deposition of p-nc-SiO_x
    - Deposition of p-nc-Si

5. The next step is to deposit a TCO layer on both sides of the wafer, which consists of indium tin oxide (ITO). This deposition is done with the sputtering tool ZORRO. For the p-side of the wafer masking is used to deposit 24 square cells, each having a 4 mm x 4 mm area and a thickness of 75 nm. On the n-side an ITO layer with a thickness of 150 nm is sputtered on the full wafer area.

6. A 500 nm thick aluminium front grid is deposited through electron beam evaporation with the Provac PRO500S. Masking is used to deposit two front grid types alternating each other. The first front grid type consists of aluminium lines deposited along the sides of the 4 mm x 4 mm TCO pattern. The second type is a grid consisting of one busbar and several fingers deposited on top of the 4 mm x 4 mm TCO cells.

7. The final step is the deposition of a back contact on the n-side of the wafer. This deposition is performed with the PROVAC PRO500S. The back contact consists of the subsequent deposition of 300 nm Ag, 30 nm Cr and 800 nm Al.

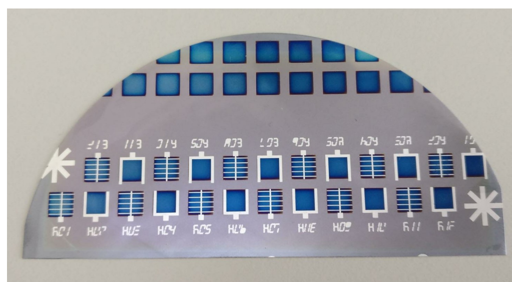

Figure 3.9: Front side of a SHJ sample

Table 3.1: Layer-by-layer PECVD deposition parameters for the performed SHJ cell production.

Layer	Wafer side (n/p)	Thickness (nm)	SiH_4 (sccm)	H_2 (sccm)	CO_2 (sccm)	B_2H_6/H_2 (200 ppm) (sccm)	PH_3 (sccm)	Pressure (mbar)	Power (W)
i-a-Si	n	10	40	0	0	0	0	0.7	2.8
HPT	n	-	0	200	0	0	0	2.2	9
n-a-Si	n	10	40	0	0	0	11	0.6	4
i-a-Si	p	10	40	0	0	0	0	0.7	2.8
HPT	p	-	0	200	0	0	0	2.2	9
i-nc-Si	p	-	1.2	120	0	0	0	4	13
p-nc-SiO_x	p	4	0.8	170	1.4	10	0	2.2	11
p-nc-Si	p	15	0.8	170	0	10	0	2.2	13

3.3.2. Nanocrystalline single junction cell production

This section treats the production method of single-junction nc-Si:H cells that was used in this thesis. The process used for manufacturing the cells is described step by step below, visually clarified in Figure 3.10. The PECVD deposition parameters of the layer-by-layer deposition are given in Table 3.2.

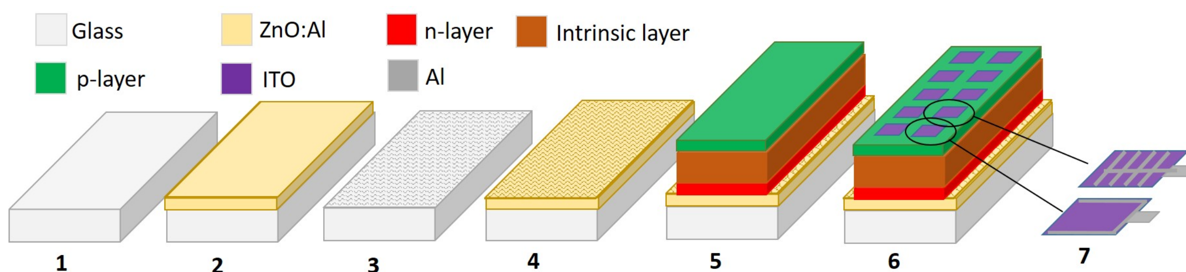

Figure 3.10: A schematic representation of the process of creating a nc-Si:H cell.

1. Firstly, a 10 cm x 10 cm piece of a Corning Eagle XG glass substrate is manually cut into 2.5 cm x 10 cm pieces with a diamond pen. Subsequently the pieces are cleaned with aceton (10 minutes) and IPA (10 minutes) in an ultrasonic bath.
2. Since nc-Si:H layers attach better on textured than on flat glass, it was chosen to texture the glass substrates with a previously developed sacrificial layer method [36]. A sacrificial 700 nm aluminum-doped zinc oxide (ZnO:Al) layer is sputtered onto the glass at a temperature of 300 °C in DPC6 of AMIGO.
3. Subsequently, the ZnO:Al layer is etched away in a 1:3:6 HF (40%):HNO_3 (69%):H_2O solution. Since the etching solution does not etch isotropically through the polycrystalline ZnO:Al layer, this process results in textured glass. Subsequently the pieces of textured glass are cleaned with aceton (10 minutes) and IPA (10 minutes) in an ultrasonic bath.
4. A 700nm aluminum-doped zinc oxide (ZnO:Al) layer is sputtered onto the glass at a temperature of 400 °C. This layer serves as the back contact of the PV cell. A transparent back contact is chosen because the eventual nc-Si:H cell will be the middle cell in a multijunction. If a back reflector would be applied, the current density would be overestimated with respect to the current in the subcell of the final device. This ZnO:Al deposition is also done in DPC6 of AMIGO.
5. The PV cell is deposited in an nip-substrate configuration with the PECVD deposition cluster tool AMIGO. The exact layer-by-layer deposition parameters are presented in Table 3.2. The sides of the sample are covered with high temperature-resistent tape, so that this part of the ZnO:Al can serve as the back contact once the complete cell is finished.
6. The front TCO made of ITO is deposited with the sputtering tool ZORRO. Masking is used to deposit 24 square cells, each having a 4 mm x 4 mm area and a thickness of 75 nm.
7. A 500 nm thick aluminium front grid is deposited through electron beam evaporation with the Provac PRO500S. Masking is used to deposit two front grid types alternating each other. The first front grid type consists of aluminium lines deposited along the sides of the 4 mm x 4 mm TCO pattern. The second type is a grid consisting of one busbar and several fingers deposited on top of the 4 mm x 4 mm TCO cells. Both of these grid types are presented in Figure 3.10.

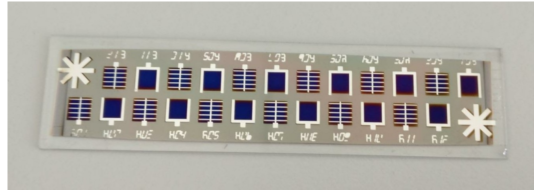

Figure 3.11: Front side of a nc-Si:H sample

Table 3.2: Layer-by-layer PECVD deposition parameters for the performed nip-deposited nc-Si:H cell production.

Layer	**Thickness (nm)**	**SiH_4 (sccm)**	**H_2 (sccm)**	**CO_2 (sccm)**	**B_2H_6/H_2 (200 ppm) (sccm)**	**PH_3 (sccm)**	**Pressure (mbar)**	**Power (W)**
n-nc-Si	8	1	120	0	0	2	1.6	11
n-nc-SiO_x	8	1	120	0.8	0	2	1.6	11
n-nc-SiO_{x+}	8	1	120	1.6	0	2	1.6	11
n-a-Si	3	40	0	0	0	11	0.6	4
HPT	-	0	200	0	0	0	1.2	8
i-nc-Si seed	25	1.2	120	0	0	0	4	40
i-nc-Si	3000	3.5	120	0	0	0	4	40
i-SiO_x	3	0.8	170	1.6	0	0	2.2	12
p-nc-SiO_x	12	0.8	170	1.6	10	0	2.2	12
p-nc-Si	3	0.8	170	0	20	0	2.2	35
HPT	-	0	200	0	0	0	1.2	8

3.3.3. Multi-junction cell production

For this thesis project, several micromorph (nc-Si:H/a-Si:H tandem) cells are made. The production method of these tandem cells is similar to that of the nc-Si:H single junction cells. However, in the case of a micromorph cell, an extra nip stack of the a-Si:H cell is now added on top of the nc-Si:H cell. The layer-by-layer deposition parameters for this a-Si:H cell are presented in Table 3.3.

Table 3.3: Layer-by-layer PECVD deposition parameters for the performed nip-deposited a-Si:H top cell production.

Layer	Thickness (nm)	SiH_4 (sccm)	H_2 (sccm)	CO_2 (sccm)	B_2H_6/H_2 (200 ppm) (sccm)	PH_3 (sccm)	Pressure (mbar)	Power (W)
n-nc-SiO$_x$	5	1	108	1.6	0	3	1.5	11
n-a-Si	25	40	0	0	0	11	0.6	4
i-a-Si	150	2	200	0	0	0	10	9
i-nc-Si	5	0.8	170	0	0	0	2.2	35
p-nc-SiO$_x$	10	0.8	170	1.8	25	0	2.2	12
p-nc-Si	3	0.8	170	0	20	0	2.2	35

The production method of SHJ/nc-Si:H tandem cells is similar to that of single-junction SHJ cells. However, in the case of such a tandem cell, an nc-Si:H cell is added on top of the p-layer of the wafer. Similarly, for the production of the triple-junction cells, an extra a-Si:H cell is added on top of the nc-Si:H cell.

3.4. Characterization tools

This section treats the different characterization tools that were used in this thesis project. The PV cell characterization was always done as quickly as was practically possible after processing, mostly to avoid cell degradation and oxidation of silicon surfaces. Furthermore, before measuring the performance of cells, the samples were always annealed at 130 °C for 30 minutes to improve the contact at the TCO-metal interface.

3.4.1. Spectroscopic ellipsometry

Spectroscopic Ellipsometry (SE) is an optical measurement technique that can be used to characterize thin film layers. With SE the film thickness and optical constants can be determined by fitting the measurement data to an appropriate model. Accurate film thickness measurements are extremely important for this thesis, since these are used to determine the PECVD deposition time that is needed to grow a certain thickness. The SE tool used for this thesis is the M-2000DI made by J.A. Woollam, of which the operation is schematically presented in Figure 3.12.

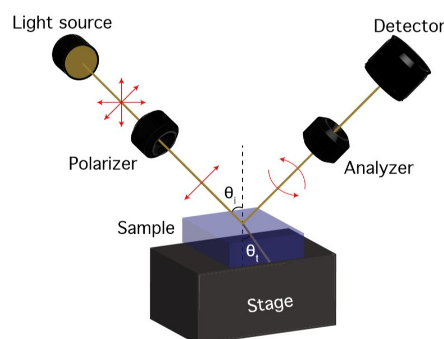

Figure 3.12: Schematic representation of a SE setup [31].

The SE technique depends upon light reflection from a sample. Light with its electric field vector oscillating in the plane of incidence is called P-polarized light. Light with its electric field vector oscillating perpendicular to the plane of incidence is called S-polarized light. As shown by the Fresnel equation in section 2.5, S- and P-polarized light reflect differently from a surface. In an SE measurement, a beam with a set S- and P-polarized light source is incident on a sample. Part of the light is reflected at the air-film interface, while another part is reflected from the underlying interface. The reflected light beams and its polarization states are compared

to the ones that were incident on the sample. If a model that assumes certain unknown parameters is then used, the thickness and optical constants of the film can be determined.

3.4.2. Raman spectroscopy

Raman spectroscopy is an optical measurement technique that can be used to obtain information about the molecular bonding and the structure of a material. In this thesis it was mainly used to compare the crystalline fraction of different materials. The technique is based upon illuminating a sample with a monochromatic light source. Most of the scattered light incident on the sample is scattered elastically, which is often referred to as Rayleigh scattered light. However, a small part is also scattered inelastically, which is called Raman scattered light. This light excites an electron from a molecule in the sample, after which it relaxes again and emits a photon. Hence, the Raman scattered photons have exchanged energy with the molecular vibrations in the material after scattering. In a Raman spectrometer, the Rayleigh scattered light is filtered out, since only the Raman scattered photons contain information about the material. The Raman spectrometer used in for this thesis is the InVia Raman Microscopy by Renishaw. This tool uses an Ar-ion laser for green light and a HeNe laser for red light.

The data of a Raman measurement is typically plotted in a graph with the Raman shift (cm^{-1}) in frequency on the x-axis and the relative intensity of the Raman scattered light on the y-axis. In literature a wide range of peaks in the Raman spectrum has been investigated and linked to all sorts of silicon bonds and structures [37] [38]. The presence of amorphous and crystalline silicon is characterized by peaks in the the Raman spectrum at respectively 480 cm^{-1} and 520 cm^{-1} [37].

3.4.3. Photoconductance lifetime measurement

Photoconductance lifetime measurements can be used to determine the minority carrier lifetime τ_{eff} of a wafer. The τ_{eff} is an important indicator of the surface passivation quality and amount of emitter dopant diffusion in a SHJ solar cell. A schematic representation of the lifetime measurement setup is presented in Figure 3.13.

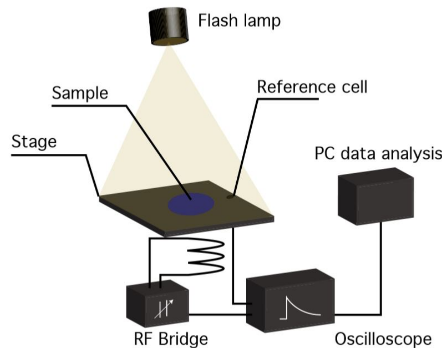

Figure 3.13: Schematic representation of the lifetime tester used in this thesis project [31].

In order to perform a lifetime measurement, a silicon wafer sample is placed on a stage. The flash lamp above the sample flashes for a short period of time (1s or 1/64s). The photoconductance of the wafer changes as a result of the changing minority carrier density in the wafer. However, after the lamp stops flashing, the photoconductance returns to its initial value after some time. This change in photoconductance is measured by a coil that is coupled to an RF Bridge. This information is then used to determine the τ_{eff} of the wafer [39]. τ_{eff} is the time constant at which the excess carrier concentration decays exponentially once the external generation from the lamp is no longer taking place. Often it is interpreted as the average time needed for excess minority carriers to recombine after photoexcitation.

3.4.4. J-V measurement

A current-voltage (J-V) characteristic is an important indicator of the performance of a solar cell. It provides some important external parameters, the most important being J_{sc}, V_{oc}, FF, R_s, R_{sh} and η. In this project, the J-V characteristics of the manufactured solar cells are measured with an AAA class Wacom WXS156S-L2 solar simulator. A schematic representation of the J-V measurement setup is presented in Figure 3.14.

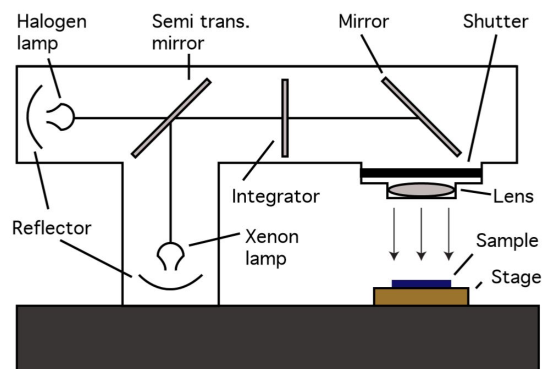

Figure 3.14: Schematic representation of the J-V characteristic measurement setup [31].

For these measurements, the standard test conditions (STC) are approximated, which correspond to an irradiance of the AM1.5 spectrum and a temperature of 25 °C. The AM 1.5 spectrum is simulated by combining the spectra of a Halogen lamp and a Xenon lamp. During a J-V measurement, the solar cell is connected to a load, whose resistive power is incrementally changed during the measurement. Such a measurements shows the produced current of the solar cell at different voltages.

3.4.5. External quantum efficiency

An external quantum efficiency (EQE) measurement of a solar cell provides the fraction of photons incident on a solar cell that result in successfully collected electron-hole pairs as a function of the wavelength. With an EQE measurement a more accurate J_{sc} value can be obtained than with a J-V measurement. The error in a J-V measurement is mainly caused by the lamps not perfectly matching the AM1.5 spectrum and the uncertainty in the solar cell area. On the other hand, for an EQE measurement only a dot with adjustable size and a controllable amount of photons needs to be incident on the solar cell that is being measured. The setup used in this thesis is presented schematically in Figure 3.15.

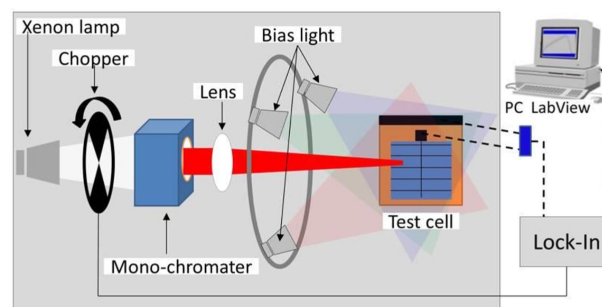

Figure 3.15: Schematic representation of the EQE measurement setup [40].

In the setup used in this thesis, light from a lamp is first chopped by an optical chopper, after which one wavelength is filtered by a monochromator. While the light is concentrated on the solar cell with a lens, the resulting photocurrent is measured with an electrometer. Bias lights can be used to measure an EQE of a subcell of a multijunction cell. The EQE setup can perform measurements in the 300 to 1200 nm wavelength range. In this thesis all measurements are performed with a step size of 10 nm.

3.4.6. Transmittance and reflectance

Transmittance and reflectance losses can give insight into the optical losses in a solar cell. These kind of measurements can help to create a better understanding of an EQE graph, by showing whether losses at specific wavelengths are optical or electrical. In this thesis, both transmittance and reflection measurements were performed with the PerkinElmer Lamda 1050 UV/VIS spectrometer

During a reflectance measurement, monochromatic light is focused into an integrating sphere, which includes InGaAs and PbS detectors. The inside walls of this sphere are made of spectralon, a highly reflective and scattering material. Firstly, a reference measurement is performed, during which spectralon material

is placed at the back of the sphere, ideally resulting in 100% reflection at each of the different wavelengths. Thereafter, a sample is placed at the back of an integrating sphere. The reflectance can now properly be determined for each wavelength by comparing the results to the reference measurement. Transmittance measurements are performed similarly, except for the fact that the sample is now placed in front of the integrating sphere. The reference measurement is now performed without any sample in front of the sphere, ideally resulting in 100% transmittance.

3.4.7. Scanning electron microscopy

Scanning electron microscopy (SEM) is a technique that produces images of a sample by scanning the surface with a focused beam of electrons. This techique makes use of electrons rather than visible light, because a higher resolution can be achieved with the shorter wavelength of electrons. Electrons originating from an electron source are accelerated towards the sample surface using the positive charge of an anode. An image is created by analyzing the back scattered (elastic scattering) and secondary electrons (inelastic scattering) from the sample surface.

In this thesis project, SEM images are used to visualize the surface texture resulting from the sacrificial layer texturing experiments. The SEM type that is used is the Nova NanoSEM 50 Series from the company FEI, located in the Kavli Institute of Quantum Nanoscience in Delft.

3.4.8. Atomic force microscopy

Atomic force microscopy (AFM) is a technique that can create a 3D-image of a sample surface at a high resolution. The technique uses a tip to raster-scan the surface, all the wile recording the interaction with the sample. In order to do this, the tip deflection during the raster-scan is constantly measured with a laser. The tip deflection indicates whether the tip is in contact with the surface (repulsive force), whether it is close to the surface (attractive force), or whether it is relatively far from the surface (no deflection at all).

The AFM measurements in this thesis project were performed with the Bruker Dimension Icon with Scan Assist, which is located in the Kavli Institute of Quantum Nanoscience in Delft.

4

Optimizing the sacrificial layer texturing method

In this chapter an optimization of the sacrificial layer texturing method is described. A step-by-step description of this texturing method was given earlier in section 3.2.3. During previous research in the DISCO project, it proved to be challenging to create surface textures with a mean crater diameter over 320 nm with the sacrificial layer texturing method. This means that the surface features of the sacrificial layer method are significantly smaller than that of the other texturing methods tried in this thesis. The aim of this chapter is to further optimize the sacrificial layer texturing method by achieving a larger crater size and roughness, which should be done for two reasons. Firstly, wafer surfaces with larger craters were shown to have lower reflectance [22]. Secondly, it has been demonstrated that texture-induced defects in nc-Si:H solar cells are avoided if the period of the underlying texture is equal or larger than the nc-Si:H layer thickness [41].

The reason that craters are formed during the sacrificial layer method is that the etching solution does not etch isotropically through the sacrificial layer. Since the formation of crystalline grains in the sacrificial layer is assumed to be responsible for this anisotropic etching behaviour, the mechanisms responsible for grain growth are presented in section 4.1. The subsequent sections 4.2-4.4 treat an optimization of the sacrificial layer thickness, the annealing temperature and time and the implantation dose. After some different implantation ions are investigated in section 4.5, the conclusions are presented in section 4.6. Furthermore, an optimization of the etching time is presented in Appendix A. The characterization of the created textures is done with SEM images taken at a tilt angle of 35 °C and AFM measurements. The wafer type used for this chapter is the polished n-type TOPSIL wafer with a thickness of 260-300 μm, a diameter of 10 cm, and a <100> orientation.

4.1. Grain growth mechanisms in the sacrificial layer

This section provides some background into the grain formation processes in the sacrificial layer. With this background in mind, the results presented in the next sections can be interpreted more easily.

It has been shown in previous studies that annealing an a-Si layer deposited with LPCVD results in poly-Si with a high crystalline fraction [42]. The reason that a-Si films crystallize upon annealing is that the Gibbs free energy of the crystalline phase is lower than that of the amorphous phase [43]. The transition from the amorphous to the crystalline phase only becomes allowed if the the mobility of the Si atoms is high enough, which can be induced by a thermal anneal of 600 °C or higher [44]. However, if the sacrificial layer texturing method is performed by etching away a non-implanted, fully crystallized poly-Si layer, this results in a smooth surface without any perceptible craters. The most likely explanation for this result is that the solution etches isotropically through such a poly-Si layer due to the relatively small size of the grains.

Craters are formed in the resulting surface texture if the sacrificial layer is implanted before annealing. A likely explanation for this is that the implantation step contributes to the formation of larger grains in the sacrificial layer. This can cause the anisotropic etching behaviour through the sacrificial layer, as the etchant goes faster through the porous grain boundaries than through the crystalline phase. Hence, for a better understanding of the sacrificial layer method, it is useful to explain why larger grain growth occurs if the sacrificial layer is imlanted before the annealing step:

1. *Implantation amorphizes the grains that are present in the as-deposited poly-Si layer*: It has been shown that during thermally induced crystallization, grains that are present in a silicon layer grow to include the space formerly occupied by amorphous tissue [45]. This process continues until full crystallization of the film has occurred. As presented in Figure 4.1, the as-deposited poly-Si layer from the LPCVD has a significant poly-Si peak. However, the crystalline peak in the Si layer completely disappears after it is implanted with Ar. If less grains survive the implantation, larger grains are allowed to form in the sacrificial layer. In a completely amorphous film, the grain growth upon annealing becomes no longer dominated by the growth of grains that were already present in the silicon layer, but by spontaneously nucleated grains [46].

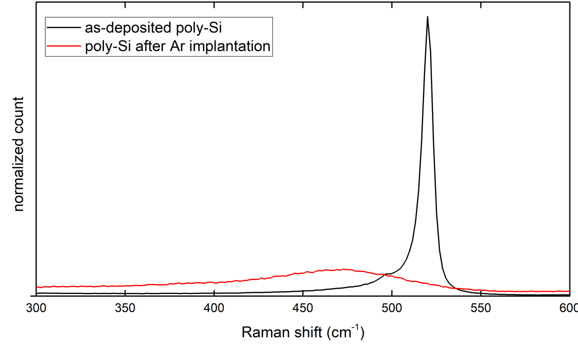

Figure 4.1: Raman measurement of a 1500 nm thick sacrificial layer in as-deposited and implanted state. The implantation step was performed with argon ions at a dose of $1 \cdot 10^{16}$ ions/cm^2 and an energy of 250 keV. The measurements were performed at a laser excitation energy of 514 nm. The Raman spectra are normalized with respect to the total amount of counts.

2. *Implantation leads to the development of larger grains due to an increasing silicon self-diffusion coefficient*: Wada et al. have shown that impurity doping in poly-Si leads to an increase in the silicon self-diffusion coefficient, which enhances the formation of large grains upon annealing. In their work, it was shown that a thermal anneal can cause small grains in highly doped layers with P and As to merge and form larger grains [47]. This effect is further explained by Mei et al., who state that in this case atoms migrate from one grain to another, hereby reducing the free energy [48]. Hence, the formation of larger grains in an implanted with respect to a non-implanted sacrificial layer might be explained by the fact that the presence of ions increases the silicon self-diffusion coefficient, hereby facilitating different grains to merge during annealing. That the implantation dose has a direct effect on the poly-Si material is demonstrated by Raman measurements as a function of dose presented in Figure 4.2. Since the observed difference is subtle, the spectra are normalized with respect to the highest count and presented on a semilog scale. The most likely explanation for this observation is a difference in grain size in the poly-Si layer. As the grain size increases, it is possible that slightly more amorphous tissue remains present at the grain boundaries. In order to confirm this theory, a Transmission Electron Microscopy (TEM) measurement could be performed in future research.

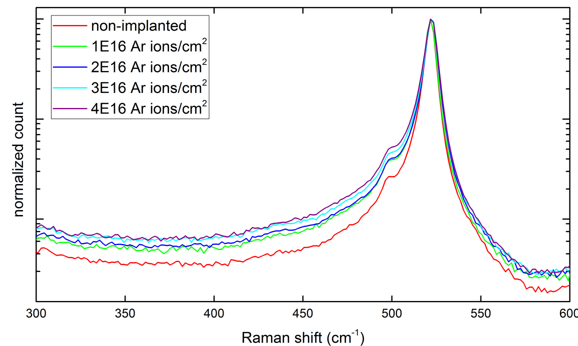

Figure 4.2: Raman spectra of sacrificial layers with different Ar implantation doses. The layers had a thickness of 1500 nm and were annealed at 1050 °C for 1h. The measurements were performed at a laser excitation energy of 514 nm. The Raman spectra are presented on a semilog scale and normalized with respect to the highest count.

4.2. Sacrificial layer thickness

In this section an optimization of the sacrificial layer thickness is described. Previous experiments have shown that the optimal sacrificial layer thickness lies somewhere in between 500 nm and 2000 nm [22]. Hence, the sacrificial layers tried for this experiment vary in between 250 nm and 1500 nm in steps of 250 nm. The SEM images of the resulting surface textures are presented in Figure 4.3. These sacrificial layers were all etched for 45 seconds per 250 nm. More information about the etching time is presented in Appendix A.

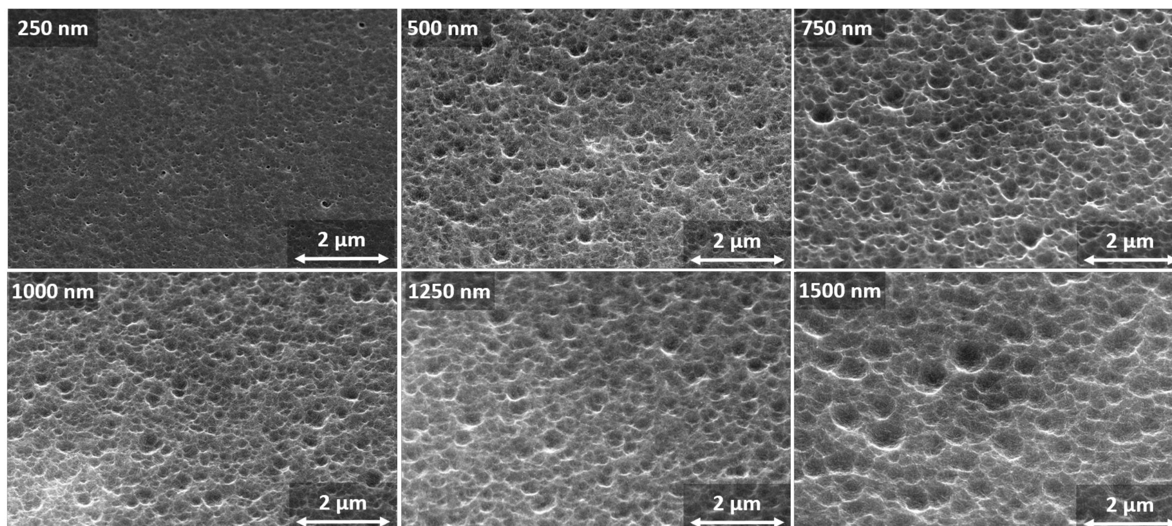

Figure 4.3: SEM images from the surface texture resulting from different sacrificial layer thicknesses. These sacrificial layers were all implanted with Ar at an implantation energy of 250 keV and a dose of $1 \cdot 10^{16}$ ions/cm^2. The wafers were annealed at 950 °C for 60 minutes.

Based on the SEM pictures of Figure 4.3, the craters in the surface texture clearly increase in size if the layer thickness is increased from 250 nm to 750 nm. In between sacrificial layer thicknesses of 750 nm and 1250 nm, the resulting crater size seems to be relatively stable. Upon a sacrificial layer increase to 1500 nm, the crater size of the surface texture again increases slightly. These trends from the SEM Figures are confirmed by the AFM analysis results, which are presented in Table 4.1. Hence, the overall results from this experiment suggest an increase in crater size and average roughness if the sacrificial layer thickness increases from 250 nm to 1500 nm. However, as was shown in previous experiments, the trend of increasing crater size for increasing sacrificial layer thickness does not continue for layers with a thickness of 2 μm or thicker [22].

The most likely explanation for this observation is that the grain size in the sacrificial layer is an interplay between the thickness of the sacrificial layer and the ion concentration through the sacrificial layer with respect to the c-Si interface. On the one hand, the results of this section suggest that larger grains can be formed if the sacrificial layer thickness is increased. On the other hand, the layer should remain thin enough to ensure that sufficient ions penetrate deep enough into the sacrificial layer to enhance the formation of large grains close to the c-Si interface.

Table 4.1: AFM analysis of the surface texture resulting from different sacrificial layer thicknesses

Sacrificial layer thickness (nm)	Mean pore diameter (nm)	Average roughness (nm)
250	359 ± 6	5.3
750	417 ± 8	18.2
1000	385 ± 5	15.3
1250	382 ± 5	16.6
1500	456 ± 11	22.7

4.3. Annealing optimization

In this section an optimization of the annealing time and temperature is described. In several studies the annealing time and temperature was shown to be an important parameter affecting the grain size development

in poly-Si layers [47] [49]. The annealing step was performed for durations of 10 minutes, 30 minutes, 60 minutes and 90 minutes at temperatures of both 950 °C and 1050 °C. All sacrificial layers for this experiment had a thickness of 1000 nm and were implanted with Argon at an implantation energy of 250 keV and a dose of $1 \cdot 10^{16}$ ions/cm^2. The SEM images from the resulting surface textures of this experiment are presented in Figure 4.4. The results from the AFM analysis of these surface textures are presented in Figure 4.5.

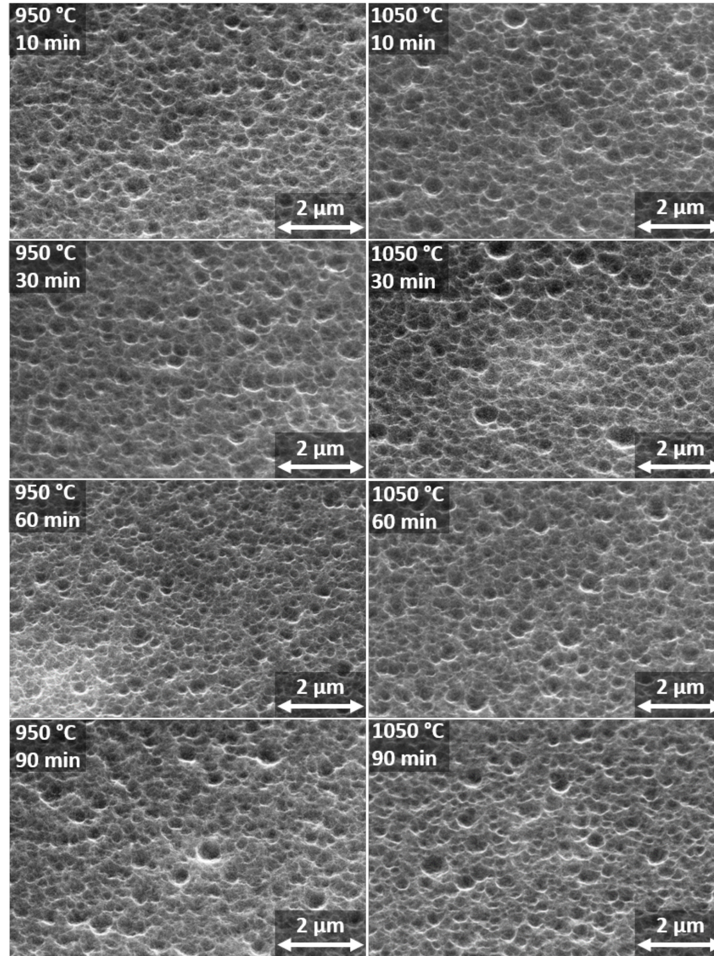

Figure 4.4: SEM images from the resulting surface texture from different annealing times at temperatures of 950 °C and 1050 °C. These sacrificial layers all had a thickness of 1 μm and were implanted with Ar at an implantation energy of 250 keV and a dose of $1 \cdot 10^{16}$ ions/cm^2.

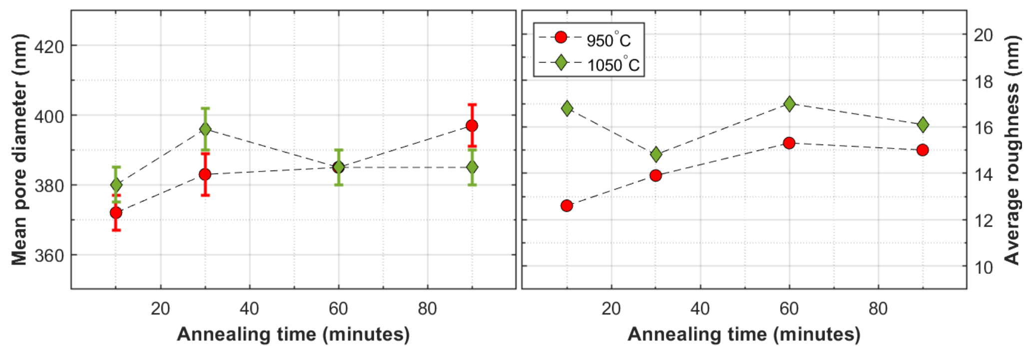

Figure 4.5: AFM analysis of the surface texture resulting from different annealing times and temperatures.

The results of the experiments in this section do not indicate that the annealing temperature and time have a

direct impact on the crater size of the resulting surface texture. The mean pore diameter and average roughness do not change significantly for the different annealing steps that were tried. An explanation for this might be that every annealing step that was tried provides the grains in the sacrificial layer with enough energy to grow to their maximum size. Nevertheless, the resulting surface texture from an annealing step of 1050 °C seems to be slightly rougher than that of 950 °C. Since annealing at 1050 °C for for 60 minutes resulted in the largest pore diameter and average roughness, this annealing step was chosen for future experiments.

4.4. Implantation dose

In this section an optimization of the implantation dose in the sacrificial layer is discussed. Several studies have established that the grain size in poly-Si layers after annealing increases if the implantation dose of phosphorus and arsenic ions is increased [47] [50] [51]. Previous sacrificial layer method experiments showed that the crater size increases for a higher doping level with Argon ions [22]. However, the highest doping level that was tried in this work was $1 \cdot 10^{16}$ ions/cm^2. This section treats a further increase of the doping level on the resulting surface texture of the sacrificial layer method. More specifically, the implantation dose of argon ions was varied in between $1 \cdot 10^{16}$ ions/cm^2 and $4 \cdot 10^{16}$ ions/cm^2 in steps of $1 \cdot 10^{16}$ ions/cm^2. The SEM images from the resulting surface textures of this experiment are presented in Figure 4.6.

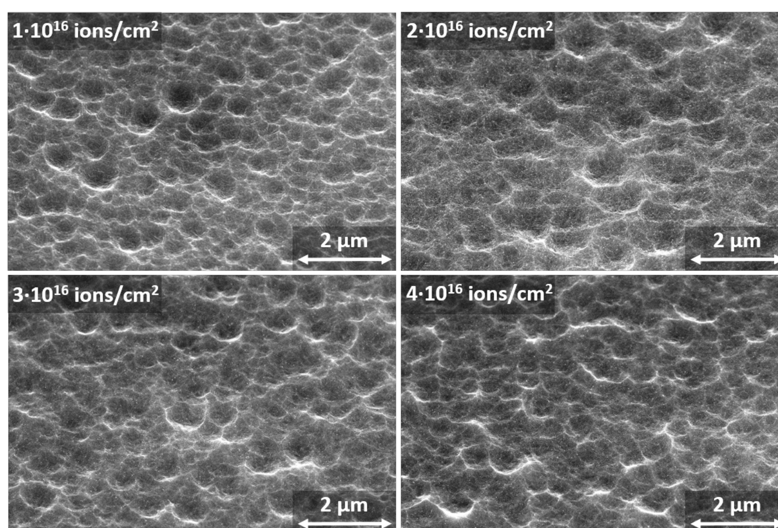

Figure 4.6: SEM images from the resulting surface texture from different Ar implantation doses at an energy of 250 keV. The sacrificial layer thickness for this experiment was kept constant at 1500 nm and an annealing step of 60 minutes at 1050 °C was used.

As can be seen in Figure 4.6, the crater size in the resulting surface texture seems to increase as the implantation dose is increased from $1{\cdot}10^{16}$ ions/cm^2 to $2{\cdot}10^{16}$ ions/cm^2. This can be explained by the fact that poly-Si tends to form larger crystal grains during a thermal anneal if the sacrificial layer is implanted with more ions. However, the crater size does not significantly increase further if the implantation dose is increased to $3{\cdot}10^{16}$ ions/cm^2 or $4{\cdot}10^{16}$ ions/cm^2.

4.5. Different ions

Whereas in the previous sections only implantation with argon was treated, this section discusses implantation with different ions. More specifically, the surface texture resulting from sacrificial layer implantations with boron difluoride (BF_2) and arsenic (As) are described. Previous experiments have shown that implanting sacrificial layers with thicknesses of 1 or 2 μm with either of these two ions does not result in as large craters as argon implantation [22]. It is likely that this is caused by the ions penetrating less deep into the sacrificial layer for similar implantation energies, because they are more heavy than argon. This can not be solved by increasing the implantation energy, since the implanter was already operating at its maximum implantation energy of 250 keV. Hence, for the experiments in this section, relatively thin sacrificial layer thicknesses of 250 nm and 500 nm were used. For both of these thicknesses, implantations with both BF_2 and As were carried out. The SEM images from the resulting surface textures of this experiment are presented in Figure 4.7.

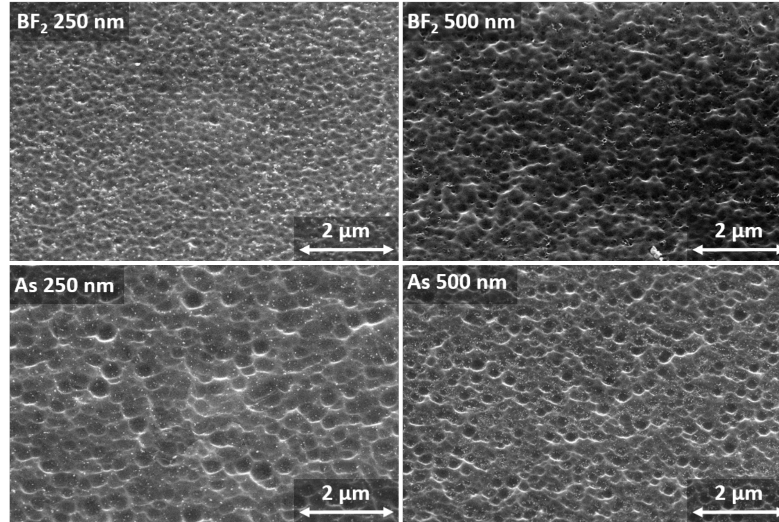

Figure 4.7: SEM images from the resulting surface texture from implantation with BF_2 and As for sacrificial layer thicknesses of 250 nm and 500 nm. The implantation doses and energy were respectively $2 \cdot 10^{16}$ ions/cm^2 and 250 keV. The annealing step was performed for 60 minutes at 1050 °C.

In Figure 4.7, it is observed that craters can be formed with BF_2 and As implantation if the sacrificial layer thickness is kept at relatively low values of 250 nm and 500 nm. However, at these relatively low thicknesses the resulting craters remain relatively small, presumably because the formed grains in the sacrificial layer are smaller.

4.6. Conclusions

In this chapter, the sacrificial layer texturing method was optimized. It was demonstrated that the crater size of the resulting surface texture increases if the argon ion implantation dose is increased from $1 \cdot 10^{16}$ ions/cm^2 to $2 \cdot 10^{16}$ ions/cm^2, presumably because larger grains are formed upon annealing if the ion concentration is higher. For higher implantation doses, the crater size seems to saturate. Raman measurements confirmed that the ion concentration affects the crystalline grain development, as a subtle decreasing trend in the crystallinity of the annealed sacrificial layer was observed as the implantation dose was continuously increased from a non-implanted layer up to $4 \cdot 10^{16}$ ions/cm^2 in steps of $1 \cdot 10^{16}$ ions/cm^2. In order to confirm that this decreasing crystallinity indeed is caused by the formation of larger grains, TEM measurements could carried out in future research.

Furthermore, it was demonstrated that the crater size in the resulting surface texture is an interplay between the sacrificial layer thickness and the position where ions end up with respect to the c-Si interface. On the one hand, the crater size increases continuously for argon-implanted sacrificial layers as the thickness is increased from 250 nm to 1500 nm, presumably because larger crystalline grains can be formed in a sacrificial layer with a higher thickness. On the other hand, if the thickness of the sacrificial layer is increased to 2000 nm or higher, it is observed that the crater size in the resulting surface texture decreases. For these thicknesses, it is assumed that for the used implantation energy an insufficient amount of ions ends up close to the c-Si interface. If relatively large grains are only formed in the top part of the sacrificial layer, the desired anisotropic etching effect fades out before the etchant reaches the c-Si interface. The sacrificial layer thickness was found to be optimal at 1500 nm, which resulted in a mean pore diameter crater increase from 385 nm to 456 nm compared to the previously used thickness of 1000 nm.

Varying the annealing temperature between 950 °C and 1050 °C did not significantly impact the resulting surface texture. Neither did varying the annealing time between 10 and 90 minutes. This suggests that all of these annealing steps provide the sacrificial layer with sufficient energy to fully crystallize.

Finally, the crater size resulting from sacrificial layers implanted with BF_2 and As were compared with Ar-implanted layers. Since BF_2 and As ions are heavier than Ar ions, they penetrate less deep into the sacrificial layer if the same implantation energy is used. As the used implanter was already operating at its maximum implantation energy, relatively low sacrificial layer thicknesses had to be used in order to achieve sufficient ion concentration near the c-Si interface. These thinner sacrificial layers implanted with BF_2 and As resulted in smaller craters than were demonstrated for Ar-implanted sacrificial layers with a higher thickness.

5

Optimizing the silicon heterojunction cell performance

In this chapter an optimization of the single-junction silicon heterojunction (SHJ) PV cell is described. Since the aim of this thesis is to integrate the SHJ into a triple junction device as the bottom cell, the surface of the wafer has to consist of a smooth surface texture. In the DISCO project, crack-free nc-Si:H layer growth has been demonstrated on three different smooth surface textures. These textures are the smooth pyramid texture, the photolithography texture, and the sacrificial layer texture, for all of which a step-by-step production method was presented earlier in section 3.2. In this chapter, the photovoltaic performance of these different surface textured are compared. Because of the limited time that was available for the project, the SHJ performance could not be optimized for all the different surface textures. The best performing surface texture is identified, and only this one is fully optimized. The integration of this optimized SHJ cell into multi-junction devices is described in chapter 7.

The wafers used for the single-junction SHJ cells are polished n-type TOPSIL wafers with a thickness of 260-300 μm, a diameter of 10 cm, and a <100> orientation. The SHJ cells are processed by stripping the native oxide layer from the wafer surface, after which the surface passivation process is performed as soon as possible. Firstly the n-side is processed, consisting of a 14 nm i-a-Si:H layer, 80 s of HPT, and a 10 nm n-layer. The p-side of the wafer is then processed by depositing a 14 nm i-a-Si:H layer, 80 s of HPT, a 4 nm p-SiOx and a 12 p-nc-Si layer. Subsequently, 75 nm and 150 nm ITO layers are sputtered on respectively the p-side and the n-side of the wafer. The final step in the process is to deposit the a 500 Al front grid on the p-side of the wafer, and a back contact on the n-side consisting of 300 nm Ag, 30 nm Cr and 800 nm Al. A more thorough description of the step-by-step procuction process of SHJ cells in this thesis was given in section 3.3.1.

Section 5.1 treats a comparison between the passivation quality of different a-Si:H types. The subsequent sections 5.2 and 5.3 treat an optimization of the a-Si:H layer thickness and the p-layer thickness. The conclusions are presented in section 5.4. The V_{oc} and FF values presented in this chapter were determined by taking the average value from J-V measurements of the 5 best cells of each sample. The J_{sc} values presented are the average values of EQE measurements of the 2 best cells. For PECVD deposition on textured pyramid silicon substrates, it is typically assumed that the deposition rate is 1.7 times slower than on flat substrates [52]. This assumption is adopted for the tried smooth textured substrates in this thesis, which might cause a slight underestimation of the layer thicknesses.

5.1. Passivation of the smooth surface textures with different a-Si:H layers

In this section, the passivation quality of different i-a-Si:H passivation layers are compared for different surface textures. The function of the i-a-Si:H layer is to passivate the dangling Si bonds at the c-Si surface after the native oxide layer is removed. If this layer would be left out of the device, there would be a higher defect density at the c-Si/p-layer interface due to unpassivated dangling bonds [53]. In this case, increased SRH recombination would deteriorate the minority charge carrier lifetime (τ_{eff}), mainly affecting the V_{oc} of the eventual device.

The i-a-Si:H passivation layers that were tried were 14 nm undiluted a-Si:H, 14 nm diluted a-Si:H, and a bilayer consisting of 7 nm undiluted and 7 nm diluted a-Si:H. The exact deposition parameters, as well as

the resulting lifetimes are presented in Table 5.1. The lifetime measurements presented here were performed after the n-layer, the p-layer, and the TCO layers were deposited. For this experiment, wafers of the smooth pyramid and the sacrificial layer texture were cut in half and processed in the same holders. Since there was only place for two half wafers in one holder, this section does not include results for the passivation of photolithography textured wafers.

Table 5.1: A comparison between different a-Si passivation layer types for wafers with a smooth pyramid and sacrificial layer texture.

	Deposition parameters				**Smooth pyramid texture**		**Sacrificial layer texture**
a-Si layer type (nm)	**SiH_4 (sccm)**	**H_2 (sccm)**	**Pressure (mbar)**	**Power (W)**	**Lifetime (μs)**	**Voc (mV)**	**Lifetime (μs)**
undiluted	40	0	0.7	2.8	3643	713	3
diluted	10	30	1.4	3	1345	685	5
bilayer	40 10	0 30	0.7 1.4	2.8 3	3577	664	13

As presented in Table 5.1, the highest lifetime for the smooth pyramid texture was achieved by depostion through an undiluted SiH_4 plasma. This is an interesting result, since previous research shows that increasing the H_2 dilution of the SiH_4 plasma up to a certain point improves the surface passivation [54]. The reason for this might be that the a hydrogen diluted silane plasma results more easily in epitaxial growth on top of the used smooth pyramid texture than on the regular random pyramid texture. Unintentional epitaxial growth in the a-Si:H passivation layer is detrimental for the surface passivation quality [55]. The smooth pyramid texture has a relatively large fraction of exposed <100> crystal orientations compared to the regular pyramid texture, for which mainly <111> facets are exposed. For clarification, the <100> and the <111> orientations of a silicon crystal are presented schematically in Figure 5.1. Epitaxial growth is more likely to occur on <100> crystal orientations than on <111> orientations [53]. This is possibly related to the fact that the <100> orientation has two exposed dangling bonds per surface atom, with respect to one surface bond for the <111> facet. Consequently, the rotational freedom of the growing surface on the <100> orientation is reduced compared to the <111> surface, increasing the probability of crystalline epitaxial growth [21]. It is well known that H_2 favourably etches relatively weak amorphous bonds, which increases the probability of epitaxy as the H_2 dilution in a SiH_4 plasma increases. Hence, the SiH_4 plasma should be undiluted to prevent epitaxial growth in the i-a-Si:H passivation layers for the smooth surface textures in this thesis project.

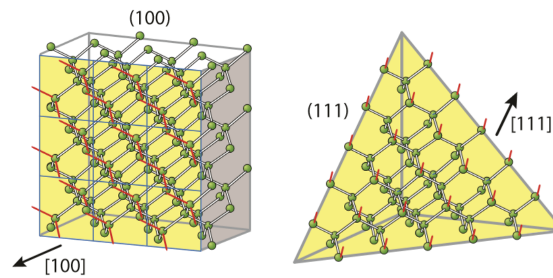

Figure 5.1: The <100> and the <111> surfaces of a silicon crystal [1].

Furthermore, Table 5.1 shows that the lifetimes of wafers with a sacrificial layer texture are three orders of magnitude lower than those of the smooth pyramid texture. Consequently, none of the SHJ solar cells with the sacrificial layer surface texture resulted in reasonably performing solar cell devices. There are several possible reasons why the wafers with a sacrificial layer texture could not be properly passivated. One explanation for this could be that the sacrificial layer was not completely removed after etching, which would result in high SRH recombination rates at the c-Si/poly-Si interface. Another explanation could be that this surface texure has a relatively high fraction of exposed <100> crystal facets exposed compared to the smooth pyramid texturing method. Finally, it could be possible that some argon ions penetrate into the top layer of the crystalline wafer, hereby affecting the crystal structure and creating additional defects. Because only limited time was available, the passivation of the sacrificial layer texture is not treated further in this thesis and requires further research,

5.2. Intrinsic a-Si:H passivation layer thickness

In this section the influence of the a-Si:H layer thickness on the passivation quality and solar cell performance is treated. Since the sacrificial layer textured wafers did not result in good lifetimes in the previous section, the photolithography textured wafers were tried for the experiment in this section instead. This time, half smooth pyramid and photolithography textured wafers were processed in the same holders. For this experiment, the undiluted a-Si:H type from Table 5.1 was used. The lifetime for different a-Si:H thicknesses on wafers with the smooth pyramid and the photolithography texture are presented in Figure 5.2. These lifetime measurements were performed after the intrinsic, n- and p-layer deposition.

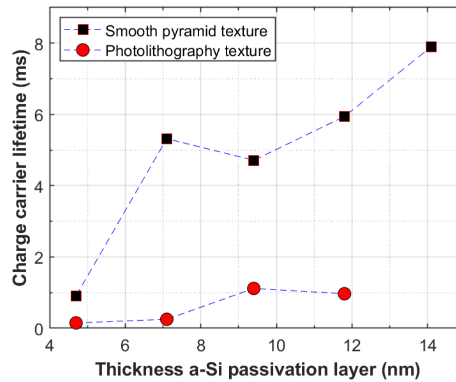

Figure 5.2: Charge carrier lifetime of the smooth pyramid and the photolithography textured wafers at a carrier density of 10^{15} cm^{-3} for different a-Si:H layer thicknesses. The p- and n-layer thicknesses were respectively 19 nm and 10 nm.

From the measurements presented in Figure 5.2, it is observed that lifetimes over 5 μs are achieved for wafers with a smooth pyramid texture for a-Si:H passivation layers of 7 nm or higher. The lifetime increases as the a-Si:H passivation layer becomes thicker, for which there are several explanations possible. Firstly, dangling bonds at the c-Si surface might be passivated more effectively as there is more hydrogen available in a thicker a-Si:H passivation layer. Secondly, the cause of lower lifetimes for thin passivation layers might be that the growth is not perfectly uniform. The probability of certain areas of the peaks or valleys of the surface texture ramaining unpassivated increases for thinner layers. Thirdly, the possibility of a few nanometers of epitaxial growth at the c-Si/a-Si:H interface cannot be fully excluded. For thicker a-Si:H layers, the likelihood of the a-Si:H layer epitaxially connecting the c-Si wafer surface with the p-layer decreases [56]. Furthermore, it is observed in Figure 5.2 that the wafers with a photolithography texture have a lower lifetime than the wafers with a smooth pyramid texture. The most likely explanation for this observation is that this surface texure has a relatively high amount of exposed <100> crystal facets exposed compared to the smooth pyramid texture.

For both the smooth pyramid and the photolithography texture, the solar cell performance for different a-Si:H passivation layer thicknesses are presented in Figure 5.3. It is shown that the J_{sc} of the smooth pyramid surface texture does slightly increase as the a-Si:H layer becomes thicker. This effect is associated with decreasing parasitic absorption in the a-Si:H passivation layer in the low wavelength range, as presented in the EQE graph in Figure 5.4. However, it stands out that the J_{sc} of the photolithography textured wafers with a 4.7 nm and a 7.1 nm i-a-Si:H thickness is significantly lower than those for higher thicknesses. This is caused by a lower EQE in the high wavelength range, as presented in Figure 5.5. The reason for this might be related to the fact that the half wafers with i-a-Si:H thicknesses of 4.7 nm and a 7.1 were placed in the same holder during the TCO sputtering process. For example, the reflection at the n-a-Si:H/TCO interface might be lower for these two samples.

Furthermore, the V_{oc} clearly shows an increasing trend for a thicker a-Si:H layer. This effect is attributed to better surface passivation, previously indicated by an increasing τ_{eff}. The V_{oc} of the photolithography textured surface follows the same trend as the smooth pyramid surface, but is around 50 mV lower. This is within expectation due to the lower τ_{eff}. The decreasing trend in FF for both textures is caused by an increasing series resistance for a thicker a-Si:H passivation layer. For example, the R_s of the SHJ with photolithography texture decreases from 4.2 $\Omega\cdot m^2$ to 3.2 $\Omega\cdot m^2$ as the a-Si:H passivation layer is decreased from 14.1 to 9.4 nm. This relation between the R_s and the FF is in line with earlier reports [57]. Hence, choosing the i-a-Si:H passivation layer thickness is a trade-off between V_{oc} and FF. The optimal SHJ solar cell efficiency was achieved for an i-a-Si:H passivation layer thickness between 5 nm and 9 nm.

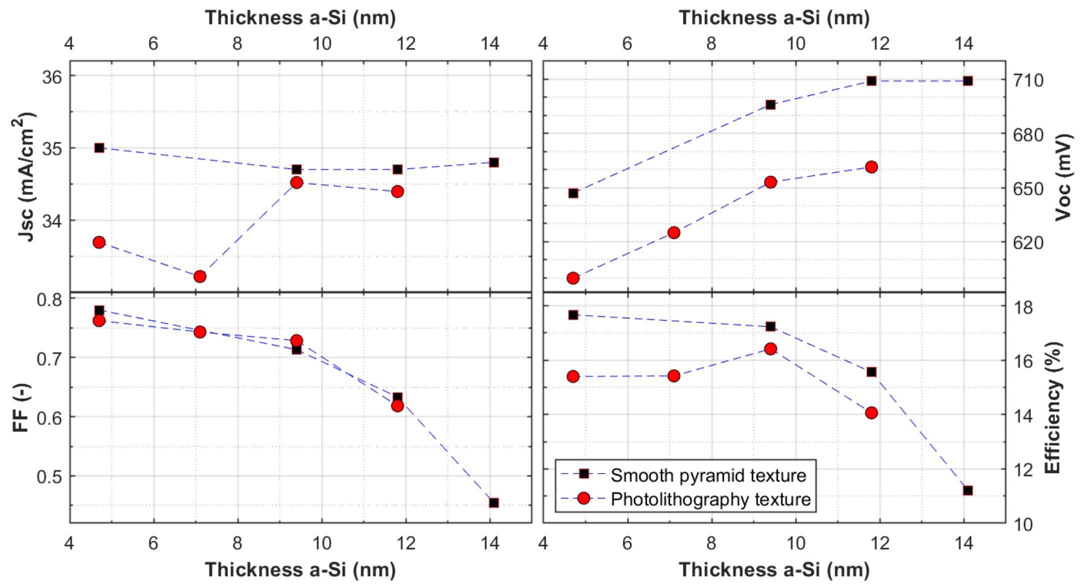

Figure 5.3: External solar cell parameters of SHJ cells with the smooth pyramid and photolithography texture for different a-Si:H passivation layer thicknesses. The p- and n-layer thicknesses were respectively 19 nm and 10 nm.

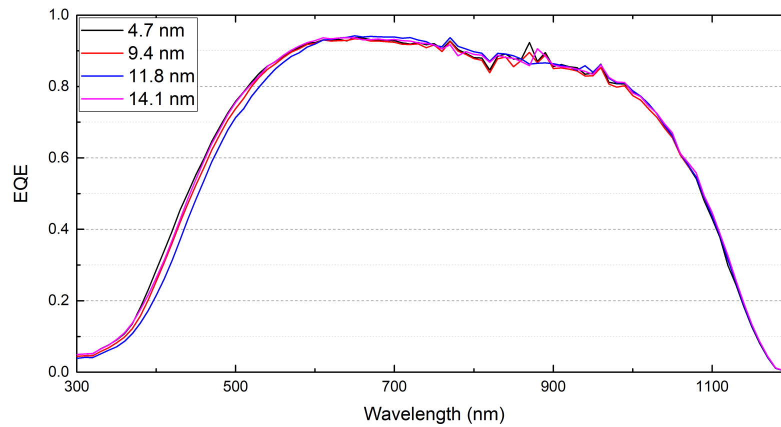

Figure 5.4: The external quantum efficiency of SHJ cells with the smooth pyramid texture for different a-Si:H passivation layer thicknesses. The p- and n-layer thicknesses were respectively 19 nm and 10 nm.

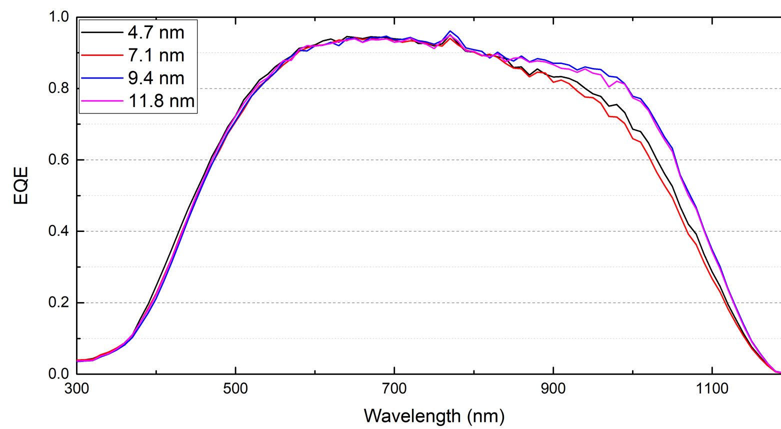

Figure 5.5: The external quantum efficiency of SHJ cells with the photolithography texture for different a-Si:H passivation layer thicknesses. The p- and n-layer thicknesses were respectively 19 nm and 10 nm.

5.3. P-layer thickness

In this section an optimization of the p-layer thickness in single-junction SHJ cells is described. Since only limited time was available and the smooth pyramid texture gave the best results in the previous experiments, this was the only texture for which further experiments were performed. The external solar cell parameters of SHJ cells with a p-layer thickness in between 12.5 and 25.0 nm is presented in Figure 5.6. For this experiment, the a-Si:H passivation layer thickness was kept constant at 14 nm.

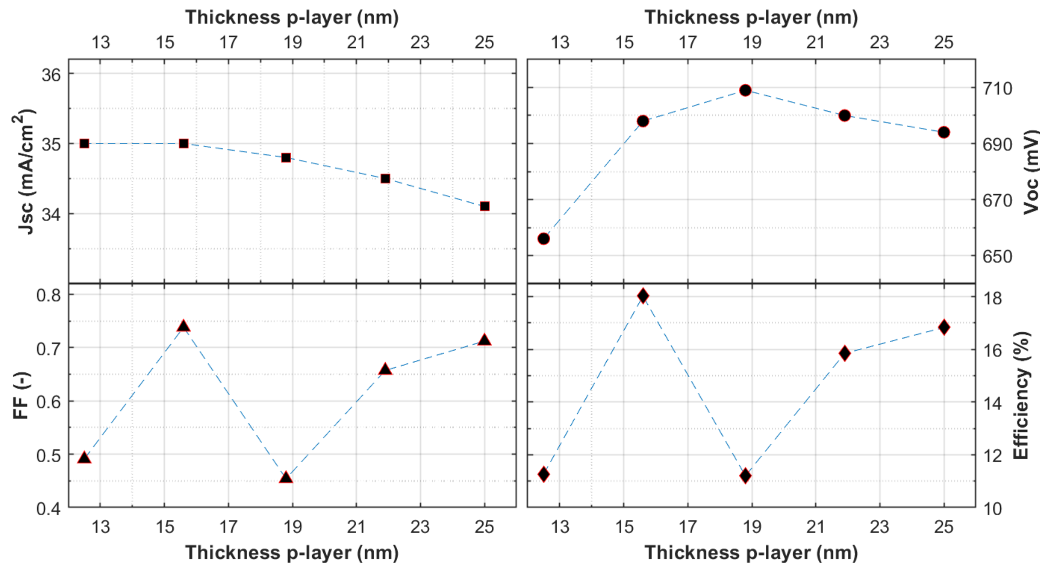

Figure 5.6: External solar cell parameters of SHJ cells with the smooth pyramid texture for different p-layer thicknesses. The i-a-Si:H passivation layer had a thickness of 9 nm on both sides, while the n-layer thicknesses was 10 nm.

In Figure 5.6, a decreasing trend in J_{sc} is observed for increasing p-thickness. This effect is caused by higher parasitic absorption of low-wavelength photons in thicker p-layers, which is illustrated in the EQE curves in Figure 5.7. Furthermore, the V_{oc} seems to be optimal for p-layer thicknesses in between 15 and 22 nm. This might be related to relatively low transport losses at the p/TCO interface for these thicknesses, as the crystallinity and opto-electrical properties of the doped p-layer are not uniform along the growth direction [58]. An alternative explanation for the decreasing V_{oc} for relatively thick p-layers could be that SRH recombination is enhanced if the p-layer becomes too thick. Even though a similar trend could be expected for the FF [56], this was not observed in this experiment. The fluctuating FF is assumed to be caused by sample-to-sample processing differences. Moreover, the influence of the n-layer thickness on the SHJ solar cell performance was investigated. Since this experiment gave inconclusive results, the external solar cell parameters are presented in Figure 4 in Appendix B.

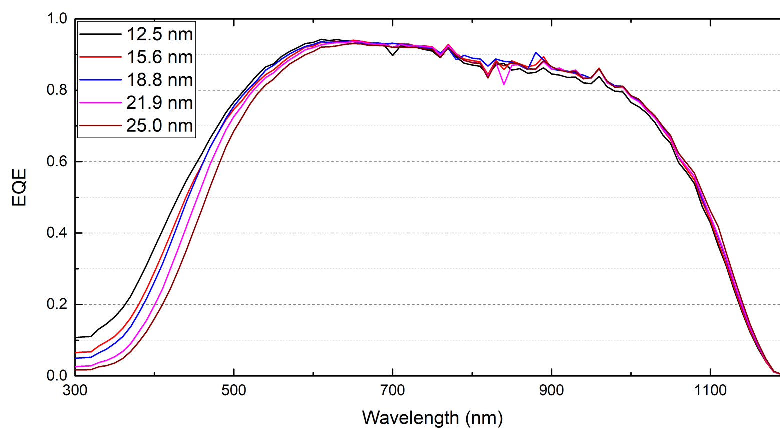

Figure 5.7: The external quantum efficiency of SHJ cells with the smooth pyramid texture for different p-layer thicknesses. The i-a-Si:H passivation layer had a thickness of 14 nm on both sides, while the n-layer thicknesses was 10 nm.

5.4. Conclusions

A comparison was made between the SHJ cell performance of wafers with the smooth pyramid surface texture, the photolithography surface texture, and the sacrificial layer surface texture. The smooth pyramid surface texture resulted in the best performing single-junction SHJ cells, which is assumed to be a result of this texturing approach leading to the smallest fraction of exposed <100> crystal orientations. Good surface passivation has been demonstrated for the smooth pyramid surface texture, indicated by a maximum achieved V_{oc} of 713 mV. The wafer surface of the photolithography texture proved to be more difficult to passivate, indicated by a maximum achieved V_{oc} of 660 mV. Proper passivation of the sacrificial layer surface texture requires further research.

The performance of the single-junction SHJ cell was shown to be extremely sensitive to the i-a-Si:H passivation layer. Firstly, it was shown that the passivation quality is highly dependent on the dilution of SiH_4 with H_2. For the used textures, the deposition through an undiluted SiH_4 plasma yielded the best results, which can be explained by the fact that these deposition conditions have the lowest probability to cause epitaxial growth. Secondly, the thickness of the i-a-Si:H passivation layer has a large impact on the cell performance. While thicker i-a-Si:H layers result in better surface passivation and a higher V_{oc}, this comes at the cost of FF. For example, increasing the i-a-Si:H layer thickness from 5 to 12 nm causes the FF to drop from 0.78 to 0.63, but increases the V_{oc} from 647 mV to 709 mV. Optimal SHJ single-junction cell efficiencies around 18% were achieved for an i-a-Si:H layer thickness between 5 and 12 nm. Furthermore, the p-layer thickness was shown to be optimal between 15 nm and 22 nm.

6 Optimizing the nanocrystalline silicon cell performance

In this chapter, an optimization of the nanocrystalline silicon (nc-Si:H) solar cell is treated. Since the aim of this thesis project is to incorporate this cell as a middle cell into a triple junction device, all nc-Si:H cells were processed on transparent back contacts without a back reflector. More specifically, they were deposited on textured corning glass covered with a 700 nm ZnO:Al layer. The step-by-step production method of these solar cells was presented earlier in section 3.3.2. In section 6.1 an optimization of the seed layer is treated. Subsequently, an optimization of the crystalline volume fraction of the intrinsic absorber layer and the intrinsic absorber layer thickness are respectively described in sections 6.2 and 6.3. Finally, the conclusions of this chapter are presented in section 6.4. The V_{oc} and FF values presented in this chapter were determined by taking the average value from J-V measurements of the 5 best cells of each sample. The J_{sc} values presented are the average values of EQE measurements of the 2 best cells.

6.1. Optimizing the seed layer

In this section, the influence of the seed layer on the nc-Si:H cell performance is treated. The seed layer is introduced in nc-Si:H cells to contribute to a uniform crystalline volume fraction throughout the intrinsic absorber layer. The crystalline fraction in an nc-Si:H layer is highly dependent on the substrate. For example, at certain deposition parameters, nc-Si:H layers directly grown on c-Si might result in epitaxial growth. However, if the same deposition parameters are applied while growing the layer directly on a non-crystalline surface such as glass, the first part of the layer might be amorphous while developing into a more crystalline phase. In an nc-Si:H cell it is desirable to have a uniform crystalline fraction along the intrinsic absorber layer. To this end, a highly crystalline seed layer is often deposited right before the deposition of the intrinsic absorber layer. This way, crystalline growth is promoted in the initial stage of the intrinsic layer, which results in a more uniform crystalline fraction throughout the intrinsic absorber layer [59].

The performance of nc-Si:H cells was investigated for two different types of seed layers. Both of these seed layers were deposited at a SiH_4 flow rate of 1.2 sccm, an H_2 flow rate of 120 sccm, and a pressure of 4 mbar. However, one type is deposited at 40 W and the other one at 50 W. For both of these seed layer types, thicknesses of 25 nm, 50 nm, and 100 nm were tried out. Before the seed layer investigation was performed, the p-layer of the nc-Si:H cell was optimized. the results of this optimization are presented in Appendix C.

The resulting external parameters of these nc-Si:H with different seed layers are presented in Table 6.1. It is shown that cell 3 has a relatively high V_{oc} of 762 mV, which indicates that this cell turned out amorphous. The used seed layer in this cell was exactly the same as those of cell 1 and 2, other than it being thicker. This illustrates just how sensitive the development of the crystalline fraction during nc-Si:H layer growth can be. An explanation of why this cell turned out amorphous will be given in the next section, as well as a measure to avoid this in the future. No significant trends are observed for the seed layer thickness variation in the other cells. However, the seed layers that are deposited at 40 W seem to give a slightly higher V_{oc} than that of 50 W. Hence, it was chosen to proceed with the 25 nm seed layer deposited at 40 W in future experiments.

Table 6.1: External solar cell parameters of nc-Si:H single-junction cells with a varying seed layer. Seed layer thicknesses of 25 nm, 50 nm and 100 nm were investigated at a deposition power of 40 W and 50 W.

Cell	Seed deposition power (W)	Seed thickness	J_{sc} (mA/cm^2)	V_{oc} (mV)	FF (-)	η (%)
1	40	25 nm	18.7	514	0.615	5.9
2	40	50 nm	19.5	510	0.615	6.1
3	40	100 nm	10.2	762	0.526	4.1
4	50	25 nm	19.1	504	0.617	5.9
5	50	50 nm	19.2	503	0.617	6.0
6	50	100 nm	19.3	499	0.621	6.0

6.2. Optimizing the intrinsic absorber layer

In this section an optimization of the intrinsic nc-Si:H absorber layer is treated. More specifically, the effect of the SiH_4/H_2 ratio and the power on the intrinsic layer are treated. The standard deposition parameters that were used for the intrinsic layer up to this experiment are presented in Table 6.2. The deposition times in this experiment were set in such a way that all intrinsic layers ended up having a thickness of 3 μm.

Table 6.2: Standard deposition parameters for the intrinsic layer of nc-Si:H cells.

SiH4 (sccm)	H2 (sccm)	Pressure (mbar)	Power (W)
3.5	120	4	40

The first experiment of this section concerns an optimization of the SiH_4/H_2 flow rate ratio for the intrinsic layer deposition. This was performed by varying the SiH_4 flow rate between 2.9 sccm (2.42% SiH_4) and 3.7 sccm (3.08% SiH_4) in steps of 0.2, all the while keeping the other deposition parameters in Table 6.2 fixed. The second experiment concerns an investigation of the optimal deposition power for the intrinsic layer deposition. This was performed by varying the power between 34 W (236.1 mW/cm^2) and 46 W (319.4 mW/cm^2) in steps of 3 W, all the while keeping the other deposition parameters in Table 6.2 fixed.

In Figure 6.1 and 6.2, Raman measurements of the intrinsic layers for both of the two experiments are presented. These measurements were performed on cells that were completely finished, which means part of the top surface was covered by square cell areas with TCO and an Aluminium front grid. However, the area in between these squares were large enough to perform Raman measurements on. It has to be noted that the Raman measurements were thus not directly performed on the intrinsic layer, but that a 12 nm p-layer was deposited on top of this. Nevertheless, the laser of the Raman still penetrates deep enough into the intrinsic layer to give a proper representation of its crystallinity. Figure 6.1 presents the relative Raman intensity for a varying SiH_4 flow, while Figure 6.2 presents this for various deposition powers.

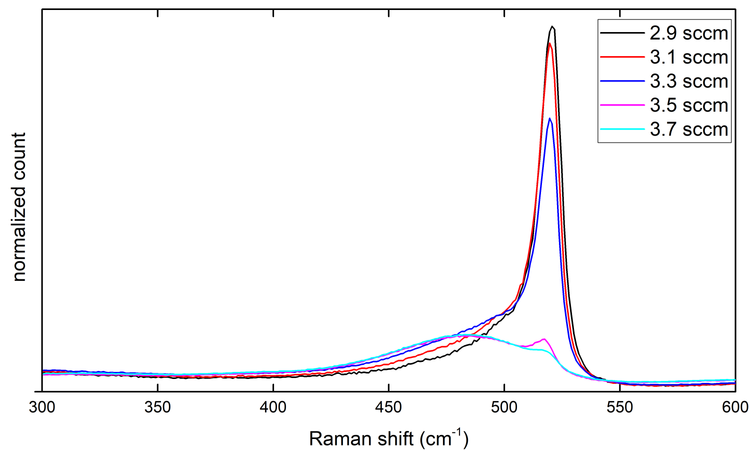

Figure 6.1: Raman spectra of nc-Si:H intrinsic layers for varying SiH_4 flow (2.9-3.7sccm) at a deposition power of 40 W. The measurements were performed at a laser excitation energy of 633 nm and the spectra are normalized with respect to the total amount of counts in the measurement.

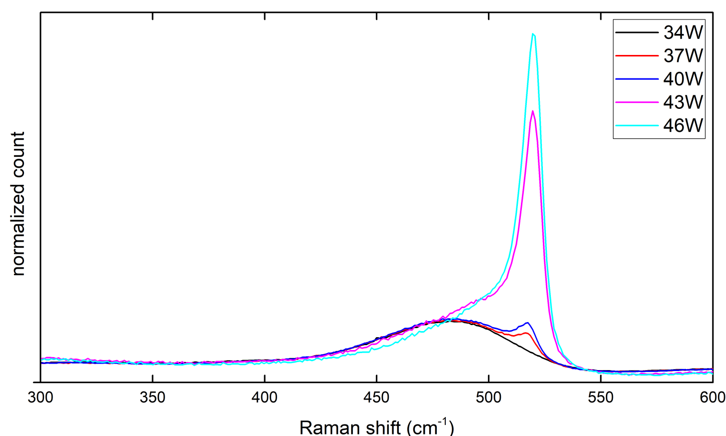

Figure 6.2: Raman spectra measured of nc-Si:H intrinsic layers for varying power (34 W to 46 W) at a SiH_4 flow of 3.5 sccm. The measurements were performed at a laser excitation energy of 633 nm and the spectra are normalized with respect to the total amount of counts in the measurement.

By making use of a Raman measurement, the corresponding crystalline fraction of the sample can be calculated. In this thesis, these calculations were performed with a peak-fitting approach that was initially developed by Smit et al. [60], which is described in Appendix D. The crystallinity of the different samples was calculated for both the red and the green laser Raman measurements. The resulting crystalline fractions of for the different intrinsic layers that were deposited are presented in Figure 6.3.

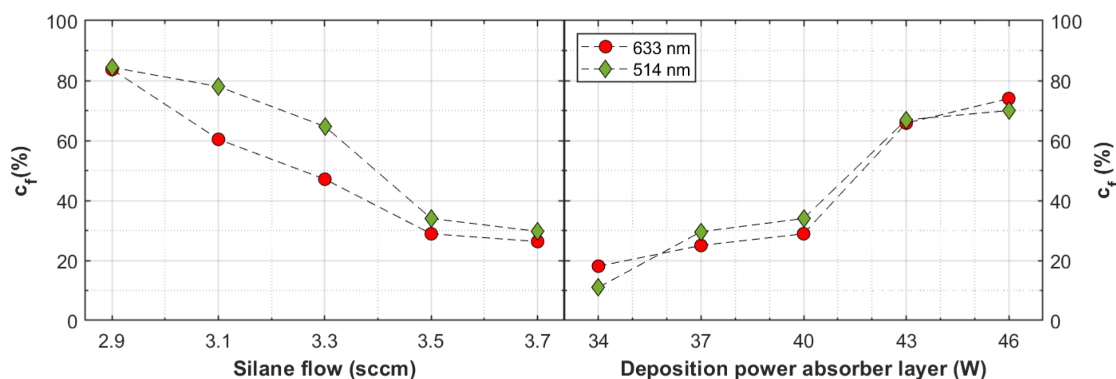

Figure 6.3: The crystalline fraction of the different intrinsic absorber layers. The fits to calculate the crystalline fraction were performed for Raman measurements with an excitation energy of both 633nm and 514 nm.

As can be seen in Figure 6.3, both the SiH_4/H_2 ratio and the power affect the crystalline fraction of the intrinsic layer. Firstly, the experiment shows that an increase of the relative flow rate of SiH_4 results in an nc-Si:H layer with a lower crystalline fraction. This is a well known effect caused by the fact that H_2 etches the disordered phase and eliminates unfavourable configurations like weak or strained Si-Si bonds [61]. Secondly, Figure 6.3 shows that an increasing power results in an nc-Si:H layer with a higher crystalline fraction. This can be explained by the fact that a higher power causes the electron temperature to increase, which promotes the depletion of the gas phase precursors and results in an increased H_2 flux to the substrate [62].

For both the relative silane flow and the power, it seems that the amorphous to nanocrystalline phase does not transform gradually, but that there is some sort of tipping point where a layer is either grown amorphous or nanocrystalline. In Figure 6.1 and 6.3 it is shown that this tipping point is exceeded if the SiH_4 flow rate is increased from 3.3 sccm to 3.5 sccm. In Figure 6.2 and 6.3 it is shown that the same thing happens if the power is decreased from 43 W to 40 W. Hence, it can be concluded that the standard deposition parameters for the intrinsic layer, earlier presented in Table 6.2, are close to the tipping point. This explains why only cell 3 of Table 6.1 was amorphous; the growth conditions of these nc-Si:H intrinsic layers were so close to the tipping point that the layers can be grown nanocrystalline one time, and amorphous the next time at the same deposition parameters. The effect of the intrinsic layer growth conditions on the external solar cell parameters is presented in Figure 6.4.

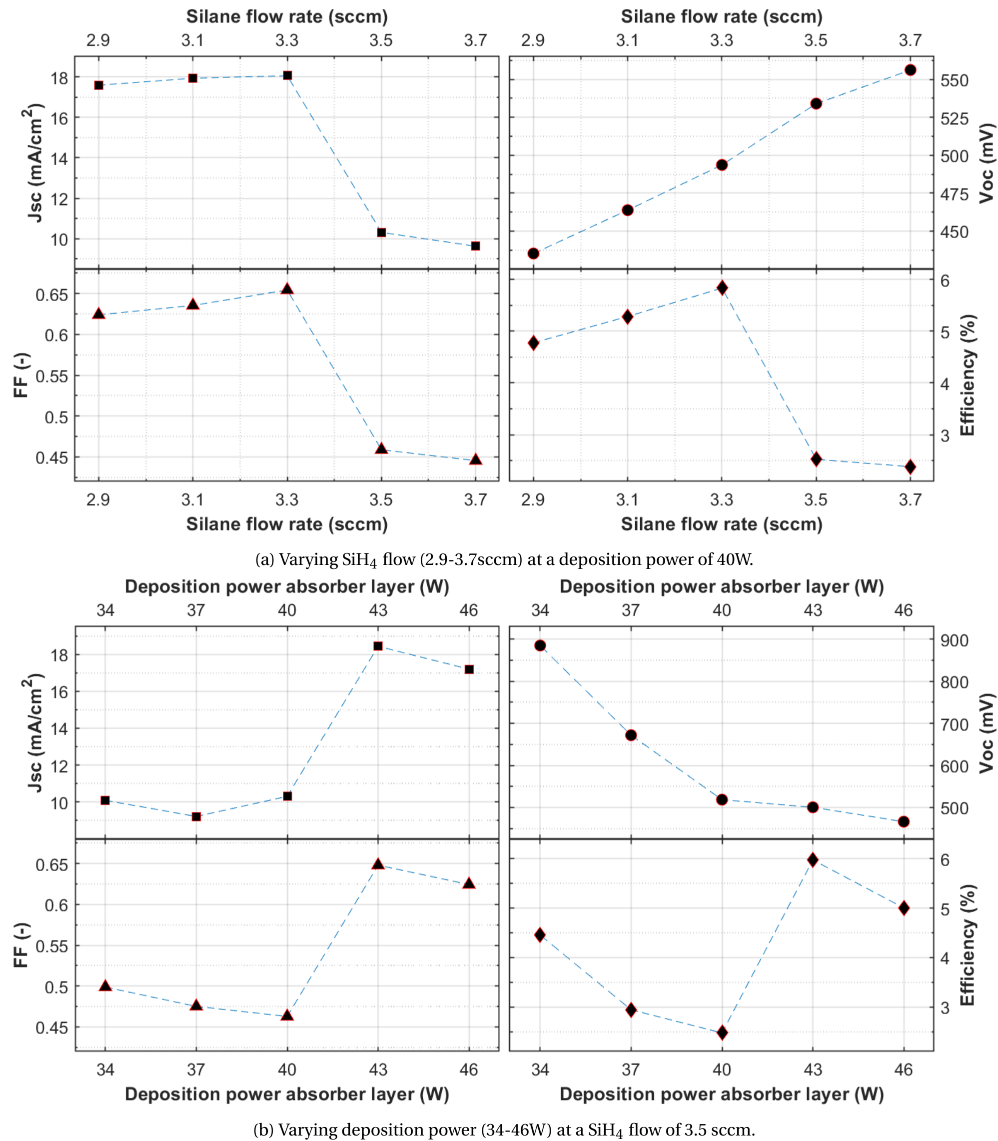

(a) Varying SiH_4 flow (2.9-3.7sccm) at a deposition power of 40W.

(b) Varying deposition power (34-46W) at a SiH_4 flow of 3.5 sccm.

Figure 6.4: External solar cell parameters of nc-Si:H cells for varying SiH_4 flow and power during the intrinsic layer deposition.

Figure 6.4 shows that the SiH_4/H_2 ratio and the deposition power during the intrinsic layer deposition are important factors influencing the nc-Si:H cell performance. This is mostly assumed to be due to the changing crystalline fraction. The effect of the previously described nanocrystalline-amorphous tipping point can clearly be seen in the J_{sc}, which drops severely as the cell becomes too amorphous. This effect can be investigated more closely by looking at the EQE curves in Figure 6.5. Here, it can be seen that the EQE of the highly amorphous cells is affected mostly in the low wavelength (300 nm - 500 nm) and the high wavelength range (700 nm - 1000 nm). A possible explanation for this is that the highly energetic photons which are being absorbed close to the p-i interface, create electron-hole pairs of which the electrons have to drift a relatively long way to reach the n-layer. In a layer with a higher crystalline fraction, the probability of this electron reaching the n-layer is higher than in a layer that is too amorphous, which can be explained by the fact that the c-Si phase has a higher electron mobility than the amorphous phase [63]. The reverse effect occurs in the high wavelength region, since these electron-hole pairs are on average generated closer to the i-n interface of the absorber layer due to a lower probability of the photons being absorbed. Furthermore, another factor at play is that the layers with a low crystalline phase have a lower absorption coefficient in the high wavelength region due to a higher band gap of the amorphous phase [64].

Similar to the J_{sc}, a severe drop in FF is observed if the nc-Si:H absorber layer becomes too amorphous. For amorphous silicon cells with a thickness of a few 100 nm, a high FF can be achieved. However, for the 3 μm absorber layer deposited here, the FF drops due to degraded transport properties [65], which result

in higher parasitic resistive losses. Unlike the J_{sc} and FF, the V_{oc} shows an increasing trend as the absorber layer gets more amorphous. This can be explained by the fact that the band gap of nc-Si:H increases as the crystallinity decreases [66].

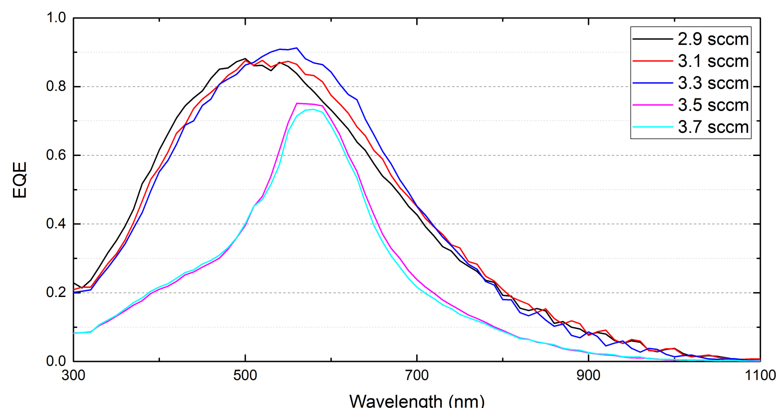

(a) EQE of nc-Si:H cells with varying SiH_4 flow (2.9-3.7sccm) at a deposition power of 40W.

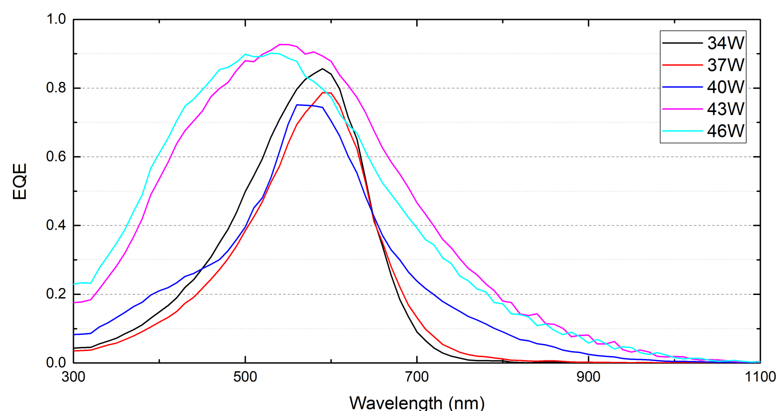

(b) EQE of nc-Si:H cells with varying deposition power (34-46W) at a SiH_4 flow of 3.5 sccm.

Figure 6.5: EQE for nc-Si:H cells with varying SiH_4 flow rate and power during the deposition of the intrinsic layer.

Based on these experiments, an additional experiment was performed in which the goal was to find the optimum deposition conditions for the intrinsic layer more precisely. The intrinsic layers that were tried, as well as the resulting external solar cell parameters are presented in Table 6.3.

Table 6.3: The left two columns present the SiH_4 flow rate and the power during the intrinsic layer deposition. The right four columns present the external solar cell parameters of the resulting cells.

Power (W)	SiH_4 (sccm)	Jsc (mA/m^2)	V_{oc} (mV)	FF (-)	η (%)
40	3.3	18.8	510	0.640	6.1
40	3.4	18.8	499	0.623	5.9
40	3.5	17.8	506	0.616	5.5
43	3.3	18.8	476	0.610	5.5
43	3.4	18.7	478	0.614	5.5
43	3.5	19.1	483	0.609	5.6

It is worth noting that for this experiment the absorber layer does not grow amorphous at a power of 40 W and a SiH_4 flow of 3.5 sccm, while this did happen in the previous experiment in this section. Based on the results presented in this section, a SiH_4 flow rate of 3.3 sccm and a power of 40 W were chosen to proceed with for the intrinsic layer of future nc-Si:H cells. These deposition parameters were shown to result in the best cells and are also less likely to result in amorphous growth than the previously used SiH_4 flow rate of 3.5 sccm.

6.3. Optimizing the intrinsic absorber layer thickness

In this section the influence of the absorber layer thickness on the nc-Si:H cell performance is treated. The optimal seed and intrinsic layer deposition parameters that were found in respectively section 6.1 and 6.2 were used for this thickness series. The thickness of the intrinsic layer was varied in between 2.0 μm and 5 μm in steps of 0.5 μm. These relatively thick nc-Si:H absorber layers were tried out because an nc-Si:H middle cell with an absorber layer thickness of 3.5 μm was current limiting in the triple-junction device of Perez-Rodriguez et al. [15]. Hence, it is interesting to see to what extent the external parameters are affected if the intrinsic layer thickness exceeds 3.5 μm. The resulting external solar cell parameters for this experiment are presented in Figure 6.6.

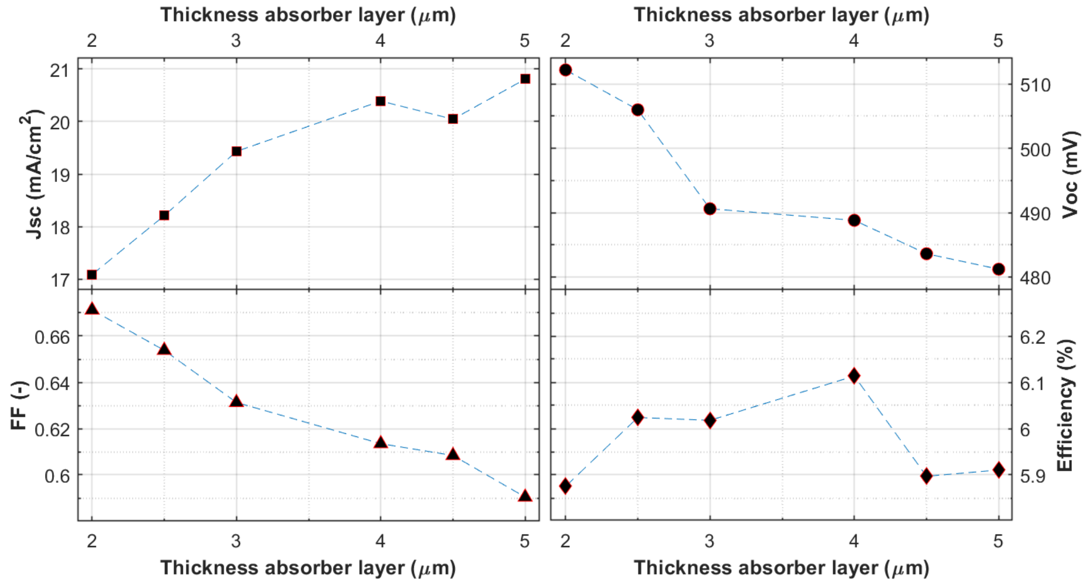

Figure 6.6: External parameters of nc-Si:H single-junction cells with different thicknesses of the intrinsic absorber layer.

In Figure 6.6, it is observed that the J_{sc} increases as the nc-Si:H absorber layer becomes thicker. In the EQE graph in Figure 6.7, it can clearly be seen that the increasing J_{sc} is caused by higher absorption in the infrared wavelength region, where photons are less likely to be absorbed. The transmission measurements in Appendix E indeed confirm that less photons in the wavelength region above 600 nm are transmitted as the absorber layer thickness increases. On the other hand, in Figure 6.6, the V_{oc} and FF show a decreasing trend for a higher absorber layer thickness. These decreasing trends are caused by a lower shunt resistance for thicker absorber layers, as presented in Appendix E. The fact that nc-Si:H absorber layers with a higher thickness have lower R_{sh} values and a higher J_0 is a trend that has been reported in previous work [65]. The efficiency was shown to be optimal for an absorber layer thickness between 3 μm and 4 μm.

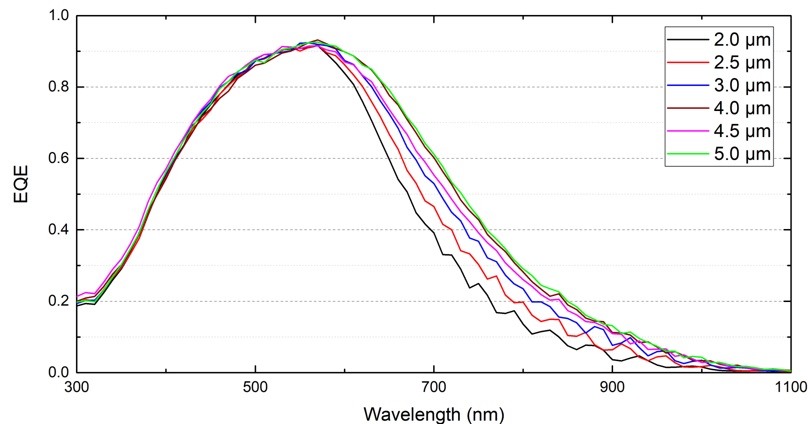

Figure 6.7: The external quantum efficiency of nc-Si:H single-junction cells with different thicknesses of the intrinsic absorber layer.

6.4. Conclusions

It was shown that the nanocrystalline solar cell performance is highly sensitive to the crystalline volume fraction of the intrinsic absorber layer. The crystalline fraction of the intrinsic layer was influenced by varying the SiH_4/H_2 flow rate ratio and the deposition power. The cell performance was found to be optimal at a crystalline volume fraction between 50% and 65%, which means that the deposition parameters are most favourable near the transition to amorphous growth. However, amorphous growth in the absorber layer should be avoided, because this is detrimental to the J_{sc} and FF of the solar cell. This makes processing nc-Si:H cells a challenging process, because the transition between the nanocrystalline and the amorphous phase is rather abrupt. The variation in the seed layers that were tried had little impact on the cell performance.

Furthermore, it was shown that choosing the absorber layer thickness of the nc-Si:H cell is a trade off between on the one hand J_{sc}, and on the other hand V_{oc} and FF. Doubling the absorber layer thickness from 2.5 μm to 5.0 μm results in a J_{sc} increase from 18.2 mA/cm^2 to 20.8 mA/cm^2, whereas the V_{oc} and the FF respectively decrease from 506 mV and 0.65 to 481 mV and 0.59.

7

Optimizing the tunnel recombination junctions

In this chapter an optimization of the tunnel recombination junctions is discussed. The tunnel recombination junctions facilitate recombination between opposite charge carriers from neighboring subcells. Since the final triple-junction device consists of three junctions, it will include two tunnel recombination junctions. In the two top junctions, from now on referred to as the top tandem, holes from the nc-Si:H middle cell should recombine with electrons from the a-Si:H top cell. In the bottom two junctions, from now on referred to as the bottom tandem, holes from the SHJ bottom cell should recombine with electrons from the nc-Si:H middle cell. In order to achieve a high V_{oc} and FF in a multi-junction, effective recombination of charge carriers in the TRJ is of the utmost importance. For that reason, different material combinations and thicknesses of p- and the n-layers are investigated.

The TRJ in the top tandem is optimized by processing micromorph tandem cells in nip-nip configuration on textured corning glass covered with a 700 nm ZnO:Al layer. The TRJ in the bottom tandem cell is investigated by processing SHJ/nc-Si:H tandem cells on wafers with a smooth pyramid texture. The optimized SHJ and nc-Si:H cells from respectively chapter 5 and 6 are hereby integrated into these multi-junction devices. A more thorough step-by-step description of the cell fabrication process was given in section 3.3.

In section 7.1, an optimization of the the p-layer in the TRJ of both the top and bottom tandem is treated. Subsequently, an optimization of the n-layer in the TRJ of the micromorph top tandem is described in section 7.2. The conclusions of this chapter are presented in section 7.3. The V_{oc} and FF values presented in this chapter were determined by taking the average value from J-V measurements of the 5 best cells of each sample. The J_{sc} values presented are the average values of EQE measurements of the 2 best cells.

7.1. Optimizing the p-layer of the tunnel recombination junction

In this section, an optimization of the p-layer of both the micromorph top tandem and the SHJ/nc-Si:H bottom tandem is described. The p-layer optimization of the micromorph top tandem is treated in section 7.1.1, while the results for the bottom tandem are presented in section 7.1.2. An interpretation of the observed results is described in section 7.1.3.

7.1.1. The p-layer in the micromorph top tandem

Six different p-layer material combinations have been investigated in the TRJ of the micromorph cell, all presented in Figure 7.1. For P1 to P3 the doping level in the top half of the p-layer is varied, while P4 to P6 all contain contact layers with a relatively low activation energy at the interface with the n-layer [58]. The exact deposition parameters of the different layers are presented in Table 4 of Appendix F. The micromorph cell consisted of a top cell with a 150 nm a-Si:H absorber layer, while the nc-Si:H absorber layer of the bottom cell was 3.5 μm thick.

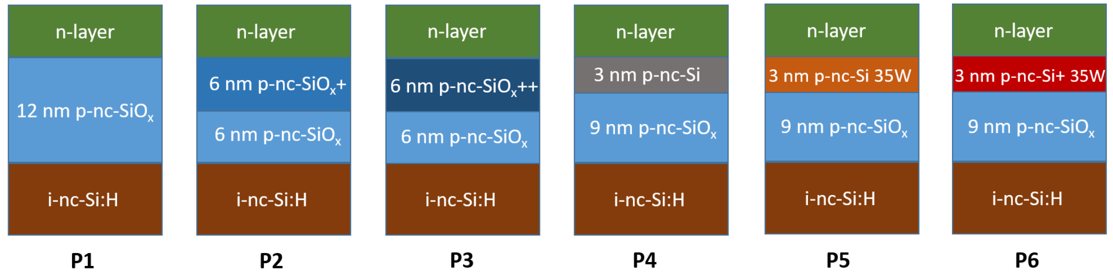

Figure 7.1: A schematic representation of the different p-layers that were tried in the TRJ of the micromorph top tandem. A plus-sign is indicative of a higher doping level. The exact deposition parameters of the different layers are presented in Table 4 of Appendix F. For the layers other than the contact layers of P5 and P6 a deposition power of 12 W was used.

The photovoltaic performance of the devices with the different p-layers of Figure 7.1 integrated in the TRJ are presented in Table 7.1. It is observed that p-nc-SiO_x contact layers (P1, P2 and P3) at the p/n interface have a superior optical and electrical performance compared to the other materials (P4, P5 and P6). The contact layers containing oxygen result in higher V_{oc} and FF values than the layers without oxide. Furthermore, an increasing trend in V_{oc} and FF is observed as the doping level of the top half of the p-layer is increased from P1 to P3. Finally, it is worth noting that the influence of the p-layer thickness on the micromorph cell was investigated. Since this experiment provided inconclusive results, these results are presented in Table 6 in Appendix G.

Table 7.1: External parameters of the different p-layers that were tried in micromorph cells. ΔV_{oc} indicates the loss in V_{oc} compared to the sum of the two single-junction cells.

TRJ	P1	P2	P3	P4	P5	P6
V_{oc} (mV)	1365	1365	1372	1375	1216	1358
ΔV_{oc} (mV)	-20	-20	-13	-10	-169	-27
FF (-)	0.722	0.734	0.743	0.716	0.532	0.739
J_{sc} top (mA/cm^2)	11.1	10.8	10.9	10.7	10.3	10.8
J_{sc} bottom (mA/cm^2)	7.5	7.5	7.9	7.4	7.4	7.4
J_{sc} sum (mA/cm^2)	18.6	18.3	18.7	18.1	17.8	18.2
Efficiency (%)	7.40	7.52	8.04	7.32	4.81	7.40

7.1.2. The p-layer in the SHJ/nc-Si:H bottom tandem

For the SHJ/nc-Si:H bottom tandem, similar p-layer material combinations have been investigated as for the micromorph tandem cells. However, the worst performing p-layer (P5 from Table 7.1) was replaced by the p-layer that was optimized for single-junction SHJ performance in chapter 5. The exact material combinations that were tried are presented in Figure 7.2, for all of which the exact deposition parameters are presented in Table 4 of Appendix F. The nc-Si:H cell had an absorber layer thickness of 2.7 μm.

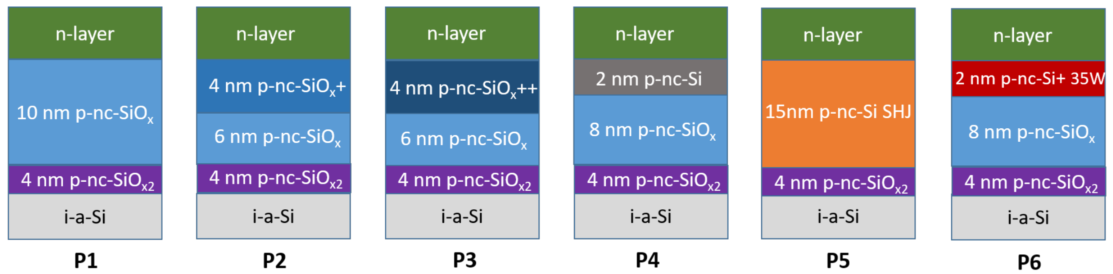

Figure 7.2: A schematic representation of the different p-layers that were tried in the TRJ of the SHJ/nc-Si bottom tandem. A plus-sign is indicative of a higher doping level. The exact deposition parameters of the different layers are presented in Table 4 of Appendix F.

The photovoltaic performance of the SHJ/nc-Si:H tandems with these different p-layer material combinations are presented in Table 7.2. It is observed that the V_{oc} and FF of the tandem increases as the doping level

of the top half of the p-layer is increased from P1 to P3. This is an interesting result, since the same trend was observed for the micromorph tandem cells. Hence, for both the SHJ/nc-Si:H bottom tandem and the micromorph top tandem, P3 was the best performing p-layer in the TRJ.

If the SHJ/nc-Si:H bottom tandem with P6 is compared to the same p-layer of the micromorph tandems, it is observed that the electrical performance of P6 gets close to the best performing p-layer (P3) for both tandems. The SHJ/nc-Si:H bottom tandem with P4 performed significantly worse than a micromorph cell with P4, which is related to a lower J_{sc} in the top cell and deteriorated electrical performance. Finally, the SHJ/nc-Si:H bottom tandem with P5 gets close to the performance of P3, but does not outperform it.

It is worth noting that the SHJ/nc-Si:H tandems made for this thesis significantly outperform previous record cells with this device structure, which had efficiencies of 9.68% [15] and 10.4% [67]. To the best of our knowledge, 14.65% is a world-record efficiency for a SHJ/nc-Si:H tandem cell.

Table 7.2: External parameters of the SHJ/nc-Si tandem cells with different p-layers. ΔV_{OC} indicates the loss in V_{OC} compared to the sum of the two single-junction cells.

TRJ	**P1**	**P2**	**P3**	**P4**	**P5**	**P6**
V_{oc} (mV)	1139	1140	1150	1015	1139	1146
ΔV_{oc} (mV)	-62	-61	-51	-186	-62	-55
FF (-)	0.596	0.688	0.690	0.640	0.700	0.681
J_{sc} top (mA/cm^2)	18.8	18.9	18.5	14.4	18.0	18.5
J_{sc} bottom (mA/cm^2)	18.7	18.5	18.9	19.1	18.5	18.6
J_{sc} sum (mA/cm^2)	37.6	37.4	37.3	33.5	36.6	37.1
Efficiency (%)	12.71	14.55	14.65	9.34	14.36	14.41

7.1.3. Discussion of the p-layer performance

Analyzing the performance of tandem cells with different tunnel recombination junctions can be a challenging process, because there are several factors at play. Firstly, the doped layers in a TRJ serve as the p-layer of the bottom cell and the n-layer of the top cell. Hence, these doped layers are responsible for the separation of charge carriers in the subcells. Secondly, the TRJ should facilitate the recombination between holes in the p-layer and electrons n-layer as efficiently as possible, hereby preventing the accumulation of charge carriers. A relatively high defect density at the p/n interface could therefore be beneficial, since SRH recombination is assumed to be dominant. However, this should not disproportionally reduce the conductivity, since the transverse conductivity in the doped layers should remain sufficient for the charge carriers to reach the p-n interface. As there are still more factors at play than just the ones described here, analyzing TRJ performance is a complicated process. Often, it is impossible to identify the exact cause of an observation with absolute certainty.

It was observed that p-nc-SiO_x material is the best performing p-type contact layer at the p/n interface, for which there are several explanations possible. Firstly, the presence of CO_2 in a SiH_4 plasma is known to suppress crystalline growth [58]. Therefore, the presence of CO_2 in the plasma can result in a more defective material at the p/n interface, hereby facilitating recombination more efficiently. Furthermore, the wide band gap due to the incorporation of oxygen might be beneficial to the carrier selective properties in the bottom junction due to improved band bending [68].

The other contact layers (P4-P6) that were tried were mainly chosen because of their relatively low activation energy [58]. A low activation energy in the p-layer is known to enhance charge carrier selectivity, mainly because it increases the energy barrier experienced by electrons, while it decreases the energy barrier for holes. Furthermore, it might increase the band bending at the interface with the intrinsic nc-Si:H absorber layer [68]. However, when these contact layers were applied in the p-layer of the micromorph TRJ (P4-P6), the V_{oc} and FF were outperformed by the p-nc-SiO_x contact layers. The same effect was observed for the SHJ/nc-Si:H bottom tandem, although to a lesser extent.

Furthermore, the the relative dopant gas flow rate in the top part of the p-nc-SiO_x layer was increased from P1 to P3, which enhanced both the V_{oc} and FF of the tandem cells. It is difficult to identify the exact cause of this effect, because doped SiO_x material growth is complex and increasing the relative dopant flow rate can affect it in a number of ways. Firstly, a higher active doping level in the p-layer is known to increase the built-in voltage of the bottom cell, hereby improving the bottom cell performance. Secondly, a higher doping level in the top part of the p-layer can suppress crystalline growth [58]. A more defect-rich p/n interface might facilitate recombination with the electrons of the neighbouring n-layer more efficiently than a more

crystalline layer with a lower defect density.

7.2. Optimizing the n-layer of the tunnel recombination junction

In this section an optimization of the n-layer in the TRJ of the micromorph top tandem is discussed. The micromorph tandem will be the integrated into the triple-junction device as the two top junctions. The results are presented in section 7.2.1, after which an interpretation of the observed results is treated in section 7.2.2. Another set of eight n-layers was processed for both the top and bottom tandem, but this set could not be included in this thesis report because the RF sputtering tool (ZORRO) was out of order.

7.2.1. Top tandem

Four investigated n-layer material combinations in the TRJ of the micromorph cell are presented in Figure 7.3. Since a highly doped SiO_x contact layer at the p/n interface worked well for the p-layer, this concept is also applied for N1-N3. For the contact layer of N4 no CO_2 was included in the SiH_4 plasma, which results in a higher crystallinity and a lower activation energy [58]. Furthermore, the performance of n-nc-SiO_x and n-a-Si:H in the main part of the n-layer can be compared between N1 and N2. The exact deposition parameters of the different layers are presented in Table 5 of Appendix F. The micromorph cell consisted of a top cell with a 175 nm a-Si:H absorber layer, while the nc-Si:H absorber layer of the bottom cell was 4.0 μm thick.

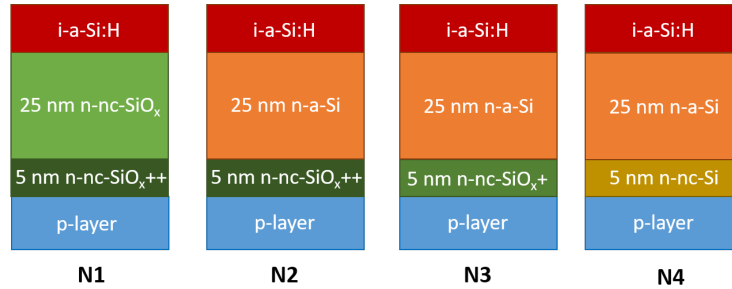

Figure 7.3: A schematic representation of the different n-layers that were tried in the TRJ of the micromorph top tandem. For all tandems, P3 from Figure 7.1 was incoroporated. A plus-sign is indicative of a higher doping level. The exact deposition parameters of the different layers are presented in Table 5 of Appendix F.

The photovoltaic performance of the micromorph tandems with these different n-layer material combinations are presented in Table 7.3. Here, it is observed that using n-nc-SiO_x in the main part of the n-layer stack (N1) results in better optical performance compared to n-a-Si:H (N2), indicated by a higher J_{sc} sum. Moreover, using n-nc-SiO_x in the main part of the n-layer (N1) seems to result in a higher V_{oc} than for using n-a-Si:H (N2), while the opposite is true for the FF. Furthermore, the n-nc-Si contact layer of N4 seems to offer better electrical performance than the highly doped n-nc-SiO_x contact layers of N2 and N3.

Table 7.3: External parameters of the different n-layers that were tried in micromorph cells. ΔV_{oc} indicates the loss in V_{oc} compared to the sum of the two single-junction cells.

TRJ	N1	N2	N3	N4
V_{oc} (mV)	1373	1365	1368	1371
ΔV_{oc} (mV)	-7	-15	-12	-9
FF (-)	0.685	0.695	0.706	0.714
J_{sc} top (mA/cm^2)	10.26	9.40	9.91	9.92
J_{sc} bottom (mA/cm^2)	8.98	8.55	7.97	7.91
J_{sc} sum (mA/cm^2)	19.25	17.95	17.88	17.84
Efficiency (%)	8.45	8.12	7.70	7.74

7.2.2. Discussion of the n-layer performance

It was observed that using n-nc-SiO_x instead of n-a-Si:H in the main part of the n-layer stack resulted in better optical performance of the tandem cell, indicated by a higher J_{sc} sum of the two subcells. This might be related to higher reflection into the top cell and lower parasitic absorption due to the high band gap of SiO_x.

Furthermore, the tandem cells with n-nc-SiO_x in the bulk of the n-layer had a higher V_{oc}. This might be related to the fact that n-a-Si:H has a higher activation energy, hereby implying a lower electron concentration and recombination rate. Moreover, n-a-Si:H has a smaller bandgap, which results in a lower barrier preventing holes from reaching the n-layer [69]. However, higher FF values were demonstrated for the n-layers where the main part of the n-stack consisted of n-a-Si:H material (P2, P3, P4). As presented in Table 9 in Appendix G, these higher fill factors are mainly caused by higher R_{sh} values. A possible explanation for this observation could be that n-a-Si:H layers result in a lower defect density at the interface with the a-Si:H intrinsic absorber layer.

The n-nc-Si:H layer (N4 of Figure 7.3) was the best performing contact layer at the p/n interface. This might be related to the fact that this contact layer has the the lowest activation energy [58]. The activation energy affects the band bending and the energy barrier experienced by holes from the neighbouring intrinsic layer [68]. Furthermore, the fraction of active dopants in this n-type contact layer might be higher due to its higher crystallinity.

7.3. Conclusions

In this chapter, the p- and the n-layer in the tunnel recombination junctions of both the SHJ/nc-Si:H bottom tandem and the micromorph top tandem were optimized. The optimized tunnel recombination junctions in this chapter resulted in a V_{oc} loss of 7 mV in the top tandem and 51 mV in the bottom tandem.

Firstly, it was shown that p-nc-SiO_x outperformed contact layers with a higher crystalline fraction and a lower activation energy at the p/n interface in both tunnel recombination junctions. The reason that p-nc-SiO_x performed best in the p-layer might be that its high band gap results in favourable carrier selective properties in the bottom cell. Furthermore, the electrical performance improved when the relative dopant gas flow in the plasma was increased in the top half of the p-layer. This might be related to suppressed crystalline growth and a more defect-rich p/n interface, hereby facilitating efficient charge carrier recombination in the TRJ.

For the n-layer, n-nc-Si outperformed highly doped n-nc-SiO_x as a 5 nm contact layer at the p/n interface. This might be related to its relatively high crystallinity and a low activation energy. Furthermore, tandem cells with n-nc-SiO_x in the main part of the n-layer yielded higher V_{oc} values than for n-a-Si:H, which might be related to the fact that n-nc-SiO_x has a higher band gap. Nevertheless, using n-a-Si:H at the n/i interface results in lower R_{sh} values and a higher FF, which could be caused by better passivation at the n/i interface of the neighbouring top cell.

8

The triple-junction device

In this chapter, the performance of the final triple-junction SHJ/nc-Si:H/a-Si:H device is discussed. For the fabrication of this device, the optimized work on SHJ single junction cells (chapter 5), nc-Si:H single junction cells (chapter 6) and tunnel recombination junctions (chapter 7) was combined. The eventual device structure is schematically represented in Figure 8.1. Hence, the optimized SHJ bottom cell was processed by passivating a smooth pyramid textured wafer with a 10 nm i-a-Si:H passivation layer on both sides. The n-side of the wafer was then covered by a 10 nm n-a-Si:H layer, a 150 nm ITO layer and a Ag/Cr/Al back contact. On the p-side of the wafer, a 16 nm p-nc-SiO_x layer was followed by the deposition of a micromorph cell in nip-nip configuration, a 75 nm ITO layer, and 500 nm thick aluminium front contacts. The nc-Si:H absorber layer of the middle cell had a thickness of 4 μm, while the a-Si:H absorber layer of the top cell was 160 nm thick. Furthermore, the p-layers in the tunnel recombination junctions of this device consisted of a p-nc-SiO_x layer with an increased doping level at the n-interface (P3 in Figure 7.1 and Figure 7.2). Likewise, the n-layers in the TRJs consisted of n-nc-SiO_x with an increased doping level at the p-interface (N1 in Figure 7.3). It is worth noting that these are not the most optimized n-layers from chapter 7, since this triple-junction device was processed before the full TRJ optimization was finished.

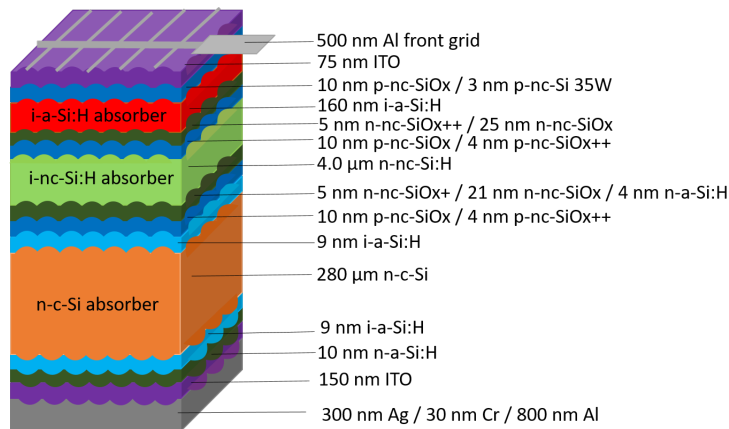

Figure 8.1: A schematic of the device structure of the triple-junction cell.

For the triple junction device described above, a PV efficiency of 13.63% was achieved, with a FF of 0.755, a V_{oc} of 1982 mV and a J_{sc} of 9.11 mA/cm^2. To the best of our knowledge, this is a world-record efficiency for this type of solar cell configuration. Our device outperforms the efficiency of similar device structures from Kirner et al. [20] and Perez-Rodriguez et al [15] by relatively 0.9% and 3.0%.

The external solar cell parameters of the single-junction cells, the bottom and top tandems, and the eventual triple junction device are all summarized in Table 8.1.

Table 8.1: External parameters of the different solar cells used in the different experiments. The single-junction external solar cell parameters are for an nc-Si:H middle cell absorber layer thicknesses of 4 μm and an a-Si:H top cell absorber layer thickness of 160 nm. However, it has to be noted that the reported bottom tandem had an nc-Si:H absorber layer thickness of 2.7 μm, hereby increasing the V_{oc} and decreasing the J_{sc} of the nc-Si:H subcell.

		V_{oc} (V)	J_{sc} Top (mA/cm^2)	J_{sc} Middle (mA/cm^2)	J_{sc} Bottom (mA/cm^2)	J_{sc} Total (mA/cm^2)	FF (-)	η (%)
Single junction	a-Si:H	0.89	11.3	-	-	-	0.64	6.5
	nc-Si:H	0.49	-	20.3	-	-	0.61	6.1
	SHJ	0.70	-	-	34.7	-	0.71	17.2
Top tandem		1.37	10.3	9.0	-	19.3	0.69	8.45
Bottom tandem		1.15	-	18.5	18.9	37.3	0.69	14.65
Triple junction		1.98	9.8	9.1	14.3	33.2	0.76	13.63

In Table 8.1, it can be seen that the V_{oc} of the triple-junction device is about 100 mV lower than the sum of the three indivual subcells. This is a higher voltage loss than the voltage losses occurring in the optimized TRJs, since 10 mV is lost in the TRJ of the top tandem, while this is 50 mV for the bottom tandem. This suggests that the V_{oc} of the triple-junction device could be boosted towards a value of 2.02 V in future research. Furthermore, it is observed that the triple-junction device has a relatively high FF of 0.76, which is assumed to be partly caused by the current mismatch between the bottom cell and the two top cells.

As presented in the JV characteristic in Figure 8.2, the maximum power point of the triple junction device operates at a V_{mpp} of 1.66 V and a J_{mpp} of 8.04 mA/cm^2. This maximum power point is estimated to closely match the operational point of a PEC device in which electrolysis is taking place [15].

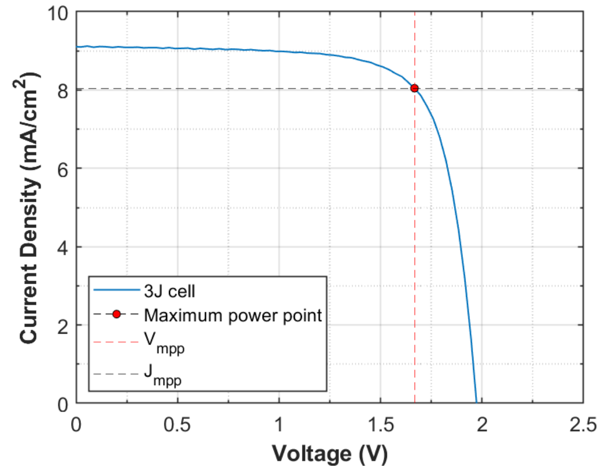

Figure 8.2: The JV characteristic of the triple-junction cell. The current density was corrected foro the J_{sc} that resulted from the EQE measurement of the nc-Si:H middle cell.

The EQE of the triple-junction is presented in Figure 8.3. Here, a dip is observed for the EQE sum between 700 nm and 1000 nm. The reason for this dip is that the TCO was slightly thinner than the intended 75 nm, resulting in increased light reflection in the 750-950 nm wavelength range due to interference effects taking place in the TCO.

Furthermore, it can be seen that the J_{sc} of the device is limited by the nc-Si:H middle cell. In order to achieve better current matching in the future, an intermediate reflective layer could be considered at the c-Si/nc-Si:H interface. However, the challenge would be to ensure that this IRL does not affect the electrical performance of the device to a significant extent. Since the spectral ranges of the different subcells overlap, light management and optimized absorber layer thicknesses are of the utmost importance for proper current matching. If it is managed in future research to match the current over the different subcells more evenly, a current density of 12 mA/cm^2 could be acheived for this device.

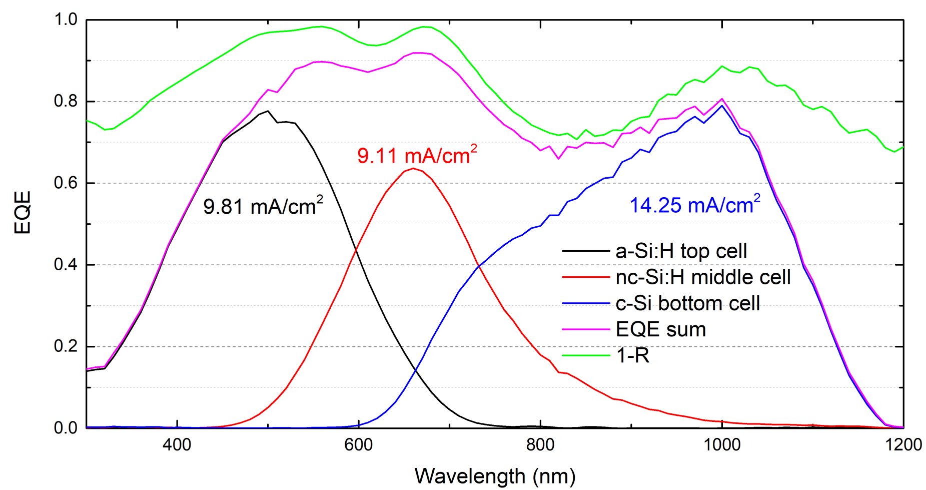

Figure 8.3: The external quantum efficiency of the triple-junction cell. The used absorber layer thicknesses for the a-Si:H and the nc-Si:H cells were respectively 160 nm and 4.0 μm.

9

Conclusions and recommendations

In this thesis work, a c-Si/nc-Si:H/a-Si:H triple-junction device has been developed and optimized. In this chapter the main findings from this thesis project are summarized in line with the research objectives that were defined in section 1.7. The main conclusions are presented in section 9.1, followed by recommendations regarding further research on these triple-junction devices in section 9.2.

9.1. Conclusions

The first research objective was to optimize the sacrificial layer texturing method. In this method, a sacrificial layer is anisotropically etched away due to the presence of crystalline grains. This process results in a texture of smooth crater like surface features on a c-Si wafer. Firstly, it was demonstrated that the crater size in the resulting surface texture increases if the argon ion implantation dose is increased from $1{\cdot}10^{16}$ ions/cm^2 to $2{\cdot}10^{16}$ ions/cm^2, presumably because larger grains are formed upon annealing if the ion concentration is higher. For higher implantation doses, the crater size seems to saturate. Secondly, it was demonstrated that the crater size in the resulting surface texture is sensitive to the thickness of the sacrificial layer. On the one hand, the crater size increases continuously for argon-implanted sacrificial layers as the thickness is increased from 250 nm to 1500 nm, presumably because larger crystalline grains can be formed in a sacrificial layer with a higher thickness. On the other hand, for thicknesses of 2000 nm or higher, the resulting crater size decreases. An explanation for this might be that an insufficient amount of ions ends up close to the c-Si interface for the used implantation energy. If relatively large grains are only formed in the top part of the sacrificial layer, the desired anisotropic etching effect fades out before the etchant reaches the c-Si interface. Hence, the crater size in the resulting surface texture is an interplay between the sacrificial layer thickness and the position where ions end up with respect to the c-Si interface. The sacrificial layer thickness was found to be optimal at 1500 nm, which resulted in a mean pore diameter crater increase from 385 nm to 456 nm compared to the previously used thickness of 1000 nm. Thirdly, varying the annealing temperature between 950 °C and 1050 °C did not significantly impact the resulting surface texture. Neither did varying the annealing time between 10 and 90 minutes. This suggests that all of these annealing steps provide the sacrificial layer with sufficient energy to fully crystallize. Fourthly, it was shown that the thickness of sacrificial layers implanted with BF_2 and As needs to remain relatively thin to achieve craters in the surface texture. Since BF_2 and As ions are heavier than Ar ions, they penetrate less deep into the sacrificial layer if the same implantation energy is used. As the implanter was already operating at its maximum implantation energy, relatively low sacrificial layer thicknesses had to be used in order to achieve sufficient ion concentration near the c-Si interface. These thinner sacrificial layers implanted with BF_2 and As resulted in smaller craters than were demonstrated for Ar-implanted sacrificial layers with a higher thickness.

The second objective of this thesis was to optimize the performance of the single junction silicon heterojunction (SHJ) solar cell. Since this cell will be integrated into the triple-junction device as the bottom cell, it needs to have a smooth surface texture to avoid cracks in the following nc-Si:H layer. To this end, three different proposed smooth surface textures were compared amongst each other. These surface texture were a smooth pyramid surface texture, a hexagonal surface texture created with photolithography, and the sacrificial layer texture. For all of these surface textures, a higher fraction of <100> crystal orientations is exposed

compared to the random pyramid texture that is regularly used in single-junction SHJ cells. The probability of undesired epitaxial growth in the passivation layer is higher if a larger fraction of the surface consists of <100> crystal orientations. For this reason, depositing the i-a-Si:H passivation layer through an undiluted SiH_4 plasma yielded the best results for the smooth surface textures. Amongst the different smooth surface textures, single-junction SHJ cells with the smooth pyramid surface texuture resulted in the best performing cells. This is assumed to be a result of the smooth pyramid texturing approach leading to the smallest fraction of exposed <100> crystal orientations, which are more challenging to passivate. Furthermore, the performance of the single-junction SHJ cell was shown to be extremely sensitive to the i-a-Si:H passivation layer thickness. While thicker i-a-Si:H layers result in better surface passivation and a higher V_{oc}, this comes at the cost of FF. For example, increasing the i-a-Si:H layer thickness from 5 to 12 nm causes the FF to drop from 0.78 to 0.63, but increases the V_{oc} from 647 mV to 709 mV. Optimal SHJ single-junction cell efficiencies around 18% were achieved for an i-a-Si:H layer thickness between 5 and 12 nm. Finally, the p-layer thickness was shown to be optimal between 15 nm and 22 nm.

The third objective of this thesis was to optimize the absorber layer of nip substrate nanocrystalline silicon single junction solar cells deposited on a transparent ZnO:Al back contact on a glass substrate. This cell is integrated into the triple-junction device as the middle cell. Regarding this objective, it was shown that the nc-Si:H solar cell performance is highly sensitive to the crystalline volume fraction of the intrinsic absorber layer. By varying the crystallinity trough adjusting the SiH_4/H_2 flow rate ratio and the deposition power, it was found that the nc-Si:H cell performance was optimal at a crystalline volume fraction between 50% and 65%. Hence, the optimal deposition parameters are most favourable near the transition to amorphous growth, but actual amorphous growth is detrimental to the J_{sc} and FF of the solar cell. Since the transition between the nanocrystalline and the amorphous phase was shown to be rather abrupt, it is important to properly optimize of the processing conditions of the nc-Si:H absorber layer. Furthermore, it was found that choosing the absorber layer thickness of the nc-Si:H cell is a trade off between on the one hand J_{sc}, and on the other hand V_{oc} and FF. Doubling the absorber layer thickness from 2.5 μm to 5.0 μm results in a J_{sc} increase from 18.2 mA/cm^2 to 20.8 mA/cm^2, whereas the V_{oc} and the FF respectively decrease from 506 mV and 0.65 to 481 mV and 0.59.

The fourth objective was to optimize the two tunnel recombination junctions (TRJs) in the triple-junction device. The optimized tunnel recombination junctions in this chapter resulted in a V_{oc} loss of 7 mV in the top tandem and 51 mV in the bottom tandem. Several different material combinations were tried for the p-layer at the p/n interface in the tunnel recombination junction of both the top and bottom tandem. These materials were p-nc-SiO_x with varying doping level and more crystalline p-nc-Si layers with a lower activation energy. It was found that the best performing p-type material at the p/n interface was p-nc-SiO_x, presumably because its high band gap results in favourable carrier selective properties in the bottom cell. Furthermore, the electrical performance was improved by increasing the relative dopant gas flow in the plasma during deposition of the top half of the p-layer, presumably because the suppressed crystalline growth in the top part of the layer might result in a defect-rich p/n interface, hereby facilitating efficient charge carrier recombination in the TRJ. For the n-layer, an n-nc-Si contact layer outperformed a highly doped n-nc-SiO_x layer at the p/n interface. This might be related to its relatively high crystallinity and a low activation energy. Furthermore, tandem cells with n-nc-SiO_x in the main part of the n-layer yielded higher V_{oc} values than for n-a-Si:H, which might be related to the fact that n-nc-SiO_x has a higher band gap and a lower activation energy. Nevertheless, using n-a-Si:H at the n/i interface results in lower R_{sh} values and a higher FF, which could be caused by a lower defect density at the n/i interface of the neighbouring top cell.

By using the results from the optimizations that were described above, the main research objective could be fulfilled, which was to make a triple-junction device based on c-Si/nc-Si:H/a-Si:H. The final device had a PV efficiency of 13.63%, with a FF of 0.755, a V_{oc} of 1982 mV and a J_{sc} of 9.11 mA/cm^2. To the best of our knowledge, this is a world-record efficiency for this type of solar cell configuration. If it is managed in future research to match the current over the different subcells more evenly, this device has the potential to achieve a current density over 12 mA/cm^2.

9.2. Recommendations

In this section, recommendations for further research are presented. These options could not be explored within the duration of this thesis project due to the limited time available.

Firstly, the efficiency of the triple-junction device could be improved by achieving better current matching between the different subcells. In this thesis work, the current limiting subcell was the nc-Si:H middle cell, while there is an abundance of current in the c-Si bottom cell. In order to improve the current matching, light management techniques should be applied to shift current from the bottom cell to the middle cell. For example, succesful integration of an intermediate reflective layer (IRL) at the c-Si/nc-Si:H interface could significantly increase the J_{sc} of the device. However, the challenge would be to ensure that this IRL does not affect the electrical performance of the device to a significant extent.

Secondly, it would be valuable to perform transmission electron microscopy (TEM) measurements for the sacrificial layer method. With proper TEM images of the crystalline grains in the sacrificial layer, the proposed explanations for the observed results in the crater size could be confirmed or disproved.

Thirdly, it would be interesting to optimize the passivation of the photolithography and sacrificial layer textures, which proved to be more challenging than for the smooth pyramid surface texture. Furthermore, it could be investigated how the performance of wafers with these smooth surface textures perform when integrated in multi-junction solar cells.

Fourthly, it could be worth the effort to boost the V_{oc} of the triple-junction cell by increasing the V_{oc} of the single-junction a-Si:H top cell. This could for example be done by investigating a higher band gap absorber like a-SiO_x.

Finally, it would be interesting to see if screen printing of the front contacts could improve the triple-junction solar cell performance. This technique might decrease the losses at the TCO/Al interface compared to electron beam evaporation.

Appendix

A: Etching time optimization of the sacrificial layer texturing method

Ideally, the etching time should be long enough, so that the sacrificial layer consisting of poly-Si is completely removed. However, if the wafer is etched for too long, the surface texture will again start to smooth out. The SEM images of Figure 1, Figure 2 and Figure 3 suggest an etching rate around 160 nm/min.

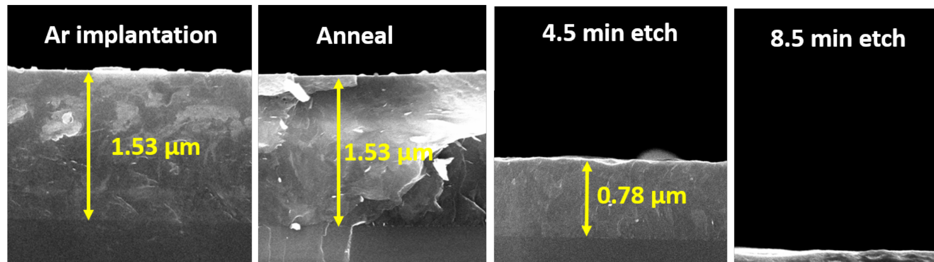

Figure 1: Cross-sectional SEM images of a 1500 nm sacrificial layer after after implantation with $1{\cdot}10^{16}$ ions/cm^2 Ar ions at 250 keV, after 1h annealing at 1050 °C, after 4.5 minutes of etching and after 8.5 minutes of etching. This figure suggests that the etchant has an etching rate around 160 nm/min.

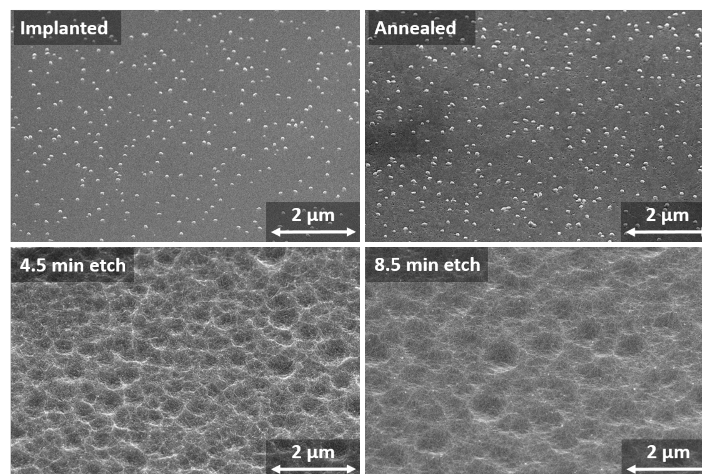

Figure 2: SEM images of the sacrificial layer after implantation with $1{\cdot}10^{16}$ ions/cm^2 Ar ions at 250 keV, after 1h annealing at 1050 °C, after 4.5 minutes of etching and after 8.5 minutes of etching.

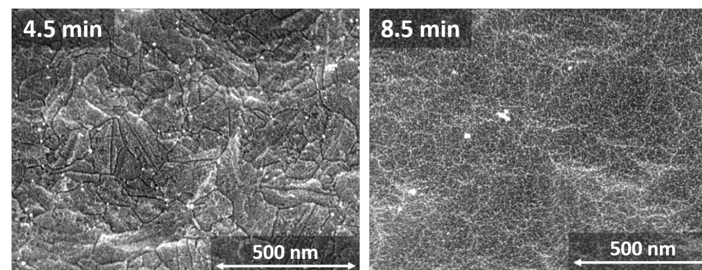

Figure 3: Highly zoomed in SEM images for the samples that were presented in Figure 2 with etching times of 4.5 minutes and 8.5 minutes. If the sacrificial layer is fully etched away, the microcracks in the SEM images seem to disappear.

B: Optimizing the n-layer thickness of the SHJ single-junction cell

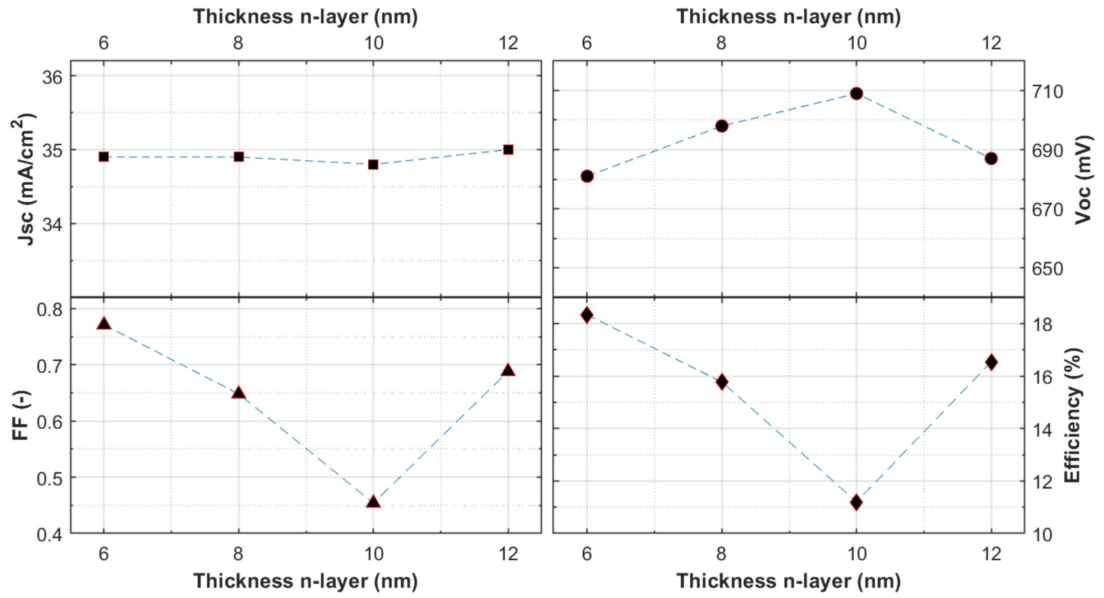

Figure 4: External solar cell parameters of SHJ cells with the smooth pyramid texture for different n-layer thicknesses. The i-a-Si:H passivation layer had a thickness of 14 nm on both sides, while the p-layer thicknesses was 19 nm.

C: Optimizing the p-layer of the nc-Si:H single-junction cell

Figure 5 presents four different p-layers that were tried for the nc-Si:H single-junction cell in this thesis. Furthermore, the exact deposition parameters of these different p-layers are presented in Table 1.

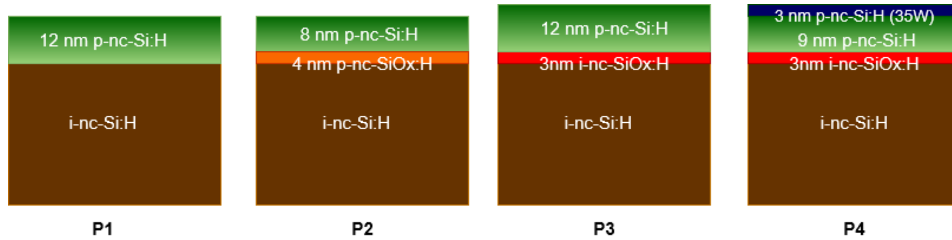

Figure 5: A schematic figure of the different p-layers that were tried, all labeled from P1 to P4.

Table 1: Deposition parameters for the different p-layers that were tried.

	SiH4 (sccm)	B2H6 (sccm)	Co2 (sccm)	H2 (sccm)	Pressure (mbar)	Power (W)
p-nc-Si:H	0.6	32	0	200	2.2	12
p-nc-SiOx:H	0.8	25	1.8	170	2.2	12
i-nc-SiOx:H	0.8	0	1.6	170	2.2	12
p-nc-Si:H 35W	0.8	20	0	170	2.2	35

As presented in Figure 5, two of the four cells (namely P3 and P4) include an i-nc-SiO_x:H layer at the p-i interface of the cell. Literature has shown interesting passivation and carrier selectivity properties of i-SiO_x layers. For example, including a p-nc-SiO_x layer at the p-i interface of a p-i-n deposited nc-Si:H cell has been shown to improve its performance. The main reason for this is assumed to be that this layer acts as an efficient barrier to boron cross-contamination [70]. Furthermore, ultrathin SiO_2 layers are used for surface passivation in c-Si solar cells in the TOPCon approach. Including a SiO_2 layer can increase the V_{oc} by a value of over 30 mV compared to a cell without this layer. Important reasons for this increase are assumed to be surface passivation and carrier selectivity [71].

The external solar cell parameters of the nc-Si:H cells with different p-layers are presented in Figure 6. If P2 is compared to P1, it can be seen that the current and the V_{oc} both increase if the bottom 4 nm of a regular 12 nm p-nc-Si:H is replaced by a p-nc-SiOx:H layer. However, this does not compensate for the severe FF decrease, which drops from 0.58 to 0.30.

In P3 a 3 nm i-nc-SiO_x layer was added at the p-i interface, which is not the case in the otherwise identical P1. This layer seems to improve the performance of the cell, as all external parameters of P3 are better than P1, resulting in an efficiency increase from 3.9% to 5.1%. The exact reasons for the increased performance are not fully understood, but it is assumed to be due to improved passivation and/or carrier selectivity. P4 is identical to P3, other than that the upper 3nm of p-nc-Si:H is processed at a much higher power, resulting in a highly crystalline layer with a low activation energy. This results in an increase of J_{sc}, namely from 16.2 to 18.1 mA/cm^2. As can be seen in the EQE curves in Figure 7, this is mainly caused by a significant increase in the 300 to 600 nm wavelength region. Hence, by adding this contact layer the efficiency is further increased from 5.1% to 5.5%. Concluding, P4 was the p-layer chosen to be used in further depositions.

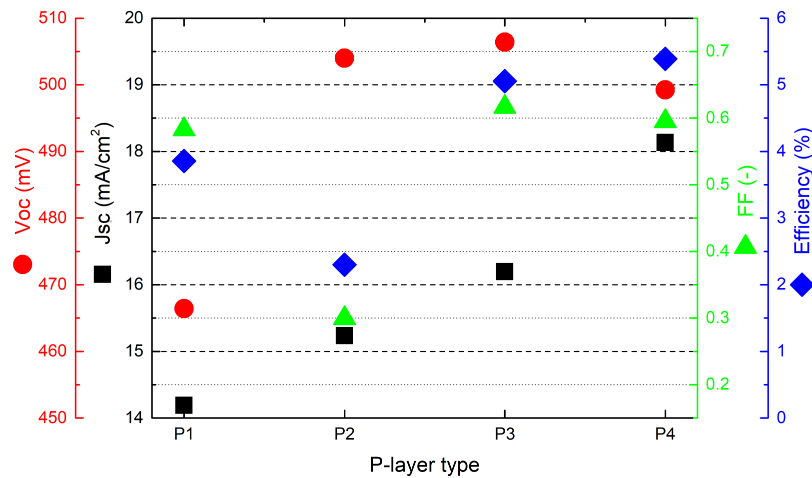

Figure 6: External solar cell paramaters for the different p-layers that are presented in Figure 5

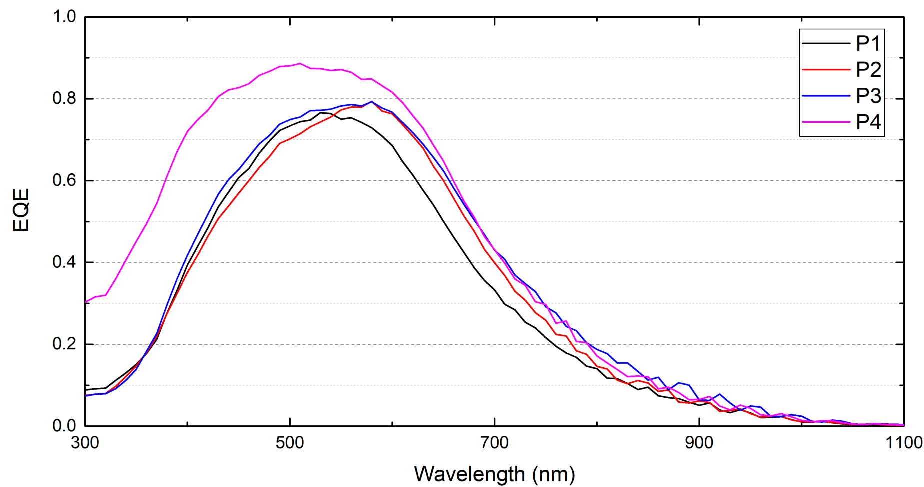

Figure 7: EQE for the different p-layers that are presented in Figure 5

D: Calculation method of the crystalline fraction

In a Raman spectrum of a nanocrystalline silicon layer, a rough estimation of the crystalline fraction can be made by analyzing the ratio between the crystalline peak at a Raman shift of 520 cm^{-1} and the amorphous peak at 480 cm^{-1}. However, a shortcoming of this method is that the Raman spectrum of a nanocrystalline film is not simply a summation of monocrystalline and amorphous silicon. The main reason for this that the Raman spectrum of a small crystalline grain differs from the Raman spectrum of monocrystalline silicon. This makes it a complex process to clearly determine which part of the Raman spectrum is caused by a contribution of the a-Si:H, and which part is caused by the crystalline grains. For example, the peak that is attributed to the amorphous fraction at 480 cm^{-1} shifts to higher energies with increasing crystalline fraction. This is not caused by a shift of the amorphous transverse optical (TO) phonon, but mainly by a change in the Raman peak shape of the crystalline fraction.

In order to overcome the previously described difficulty, Smit et al. have developed a method with which the crystalline fraction can be calculated more accurately [60]. Firstly, they showed that the Raman spectrum of the amorphous material in a nc-Si:H film can be represented fairly accurate by the individual Raman spectrum of a-Si:H. The reason for this is that the Raman spectra of amorphous silicon show no significant differences for different processing conditions in a relevant range. Subsequently, the contributions of the amorphous and the crystalline material is split by subtracting a scaled a-Si:H Raman spectrum from the nc-Si:H spectrum. The scaled a-Si:H Raman spectrum is obtained by fitting Gaussians to four characteristic phonon modes (TA, LA, LO and TO) of the amorphous spectrum. The contribution of the crystallites is then obtained by integrating the remaining nc-Si:H spectrum from 440 cm^{-1} to 560 cm^{-1}. Furthermore, the intermediate component peak is taken into account. This is the peak in between 494 and 507 cm^{-1} which is associated with bond dilation at grain boundaries [72].

The crystalline fraction X_C is then determined by using the following equation:

$$X_C = \left(\frac{A_{510} + A_{520}}{(0.8 * A_{480} + A_{510} + A_{520})} \right) \cdot 100\% \qquad (1)$$

In this equation, A_{510} corresponds to the gaussian fit of the intermedia component peak, A_{520} to the crystalline TO peak, and A_{480} to the amorphous TO peak. The factor of 0.8 is included because the count needs to be corrected for the difference in phonon excitation of c-Si compared to that of a-Si:H. Note that fixing this factor at 0.8 causes some uncertainty, since in reality this factor varies in between 0.7 and 0.9 depending on the size of the crystalline grains. For more information about determining the crystallinity of nc-Si:H films the reader is referred to the work of Smit et al. [60].

E: Extra data for single-junction nanocrystalline cells

Table 2: External solar cell parameters of nc-Si:H single-junction cells with varying deposition parameters for the intrinsic absorber layer.

Power (W)	SiH4 (sccm)	Jsc (mA/cm2)	Voc (mV)	FF (-)	eff (%)	Rs (Ohm*m2)	Rsh (Ohm*m2)
40	2.9	17.6	435	0.624	4.77	5.8	2171
40	3.1	17.9	464	0.635	5.28	6.5	2282
40	3.3	18.1	494	0.654	5.83	6.6	2932
40	3.5	10.3	534	0.459	2.53	14.1	943
40	3.7	9.6	556	0.445	2.38	16.7	883
34	3.5	10.1	885	0.499	4.45	65.1	1843
37	3.5	9.2	672	0.475	2.94	30.0	1300
43	3.5	18.4	500	0.648	5.98	8.1	3269
46	3.5	17.2	466	0.624	5.00	7.8	2103

Table 3: External solar cell parameters of nc-Si:H single-junction cells with different absorber layer thicknesses.

i-nc-Si:H absorber layer thickness (um)	Jsc (mA/cm2)	Voc (mV)	FF (-)	eff (%)	Rs (Ohm*m2)	Rsh (Ohm*m2)
2.0	17.1	512	0.671	5.88	7.7	5298
2.5	18.2	506	0.654	6.02	7.4	3478
3.0	19.4	491	0.631	6.02	7.7	3257
4.0	20.4	489	0.613	6.11	9.0	2768
4.5	20.0	484	0.608	5.90	8.1	2127
5.0	20.8	481	0.590	5.91	7.9	1972

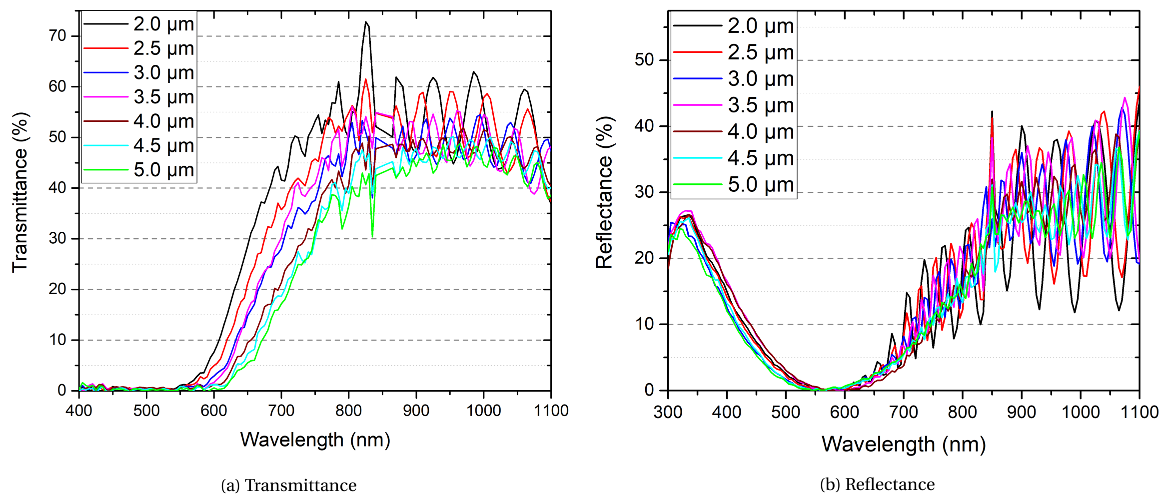

(a) Transmittance

(b) Reflectance

Figure 8: Transmittance and reflectance measurements of the nc-Si:H cells for the different thicknesses of the intrinsic layer. Note that the data of the transmittance figure is linearly interpolated in between 840 and 865 nm to prevent outliers due to detector switching of the LAMBDA machine.

F: Deposition parameters of the doped layers in the tunnel recombination junctions

Table 4: Deposition parameters of the different p-layers that were used in tunnel recombination junctions of the tandem cells.

	SiH4 (sccm)	B2H6 (sccm)	Co2 (sccm)	H2 (sccm)	Pressure (mbar)	Power (W)
p-nc-SiOx	0.8	10	2.2	170	2.2	12
p-nc-SiOx+	0.8	30	2.2	170	2.2	12
p-nc-SiOx++	0.8	50	2.2	170	2.2	12
p-nc-Si	0.6	32	0	200	2.2	12
p-nc-Si 35W	0.8	20	0	170	2.2	35
p-nc-Si+ 35W	0.8	40	0	170	2.2	35
p-nc-SiOx2	0.8	10	1.4	170	2.2	11
p-nc-Si SHJ	0.8	10	0	170	2.2	13

Table 5: Deposition parameters of the different n-layers that were used in tunnel recombination junctions of the tandem cells.

	SiH4 (sccm)	PH3 (sccm)	Co2 (sccm)	H2 (sccm)	Pressure (mbar)	Power (W)
n-nc-SiOx	1	2	1.6	120	1.5	11
n-nc-SiOx+	1	3	1.6	108	1.5	11
n-nc-SiOx++	1	3.6	1.6	108	1.5	11
n-nc-Si	1	2	0	120	1.5	11
n-a-Si	40	11	0	0	0.6	4

G: Extra data tunnel recombination junctions

Table 6: External parameters of micromorph cells with varying p-layer thickness. The p-layer materials of P3 from Figure 7.1 were used for these micromorph cell. For these micromorph cells, the nc-Si:H absorber layer of the bottom cell had a thickness of 4.0 μm.

Thickness p-layer (nm)	Voc (mV)	FF (-)	Jsc top (mA/cm2)	Jsc bottom (mA/cm2)	Jsc sum (mA/cm2)	eff (%)
10	1370	0.720	8.5	10.7	19.2	8.4
15	1380	0.713	8.4	9.5	18.0	8.3
20	1377	0.703	8.5	9.7	18.2	8.2

Table 7: Series and shunt resistances of the different micromorph top tandem p-layers from Figure 7.1.

TRJ	P1	P2	P3	P4	P5	P6
Voc (mV)	1365	1365	1372	1375	1216	1358
FF (-)	0.722	0.734	0.743	0.716	0.532	0.739
Rs (Ω·m^2)	45.5	27.3	25.1	32.9	2274.4	24.9
Rsh (Ω·m^2)	15707	13814	17015	13717	10049	15600

Table 8: Series and shunt resistances of the different bottom tandem p-layers from Figure 7.2.

TRJ	P1	P2	P3	P4	P5	P6
Voc (mV)	1139	1140	1150	1015	1139	1146
FF (-)	0.596	0.688	0.690	0.640	0.700	0.681
Rs (Ω·m^2)	16.1	7.4	8.0	4.9	12.4	9.2
Rsh (Ω·m^2)	16157	16898	19670	7050	14288	18465

Table 9: Series and shunt resistances of the different micromorph top tandem n-layers from Figure 7.3.

TRJ	N1	N2	N3	N4
Voc (mV)	1373	1365	1368	1371
FF (-)	0.685	0.695	0.706	0.714
Rs (Ω·m^2)	34.8	41.2	38.6	41.0
Rsh (Ω·m^2)	10999	13144	15647	15882

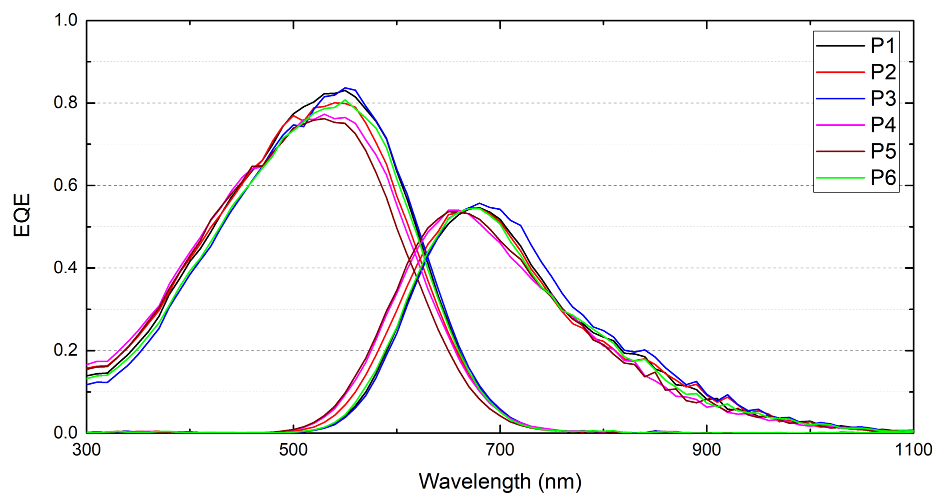

Figure 9: The external quantum efficiency of micromorph cells with the different p-layers from Figure 7.1.

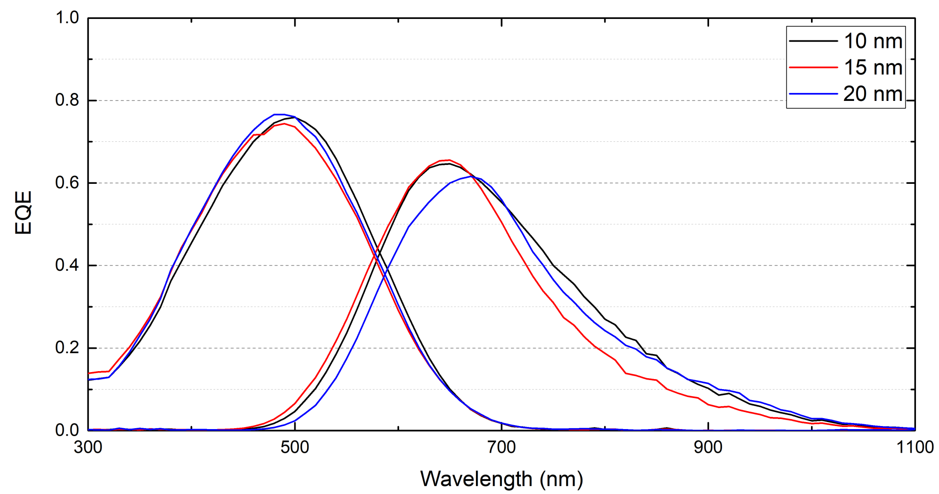

Figure 10: The external quantum efficiency of micromorph cells where P3 from Figure 7.1 was used and varied in thickness.

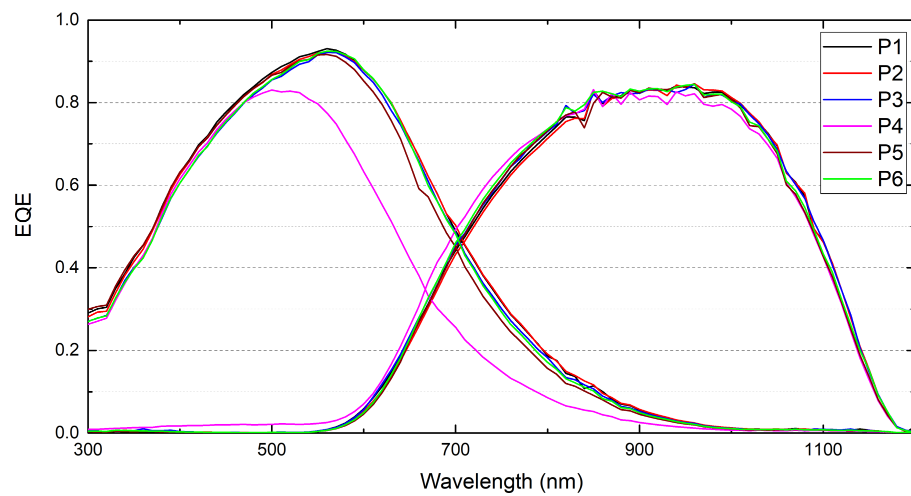

Figure 11: The external quantum efficiency of SHJ/nc-Si:H bottom tandem cells with the different p-layers from Figure 7.2.

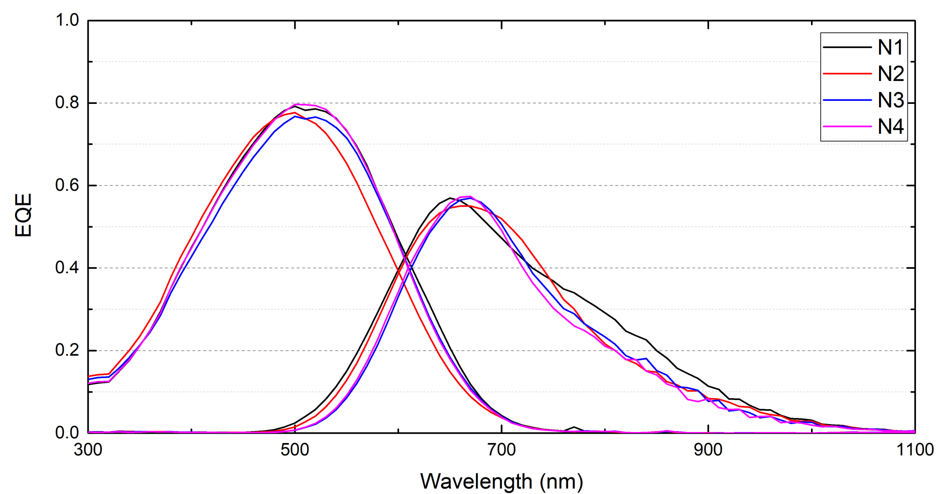

Figure 12: The external quantum efficiency of micromorph cells with the different n-layers from Figure 7.3.

Bibliography

[1] A.H.M. Smets, K. Jäger, O. Isabella, R.A.C.M.M. van Swaaij and M. Zeman, *Solar Energy.* Cambridge, UIT Cambridge Ltd, 2016.

[2] J. R. Petit, J. Jouzel, D. Raynaud, N. I. Barkov, J.M. Barnola, I. Basile, M. Bender, J. Chappellaz, M. Davis, G. Delaygue, M. Delmotte, V. M. Kotlyakov, M. Legrand, V. Y. Lipenkov, C. Lorius, L. PÉpin, C. Ritz, E. Saltzman and M. Stievenard, "Climate and atmospheric history of the past 420,000 years from the Vostok ice core, Antarctica," in *Nature,* Vol. 399, January 1999, pp. 429–436 [Online]. Available: Nature, https://www.nature.com/. [Accessed: Apr. 4 2020].

[3] C. MacFarling Meure, D. Etheridge, C. Trudinger, P. Steele, R. Langenfelds, T. van Ommen, A. Smith and J. Elkins, "Law Dome CO_2,CH_4 and N_2O ice core records extended to 2000 years BP," in *Geophysical research letters,* Vol. 33, Issue 14, February 2006, L14810 [Online]. Available: AGU, https://agupubs.onlinelibrary.wiley.com/. [Accessed: Apr. 4 2020].

[4] National Oceanic and Atmospheric Administration, Mauna Loa, 2020, "Trends in Atmospheric Carbon Dioxide," Available: NOAA Global Monitoring Laboratory, https://www.https://www.esrl.noaa.gov/gmd/ccgg/trends. [Accessed: Apr. 7 2020].

[5] O. Edenhofer, R. Pichs-Madruga, Y. Sokona, E. Farahani, S. Kadner, K. Seyboth, A. Adler, I. Baum, S. Brunner, P. Eickemeier, B. Kriemann, J. Savolainen, S. Schlömer, C. von Stechow, T. Zwickel and J.C. Minx, "Climate Change 2014: Mitigation of Climate Change.", Intergovernmental Panel on Climate Change, Contribution of Working Group III to the Fifth Assessment Report of the Intergovernmental Panel on Climate Change, 2014. [Online]. Available: https://www.ipcc.ch/. [Accessed: Feb. 20, 2020].

[6] G.R. Timilsina, L. Kurdgelashvili and P. Narbel, "Solar energy: Markets, economics and policies," in *Renewable and Sustainable Energy Reviews,* Vol. 16, Issue 1, January 2012, pp. 449-465 [Online]. Available: Science Direct, https://www.sciencedirect.com. [Accessed: Feb. 14 2020].

[7] E. Bellini, "Dubai confirms Saudi's ACWA won 900 MW solar project tender with $0.016953/kWh bid," PV Magazine, November 2019. [Online]. Available: https://www.pv-magazine.com/ [Accessed: Feb. 18, 2020].

[8] Fraunhofer Institute for Solar Energy Systems, "Levelized cost of electricity renewable energy technologies," Fraunhofer ISE, March 2018. [Online]. Available: https://www.ise.fraunhofer.de. [Accessed: Feb. 14, 2020].

[9] V. Fthenakis and H. C. Kim, "Land use and electricity generation: A life-cycle analysis," in *Renewable and Sustainable Energy Reviews,* Vol. 13, Issues 6–7, August 2009, pp. 1465-1474 [Online]. Available: Science Direct, https://www.sciencedirect.com. [Accessed: Feb. 14 2020].

[10] International Energy Agency, "Renewables 2018," IEA, 2018. [Online]. Available: https://www.iea.org/reports/renewables-2018. [Accessed: Feb. 14, 2020].

[11] O. Isabella, "PV systems (MSc course)," TU Delft, Delft, 2019.

[12] J. Kunze, O. Paschos, U. Stimming, "Fuel Cell Comparison to Alternate Technologies," In: Meyers R.A. (eds) Encyclopedia of Sustainability Science and Technology, Springer, New York, NY, 2012. [Online]. Available: https://link.springer.com. [Accessed: Feb. 14, 2020].

[13] A. Buttler and H. Spliethoff, "Current status of water electrolysis for energy storage, grid balancing and sector coupling via power-to-gas and power-to-liquids: A review," in *Renewable and Sustainable Energy Reviews,* Vol. 82, Part 3, February 2018, pp. 2440-2454 [Online]. Available: Science Direct, https://www.sciencedirect.com. [Accessed: Feb. 14 2020].

[14] L. Schlapbach and A. Züttel, "Hydrogen-storage materials for mobile applications," in *Nature,* Vol. 414, November 2001, pp. 353-358 [Online]. Available: Nature, https://www.nature.com. [Accessed: Feb. 18 2020].

[15] P. Perez-Rodriguez, W. Vijselaa, J. Huskens, M. Stam, M. Falkenberg, M. Zeman, W. Smith and A.H.M. Smets, "Designing a hybrid thin-film/wafer silicon triple photovoltaic junction for solar water splitting," in *Progress in Photovoltaics,* Vol. 27, Issue 3, March 2019, pp. 245-254 [Online]. Available: Wiley Online Library, https://onlinelibrary.wiley.com/. [Accessed: Feb. 14 2020].

[16] W.H. Cheng, M.H. Richter, M.M. May, J. Ohlmann, D. Lackner, F. Dimroth, T. Hannappel, H.A. Atwater and H. Lewerenz. "Monolithic Photoelectrochemical Device for Direct Water Splitting with 19% Efficiency," in *ACS Energy Lett.,* Vol. 3.8, June 2018, pp. 1795-1800 [Online]. Available: ACS Publications, https://pubs.acs.org/. [Accessed: Feb. 20 2020].

[17] J.W. Schüttauf, M.A. Modestino, E. Chinello, D. Lambelet, A. Delfino, D. Dominé, A. Faes, M. Despeisse, J. Bailat, D. Psaltis, C. Moser and C. Ballif, "Solar-to-Hydrogen Production at 14.2% Efficiency with Silicon Photovoltaics and Earth-Abundant Electrocatalysts," in *Journal of The Electrochemical Society,* Vol. 163 (10) F1177-F1181, August 2016. [Online]. Available: ResearchGate, https://www.researchgate.net/. [Accessed: Feb. 20 2020].

[18] W.J. Chang, K. Lee, H. Ha, K. Jin, G. Kim, S. Hwang, H. Lee, S. Ahn, W. Yoon, H. Seo, J.S. Hong, Y.K. Go, J. Ha and K.T. Nam, "Design Principle and Loss Engineering for Photovoltaic-Electrolysis Cell System," in *ACS Omega,* Vol. 2.3, March 2017, pp. 1009-1018 [Online]. Available: ACS Publications, https://pubs.acs.org/. [Accessed: Feb. 20 2020].

[19] W.J.C. Vijselaar, P. Perez-Rodriguez, P.J. Westerik, R.M. Tiggelaar, A.H.M. Smets, H. Gardeniers and J. Huskens, "A Stand-Alone Si-Based Porous Photoelectrochemical Cell," in *Progress in Photovoltaics,* Vol. 9, Issue 19, May 2019, 1803548 [Online]. Available: Wiley Online Library, https://onlinelibrary.wiley.com/. [Accessed: Feb. 24 2020].

[20] S. Kirner, H. Sarajan, A. Azarpira, T. Schedel-Niedrig, B. Stannowski, B. Rech and R. Schlatmann, "Wafer Surface Tuning for a-Si:H/μc-Si:H/c-Si Triple Junction Solar Cells for Application in Water Splitting," in *Energy Procedia,* Vol. 102, December 2016, pp. 126-135 [Online]. Available: Science Direct, https://www.sciencedirect.com. [Accessed: Feb. 20 2020].

[21] T. de Vrijer and A.H.M Smets, "Advanced textured monocrystalline silicon substrates with high optical scattering yields and low electrical recombination losses for supporting crack-free nano-to polycrystalline film growth," in *Progress in Photovoltaics,* under review.

[22] M. Wiering, "New Methods of Texturing Crystalline Silicon," Master's thesis, Delft University of Technology, Delft, 2020.

[23] A. Richter, M. Hermle and S. Glunz, "Reassessment of the Limiting Efficiency for Crystalline Silicon Solar Cells ," in *IEEE Journal of Photovoltaics,* Vol. 3, no. 4, pp. 1184-1191, July 2013, [Online]. Available: ResearchGate, https://www.researchgate.net/. [Accessed: March 12 2020].

[24] S.A, Hadi, E.A. Fitzgerald and A. Nayfeh, "Theoretical efficiency limit for a two-terminal multi-junction "step-cell" using detailed balance method," in *Journal of Applied Physics,* Vol. 119, Issue 7, February 2016, p. 073104 [Online]. Available: American Institute of Physics, https://aip.scitation.org/journal/jap. [Accessed: Jan. 27 2020].

[25] D. McLaughlin, "Spectrum absorption," 2010. Available: https://www.appropedia.org

[26] P. Babal, "Doped nanocrystalline silicon oxide for use as (intermediate) reflecting layers in thin-film silicon solar cells," Ph.D. thesis, Delft University of Technology, Delft, 2014.

[27] G. Papakonstaniou, "Investigation and Optimization of the Front Metal Contact of Silicon Heterojunction Solar Cells," Master's thesis, Delft University of Technology, Delft, 2014.

[28] G. Limodio, "Strategies for the implementation of ion implantation doping technique in c-Si wafer-based solar cells," Ph.D. thesis, Delft University of Technology, Delft, 2019.

[29] L. Röntzsch, "Self-Organization of Nanocluster delta-Layers at Ion-Beam-Mixied Si-SiO_2 Interfaces," Ph.D. thesis, Forschungszentrum Rossendorf, Dresden, Oktober 2003.

[30] S.Y. Herasimenka, W.J. Dauksher and S.G. Bowden, ">750 mV open circuit voltage measured on 50 μm thick silicon heterojunction solar cell," in *Applied Physics Letters,* Vol. 103, Issue 5, July 2013, 053511 [Online]. Available: American Institute of Physics, https://aip.scitation.org/. [Accessed: May 31 2020]

[31] D. Deligiannis, "Surface passivation for silicon solar cells," Ph.D. thesis, Delft University of Technology, Delft, 2017.

[32] A.F.M. Leenaars, J.A.M. Huethorst, and J.J. Van Oekel, "Marangoni drying: A new extremely clean drying process," in *Langmuir,* Vol. 6, Issue 11, November 1990, pp. 1701-1703 [Online]. Available: ACS Publications, https://pubs.acs.org/. [Accessed: May 31 2020].

[33] M. Morita, T. Ohmi, E. Hasegawa, M. Kawakami, and M. Ohwada, "Growth of native oxide on a silicon surface," in *Journal of Applied Physics,* Vol. 68, Issue 3, March 1990, 1272 [Online]. Available: American Institute of Physics, https://aip.scitation.org/. [Accessed: May 31 2020]

[34] M. Mews, T.F. Schulze, N. Mingirulli and L. Korte, "Hydrogen plasma treatments for passivation of amorphous-crystalline silicon-heterojunctions on surfaces promoting epitaxy," in *Applied Physics Letters,* Vol. 102, Issue 12, March 2013, 122106 [Online]. Available: American Institute of Physics, https://aip.scitation.org/. [Accessed: May 31 2020]

[35] Y. Zhao, L. Mazzarella, P. Procel, C. Han, G. Yang, A. Weeber, M. Zeman, O. Isabella, "Doped hydrogenated nanocrystalline silicon oxide layers for high-efficiency c-Si heterojunction solar cells," in *Progress in Photovoltaics,* Vol. 28, Issue 5, February 2020, pp. 425-435 [Online]. Available: Wiley Online Library, https://onlinelibrary.wiley.com/. [Accessed: May 31 2020].

[36] G. Yang, R.A.C.M.M. van Swaaij, Olindo Isabella and Miro Zeman, "A novel way of texturing glass for microcrystalline silicon thin film solar cells application," in *Progress in Photovoltaics,* Vol. 23, Issue 10, October 2014, pp. 1283-1290 [Online]. Available: Wiley Online Library, https://onlinelibrary.wiley.com/. [Accessed: May 4 2020].

[37] Z. Iqbal and S. Veprek, "Raman scattering from hydrogenated microcrystalline and amorphous silicon," in *Journal of Physics C: Solid State Physics,* Vol. 15, Issue 2, 1982, pp. 377-392 [Online]. Available: ResearchGate, https://www.researchgate.net/. [Accessed: Mar. 29 2020].

[38] A. H. M. Smets, T. Matsui, and M. Kondo, "High-rate deposition of microcrystalline silicon p-i-n solar cells in the high pressure depletion regime," in *Journal of Applied Physics,* Vol. 104, Issue 3, May 2008, 034508 [Online]. Available: American Institute of Physics, https://aip.scitation.org/. [Accessed: Mar. 29 2020].

[39] R.A. Sinton and A. Cuevas, "Contactless determination of current–voltage characteristics and minority-carrier lifetimes in semiconductors from quasi-steady-state photoconductance data," in *Applied Physics letters,* Vol. 69, Issue 17, August 1996, 2510 [Online]. Available: American Institute of Physics, https://aip.scitation.org/. [Accessed: Mar. 30 2020].

[40] G. Yang, "High-efficient n-i-p thin-film silicon solar cells," Ph.D. thesis, Delft University of Technology, Delft, 2015.

[41] H. Sai, K. Saito, N. Hozuki, and M. Kondo, "Relationship between the cell thickness and the optimum period of textured back reflectors in thin-film microcrystalline silicon solar cells," in *Applied Physics letters,* Vol. 102, 053509, January 2013 [Online]. Available: American Institute of Physics, https://aip.scitation.org/. [Accessed: May 24 2020].

[42] G. Limodio, G. Yang, Y. De Groot, P. Procel, L. Mazzarella, A.W. Weeber, O. Isabella and M. Zeman, "Implantation-based passivating contacts for crystalline silicon front/rear contacted solar cells," in *Progress in Photovoltaics,* Vol. 28, Issue 5, January 2020, pp. 403-416 [Online]. Available: Wiley Online Library, https://onlinelibrary.wiley.com/. [Accessed: May 28 2020].

[43] M.K. Hatalis and David W. Greve, "Large grain polycrystalline silicon by low-temperature annealing of low-pressure chemical vapor deposited amorphous silicon films," in *Journal of Applied Physics,* Vol. 63, Issue 7, December 1987, 2260 [Online]. Available: American Institute of Physics, https://aip.scitation.org/. [Accessed: May 30 2020]

[44] M.H. Brodsky, R.S. Title, K. Weiser and G.D. Pettit, "Structural, Optical, and Electrical Properties of Amorphous Silicon Films," in *Physycal Review B,* Vol. 1, Number 6, March 1970, 2632 [Online]. Available: APS Physics, https://journals.aps.org/. [Accessed: May 28 2020].

[45] R.B. Iverson and R. Reif, "Recrystallization of amorphized polycrystalline silicon films on SiO_2: Temperature dependence of the crystallization parameters," in *Journal of Applied Physics,* Vol. 62, Issue 5, May 1987 [Online]. Available: American Institute of Physics, https://aip.scitation.org/. [Accessed: May 28 2020].

[46] R.B. Iverson and R. Reif, "Stochastic model for grain size versus dose in implanted and annealed polycrystalline silicon films on SiO_2," in *Journal of Applied Physics,* Vol. 57, Issue 12, January 1985 [Online]. Available: American Institute of Physics, https://aip.scitation.org/. [Accessed: May 28 2020].

[47] Y. Wada and S. Nishimatsu, "Grain Growth Mechanism of Heavily Phosphorus-Implanted Polycrystalline Silicon," in *Journal of The Electrochemical Society,* Vol. 125, Issue 9, September 1978, 1499 [Online]. Available: IOPscience, https://iopscience.iop.org/. [Accessed: May 28 2020].

[48] L. Mei, M. Rivier, Y. Kwark and R.W. Dutton, "Grain-Growth Mechanisms in Polysilicon," in *Journal of The Electrochemical Society,* Vol. 129, Issue 8, August 1982, pp. 1792-1795 [Online]. Available: IOPscience, https://iopscience.iop.org/. [Accessed: June 16 2020].

[49] G. Harbeke, L. Krausbauer, E.F. Steigmeier, A.E. Widmer, H.F. Kappert and G. Neugebauer, "Growth and Physical Properties of LPCVD Polycrystalline Silicon Films," in *Journal of The Electrochemical Society,* Vol. 131, Issue 3, March 1984, 675 [Online]. Available: IOPscience, https://iopscience.iop.org/. [Accessed: May 30 2020].

[50] S. Solmi, M. Severi, R. Angelucci, L. Baldi and R. Bilenchi, "Electrical Properties of Thermally and Laser Annealed Polycrystalline Silicon Films Heavily Doped with Arsenic and Phosphorus," in *Journal of The Electrochemical Society,* Vol. 129, Issue 8, August 1982, 1811 [Online]. Available: IOPscience, https://iopscience.iop.org/. [Accessed: May 30 2020].

[51] A. Carabelas, D. Nobili and S. Solmi, "Grain boundary segragation in silicon heavily doped with phosphorus and arsenic," in *Journal de Physique Colloques,* Vol. 43 (C1), 1982, pp. 187-192 [Online]. Available: HAL archives ouvertes, https://hal.archives-ouvertes.fr/. [Accessed: May 27 2020].

[52] S. Olibet, C. Monachon, A. Hessler-Wyser, E. Vallat-Sauvain, L. Fesquet, J. Damon-Lacoste, S. Dewolf and C. Ballif, "Textured silicon heterojunction solar cells with over 700 mV open-circuit voltage studied by transmission electron microscopy," in *23rd EUPVSEC,* 2008 [Online]. Available: Semantic Scholar, https://www.semanticscholar.org/. [Accessed: May 31 2020].

[53] I.P. Sobkowicz, "Study and optimization of the growth of a-Si:H on wet-chemically textured c-Si substrates for the enhancement of a-Si:H/c-Si heterojunction solar cells," Ph.D. thesis, Laboratoire de Physique des Interfaces et des Couches Minces, Palaiseau, 2014.

[54] J. Ge, Z.P. Ling, J. Wonga, T. Mueller and A.G. Aberleab, "Optimisation of Intrinsic a-Si:H Passivation Layers in Crystalline-amorphous Silicon Heterojunction Solar Cells," in *Energy Procedia,* Vol. 15, 2012, pp. 107-117 [Online]. Available: Science Direct, https://www.sciencedirect.com. [Accessed: Jun. 1 2020].

[55] T.H. Wang, E. Iwaniczko, M.R.Page, D.H. Levi, Y. Yan, H.M. Branz and Q.Wang, "Effect of emitter deposition temperature on surface passivation in hot-wire chemical vapor deposited silicon heterojunction solar cells," in *Thin Solid Films,* Vol. 501, Issues 1-2, April 2006, pp. 284-287 [Online]. Available: Science Direct, https://www.sciencedirect.com. [Accessed: Jun. 1 2020].

[56] H. Fujiwara and M. Kondo, "Effects of a-Si:H layer thicknesses on the performance of a-Si:H/c-Si heterojunction solar cells," in *Journal of Applied Physics,* Vol. 101, Issue 5, December 2006 [Online]. Available: American Institute of Physics, https://aip.scitation.org/. [Accessed: Jun. 1 2020].

[57] K. Ding, U. Aeberhard, F. Finger and U. Rau, "Optimized amorphous silicon oxide buffer layers for silicon heterojunction solar cells with microcrystalline silicon oxide contact layers," in *Journal of Applied Physics,* Vol. 113, Issue 13, March 2013 [Online]. Available: American Institute of Physics, https://aip.scitation.org/. [Accessed: Jun. 1 2020].

[58] T. de Vrijer and A.H.M Smets, "The relation between precursor gas flows, thickness dependent material phases and opto-electrical properties of doped a/nc-$SiO_{X>0}$:H films ," in *IEEE Journal of Photovoltaics,* under review.

[59] O. Vetterl, M. Hülsbeck, J. Wolff, R. Carius, F. Finger, "Preparation of microcrystalline silicon seed-layers with defined structural properties," in *Thin Solid Films,* Vol. 427, Issues 1-2, March 2003, pp. 46-50 [Online]. Available: Science Direct, https://www.sciencedirect.com. [Accessed: Apr. 2 2020].

[60] C. Smit, R.A.C.M.M. van Swaaij, H. Donker, A.M.H.N. Petit, W.M.M. Kessels and M.C.M. van de Sanden, "Determining the material structure of microcrystalline silicon from Raman spectra," in *Journal of Applied Physics,* Vol. 94, Issue 5, June 2003, pp. 3582-3588 [Online]. Available: American Institute of Physics, https://aip.scitation.org/. [Accessed: May 10 2020].

[61] I. Beckers, N.H. Nickel, W. Pilz, W. Fuhs, "Influence of hydrogen on the structural order of microcrystalline silicon during the growth process," in *Journal of Non-Crystalline Solids,* Vol. 227-230, Part 2, May 1998, pp. 847-851 [Online]. Available: Science Direct, https://www.sciencedirect.com. [Accessed: Jun. 7 2020].

[62] Y.Q. Guo, X. Wang, C. Song, R. Huang, J. Song, "Influence of Radio Frequency Power on the Structural Properties of nc-Si Films Fabricated by VHF-PECVD," in *Key Engineering Materials,* Vol. 531-532, December 2012, pp. 469-472 [Online]. Available: Scientific.net, https://www.scientific.net/. [Accessed: Jun. 11 2020].

[63] K.Y. Chan, D. Knipp, A. Gordijn, H. Stiebig, "Influence of crystalline volume fraction on the performance of high mobility microcrystalline silicon thin-film transistors," in *Journal of Non-Crystalline Solids,* Vol. 354, Issues 19-25, May 2008, pp. 2505-2508 [Online]. Available: Science Direct, https://www.sciencedirect.com. [Accessed: Jun. 11 2020].

[64] O. Vetterl, F. Finger, R. Carius, P. Hapke, L. Houben, O. Kluth, A. Lambertz, A. Mück, B. Rech and H. Wagner, "Intrinsic microcrystalline silicon: A new material for photovoltaics," in *Solar Energy Materials and Solar cells,* Vol. 62, 2000, pp. 97-108 [Online]. Available: Semantic Scholar, https://www.semanticscholar.org/. [Accessed: Jun. 21 2020].

[65] S. Klein, T. Repmann and T. Brammer, "Microcrystalline silicon films and solar cells deposited by PECVD and HWCVD," in *Solar Energy,* Vol. 77, Issue 6, December 2004, pp. 893-908 [Online]. Available: Science Direct, https://www.sciencedirect.com. [Accessed: Jun. 21 2020].

[66] C. Ellert, C. Wachtendorf, A. Hedler, M. Klindworth and M. Martinek, "Influence of Raman crystallinity on the performance of micromorph thin film silicon solar cells," in *Solar Energy Materials and Solar cells,* Vol. 96, January 2012, pp. 71-76 [Online]. Available: Science Direct, https://www.sciencedirect.com. [Accessed: Jun. 21 2020].

[67] R. Vasudevan, Z. Thanawala, L. Han, T. Buijs, H. Tan, D. Deligiannis, P. Perez-Rodriguez, I.A. Digdaya, W.A. Smith, M. Zeman and A.H.M. Smets, "A thin-film silicon/silicon hetero-junction hybrid solar cell for photoelectrochemical water-reduction applications," in *Solar Energy Materials and Solar cells,* Vol. 150, June 2016, pp. 82-87 [Online]. Available: Science Direct, https://www.sciencedirect.com. [Accessed: Jun. 27 2020].

[68] P. Procel, G. Yang, O. Isabella and M. Zeman, "Theoretical evaluation of contact stack for high efficiency IBC-SHJ solar cells," in *Solar Energy Materials and Solar cells,* Vol. 186, November 2018, pp. 66-77 [Online]. Available: Science Direct, https://www.sciencedirect.com. [Accessed: Jun. 25 2020].

[69] F.T. Si, "Quadruple-Junction Thin-Film Silicon-Based Solar Cells," Ph.D. thesis, Delft University of Technology, Delft, 2017.

[70] G. Bugnon, G. Parascandolo, S. Hänni, M. Stuckelberger, M. Charrière, M. Despeisse, F. Meillaud and C. Ballif, "Silicon oxide buffer layer at the p–i interface in amorphous and microcrystalline silicon solar cells," in *Solar Energy Materials and Solar Cells,* Vol. 120, Part A, January 2014, pp. 143-150 [Online]. Available: Science Direct, https://www.sciencedirect.com. [Accessed: Jan. 22 2020].

[71] Y. Zeng, H. Tong, C. Quan, L. Cai, Z. Yang, K. Chen, Z. Yuan, C. Wu, B. Yan, P. Gao and J. Ye, "Theoretical exploration towards high-efficiency tunnel oxide passivatedcarrier-selective contacts (TOPCon) solar cells," in *Solar Energy,* Vol. 155, October 2017, pp. 654-660 [Online]. Available: Science Direct, https://www.sciencedirect.com. [Accessed: Apr. 1 2020].

[72] D. Han, G. Yue, J.D. Lorentzen, and J. Lin, "Optical and electronic properties of microcrystalline silicon as a function of microcrystallinity," in *Journal of Applied Physics,* Vol. 87, Issue 4, October 1999 [Online]. Available: American Institute of Physics, https://aip.scitation.org/. [Accessed: May 11 2020].